

**Identification of anodic and cathodic locations on  
corroding steel reinforcement in concrete using  
inverse modelling of half-cell potential  
measurements**

A thesis submitted to  
the Faculty of Graduate Studies and Research  
in partial fulfillment of the requirements for the degree of  
**Master of Applied Science in Civil Engineering**

by

**Phil Marinier, B.Eng.**

Department of Civil and Environmental Engineering  
Carleton University  
Ottawa-Carleton Institute of Civil and Environmental Engineering  
February, 2011

©Copyright

Phil Marinier. 2011



Library and Archives  
Canada

Published Heritage  
Branch

395 Wellington Street  
Ottawa ON K1A 0N4  
Canada

Bibliothèque et  
Archives Canada

Direction du  
Patrimoine de l'édition

395, rue Wellington  
Ottawa ON K1A 0N4  
Canada

*Your file* *Votre référence*  
ISBN: 978-0-494-81666-0  
*Our file* *Notre référence*  
ISBN: 978-0-494-81666-0

**NOTICE:**

The author has granted a non-exclusive license allowing Library and Archives Canada to reproduce, publish, archive, preserve, conserve, communicate to the public by telecommunication or on the Internet, loan, distribute and sell theses worldwide, for commercial or non-commercial purposes, in microform, paper, electronic and/or any other formats.

The author retains copyright ownership and moral rights in this thesis. Neither the thesis nor substantial extracts from it may be printed or otherwise reproduced without the author's permission.

---

In compliance with the Canadian Privacy Act some supporting forms may have been removed from this thesis.

While these forms may be included in the document page count, their removal does not represent any loss of content from the thesis.

**AVIS:**

L'auteur a accordé une licence non exclusive permettant à la Bibliothèque et Archives Canada de reproduire, publier, archiver, sauvegarder, conserver, transmettre au public par télécommunication ou par l'Internet, prêter, distribuer et vendre des thèses partout dans le monde, à des fins commerciales ou autres, sur support microforme, papier, électronique et/ou autres formats.

L'auteur conserve la propriété du droit d'auteur et des droits moraux qui protègent cette thèse. Ni la thèse ni des extraits substantiels de celle-ci ne doivent être imprimés ou autrement reproduits sans son autorisation.

---

Conformément à la loi canadienne sur la protection de la vie privée, quelques formulaires secondaires ont été enlevés de cette thèse.

Bien que ces formulaires aient inclus dans la pagination, il n'y aura aucun contenu manquant.

  
**Canada**

# Abstract

The determination of the locations and sizes of actively corroding areas on embedded steel reinforcement in concrete is difficult using the widely-used and standardized half-cell potential measurement technique. In this research, it is hypothesized that half cell measurements on the surface of the concrete can be used, beyond their originally intended purpose, to identify the locations and sizes of anodic and cathodic sites on the steel reinforcement by means of inverse modelling algorithms. The problem, simply put, is a boundary identification problem: given the potential measurements on the surface of the concrete, identify the anodic and cathodic boundaries on the surface of the reinforcement. Once the anodic and cathodic sites are identified, it is also possible to determine corrosion rates through well-established forward solution algorithms. To this end, a conjugate-gradient based inverse modelling algorithm was developed and coded using open-source finite element analysis libraries to assimilate standard half-cell potential measurements on the concrete surface and to calculate the potential distribution on the surface of the reinforcement. The performance of the inverse model was tested with various configurations of corroding systems with single and multiple anodes. The results show that the developed inverse modelling algorithm is robust and can even be used in cases for which the number of observation points on the surface of the concrete is limited.

# Acknowledgments

I would like to acknowledge the support and guidance of Prof. O. Burkan Isgor. Without his patient direction and understanding, this work would never have been complete. It has been a great honour and pleasure to work under him and to have had the opportunity to benefit from his knowledge and experience.

I would also like to thank my family, my girlfriend and my friends for their understanding and for being there for me through this research and the writing of this thesis.

# Table of Contents

<b>Abstract</b>	<b>ii</b>
<b>Acknowledgments</b>	<b>iii</b>
<b>Table of Contents</b>	<b>iv</b>
<b>List of Tables</b>	<b>viii</b>
<b>List of Figures</b>	<b>x</b>
<b>1 Introduction</b>	<b>1</b>
1.1 Background . . . . .	1
1.2 Objectives and Scope . . . . .	8
1.3 Organization of the Thesis . . . . .	9
<b>2 Background</b>	<b>11</b>
2.1 General . . . . .	11
2.2 Inverse Modelling - Basic Overview . . . . .	12
2.3 Inverse Modelling of Corrosion . . . . .	15
2.3.1 General Corrosion Problems . . . . .	16
2.3.2 Corrosion of Steel in Concrete . . . . .	23
2.4 Summary . . . . .	28

<b>3</b>	<b>Formulation of the Inverse Modelling Algorithm</b>	<b>30</b>
3.1	General . . . . .	30
3.2	Forward Model . . . . .	31
3.3	Inverse Model . . . . .	33
3.3.1	The Cost Function . . . . .	33
3.3.2	The Gradient of the Cost Function . . . . .	34
3.3.3	Conjugate Gradient Method . . . . .	37
3.4	Regularisation . . . . .	39
3.4.1	Initial Conditions and Starting Values of the Analysis . . . . .	41
3.4.2	Convergence Criterion . . . . .	41
3.5	Implementation: FEniCS / Dolfin framework . . . . .	41
3.5.1	Inverse Solution Algorithm . . . . .	43
3.6	Identical Twin Numerical Experiments . . . . .	44
3.7	Sample Analysis . . . . .	46
<b>4</b>	<b>Studies on Systems with a Localized Single Anode</b>	<b>50</b>
4.1	General . . . . .	50
4.2	Preliminary Analysis . . . . .	51
4.3	Parametric Study . . . . .	56
4.4	Results and Discussion: Preliminary Analysis . . . . .	59
4.4.1	PA 1: Perturbation Analysis . . . . .	59
4.4.2	PA 2: Interpolation of $\alpha$ . . . . .	59
4.4.3	PA 3: Element Type . . . . .	61
4.4.4	PA 3: Element Size . . . . .	63
4.4.5	PA 3: Domain Size . . . . .	65
4.4.6	PA 4: Initial Potentials along Steel/Concrete Interface . . . . .	68

4.4.7	PA 5: Convergence Criteria Analysis . . . . .	69
4.4.8	Summary of the Preliminary Analysis . . . . .	70
4.5	Results and Discussion: Parametric study . . . . .	72
4.5.1	Effect of Residual Equations . . . . .	72
4.5.2	Effect of Anode Location . . . . .	73
4.5.3	Effect of A/C Ratio . . . . .	74
4.5.4	Effect of Resistivity and Concrete Cover Thickness . . . . .	77
4.6	Removal of Observation Points . . . . .	78
4.7	Summary of the Parametric Study . . . . .	80
<b>5</b>	<b>Studies on Systems with Multiple Anodes</b>	<b>98</b>
5.1	General . . . . .	98
5.2	Preliminary Analysis . . . . .	99
5.3	Parametric Study . . . . .	102
5.4	Results and Discussion: Preliminary Analysis . . . . .	103
5.4.1	Convergence Criteria Analysis . . . . .	103
5.4.2	Interpolation of $\alpha$ . . . . .	103
5.4.3	Initial Potentials along Steel/Concrete Interface . . . . .	104
5.4.4	Regularisation Analysis . . . . .	106
5.5	Results and Discussion: Parametric Study . . . . .	108
5.5.1	Effect of Resistivity and Cover Thickness . . . . .	108
5.5.2	Effect of the A/C Ratio . . . . .	109
5.5.3	Effect of Increasing the Number of Anodes . . . . .	109
5.5.4	Effect of Asymmetry . . . . .	110
5.6	Removal of Observation Points . . . . .	110
5.7	Summary of the Parametric Study . . . . .	112

<b>6</b>	<b>Conclusions and Future Work</b>	<b>138</b>
6.1	General . . . . .	138
6.2	Conclusions . . . . .	139
6.3	Future Work . . . . .	140
	<b>List of References</b>	<b>142</b>

# List of Tables

3.1	Input data for the sample analysis. . . . .	47
4.1	Specifications of the computer used in the identical twin numerical experiments. . . . .	51
4.2	Preliminary analysis test grid. . . . .	53
4.3	Parametric study test grid. . . . .	57
4.4	Inverse convergence rates depending on the $\alpha$ interval size used in the quadratic interpolation algorithm. . . . .	60
4.5	Convergence rates of the inverse solution depending on element size. . . . .	65
4.6	Inverse convergence rates depending on domain dimensions with two different resistivities. . . . .	67
4.7	Inverse convergence rates depending on the initial potential distribution. . . . .	72
4.8	Inverse convergence rates depending on anode location for a given A/C ratio, resistivity and cover thicknesses. . . . .	75
5.1	Description of the anode configurations used in the studies on systems with multiple anodes. . . . .	99
5.2	Preliminary analysis test grid. . . . .	102
5.3	Parameter study test grid. . . . .	103
5.4	Final cost function depending on the interval size used to approximate $\alpha$ . . . . .	104

5.5	Times of convergence of the inverse model depending on the initial potentials on steel/concrete interface. . . . .	105
5.6	Times of convergence of the inverse model for all four anode configurations. . . . .	111

# List of Figures

1.1	Schematic illustration of the half cell potential measurement process (taken from [1]) . . . . .	4
1.2	A typical potential map created from half-cell measurements on the surface a 240 cm $\times$ 240 cm concrete slab. Potentials measured in mV vs CSE. . . . .	5
1.3	Potential distributions at the surface of concrete and at the steel/concrete interface at different concrete resistivities ( $\rho$ ) (reported by [1] for a numerical case study). Cover thickness and A/C ratio are the same for both cases. . . . .	6
1.4	Potential distributions at the surface of concrete and at the steel/concrete interface at different concrete cover thicknesses (d) (reported by [1] for a numerical case study). Concrete resistivity and A/C ratio are the same for both cases. . . . .	6
1.5	Analyses on the average potentials at the surface of the concrete (reported by [1] for a numerical case study). . . . .	7
3.1	Boundary conditions for the forward problem. . . . .	32
3.2	Comparison of the results of the sample analysis to the initial value and the target forward solution. . . . .	48

3.3	Convergence of the sample analysis. Comparison of the intermediary solutions at different iterations to show the progression of the solution.	49
4.1	Discretization schemes used in the preliminary analysis . . . . .	55
4.2	Possible selections for the initial potential distribution along the steel/concrete interface. . . . .	56
4.3	Comparison of four proposed $\alpha$ interval sizes over 25 iterations showing the divergence of the calculated value for $\alpha$ when the two smallest intervals are used. . . . .	61
4.4	Close up comparison of the forward solution using different diagonals for the discretisation scheme at the left transition zone between anodic and cathodic potentials. Middle location for the anode, A/C ratio = 0.5, $\rho = 150 \Omega\text{-m}$ . . . . .	62
4.5	Close up comparison of the forward solution using different diagonals for the discretisation scheme at the right transition zone between anodic and cathodic potentials. Middle location for the anode, A/C ratio = 0.5, $\rho = 150 \Omega\text{-m}$ . . . . .	63
4.6	Forward solution of the potential distribution along the steel/concrete interface for different element sizes. . . . .	64
4.7	Inverse solution for the interface potential depending on the initial potential distribution. . . . .	69
4.8	Detail of the left side of the plot of the inverse solution for the interface potential depending on the initial potential distribution. . . . .	70
4.9	Detail of the right side of the plot of the inverse solution for the interface potential depending on the initial potential distribution. . . . .	71

4.10	Inverse solution that did not converge below tolerance of $10^{-8}$ . Middle anodic location, A/C ratio = 0.11, $\rho = 150 \Omega\text{-m}$ , cover thickness = 80 mm. . . . .	76
4.11	Comparison of the forward solution for two values of resistivity. Resistivity measure in $\Omega\text{-m}$ . . . . .	81
4.12	Comparison of the forward and inverse solutions with an end location for the anode, A/C ratio of 0.11, resistivity of $150 \Omega\text{-m}$ . . . . .	82
4.13	Comparison of the forward and inverse solutions with an end location for the anode, A/C ratio of 0.11, resistivity of $1500 \Omega\text{-m}$ . . . . .	83
4.14	Comparison of the forward and inverse solutions with an end location for the anode, A/C ratio of 0.25, resistivity of $150 \Omega\text{-m}$ . . . . .	84
4.15	Comparison of the forward and inverse solutions with an end location for the anode, A/C ratio of 0.25, resistivity of $1500 \Omega\text{-m}$ . . . . .	85
4.16	Comparison of the forward and inverse solutions with an end location for the anode, A/C ratio of 0.5, resistivity of $150 \Omega\text{-m}$ . . . . .	86
4.17	Comparison of the forward and inverse solutions with an end location for the anode, A/C ratio of 0.5, resistivity of $1500 \Omega\text{-m}$ . . . . .	87
4.18	Comparison of the forward and inverse solutions with a middle location for the anode, A/C ratio of 0.11, resistivity of $150 \Omega\text{-m}$ . . . . .	88
4.19	Comparison of the forward and inverse solutions with a middle location for the anode, A/C ratio of 0.11, resistivity of $1500 \Omega\text{-m}$ . . . . .	89
4.20	Comparison of the forward and inverse solutions with a middle location for the anode, A/C ratio of 0.25, resistivity of $150 \Omega\text{-m}$ . . . . .	90
4.21	Comparison of the forward and inverse solutions with a middle location for the anode, A/C ratio of 0.25, resistivity of $1500 \Omega\text{-m}$ . . . . .	91

4.22	Comparison of the forward and inverse solutions with a middle location for the anode, A/C ratio of 0.5, resistivity of 150 $\Omega$ -m. . . . .	92
4.23	Comparison of the forward and inverse solutions with a middle location for the anode, A/C ratio of 0.5, resistivity of 1500 $\Omega$ -m. . . . .	93
4.24	Comparison of the inverse solution with 60 observed nodes to the control solution and the forward solution. . . . .	94
4.25	Comparison of the inverse solution with 40 observed nodes to the control solution and the forward solution. . . . .	95
4.26	Comparison of the inverse solution with 30 observed nodes to the control solution and the forward solution. . . . .	96
4.27	Comparison of the inverse solution with 24 observed nodes to the control solution and the forward solution. . . . .	97
5.1	Anode configurations used in this study. . . . .	100
5.2	Inverse solution for the interface potential depending on the initial potential distribution. . . . .	105
5.3	Close up of the left side of the inverse solution for the interface potential depending on the initial potential distribution. . . . .	106
5.4	Close up of the right side of the inverse solution for the interface potential depending on the initial potential distribution. . . . .	107
5.5	Comparison of the forward and inverse solutions with Configuration 1 and a resistivity of 150 $\Omega$ -m. . . . .	114
5.6	Comparison of the forward and inverse solutions with Configuration 1 and a resistivity of 1500 $\Omega$ -m. . . . .	115
5.7	Comparison of the forward and inverse solutions with Configuration 2 and a resistivity of 150 $\Omega$ -m. . . . .	116

5.8	Comparison of the forward and inverse solutions with Configuration 2 and a resistivity of 1500 $\Omega$ -m. . . . .	117
5.9	Comparison of the forward and inverse solutions with Configuration 3 and a resistivity of 150 $\Omega$ -m. . . . .	118
5.10	Comparison of the forward and inverse solutions with Configuration 3 and a resistivity of 1500 $\Omega$ -m. . . . .	119
5.11	Comparison of the forward and inverse solutions with Configuration 4 and a resistivity of 150 $\Omega$ -m. . . . .	120
5.12	Comparison of the forward and inverse solutions with Configuration 4 and a resistivity of 1500 $\Omega$ -m. . . . .	121
5.13	Comparison of the inverse solution of Configuration 1 with 60 observed nodes, the forward solution and the control solution with all nodes observed. . . . .	122
5.14	Comparison of the inverse solution of Configuration 1 with 40 observed nodes, the forward solution and the control solution with all nodes observed. . . . .	123
5.15	Comparison of the inverse solution of Configuration 1 with 30 observed nodes, the forward solution and the control solution with all nodes observed. . . . .	124
5.16	Comparison of the inverse solution of Configuration 1 with 24 observed nodes, the forward solution and the control solution with all nodes observed. . . . .	125
5.17	Comparison of the inverse solution of Configuration 2 with 60 observed nodes, the forward solution and the control solution with all nodes observed. . . . .	126

5.18	Comparison of the inverse solution of Configuration 2 with 40 observed nodes, the forward solution and the control solution with all nodes observed. . . . .	127
5.19	Comparison of the inverse solution of Configuration 2 with 30 observed nodes, the forward solution and the control solution with all nodes observed. . . . .	128
5.20	Comparison of the inverse solution of Configuration 2 with 24 observed nodes, the forward solution and the control solution with all nodes observed. . . . .	129
5.21	Comparison of the inverse solution of Configuration 3 with 60 observed nodes, the forward solution and the control solution with all nodes observed. . . . .	130
5.22	Comparison of the inverse solution of Configuration 3 with 40 observed nodes, the forward solution and the control solution with all nodes observed. . . . .	131
5.23	Comparison of the inverse solution of Configuration 3 with 30 observed nodes, the forward solution and the control solution with all nodes observed. . . . .	132
5.24	Comparison of the inverse solution of Configuration 3 with 24 observed nodes, the forward solution and the control solution with all nodes observed. . . . .	133
5.25	Comparison of the inverse solution of Configuration 4 with 60 observed nodes, the forward solution and the control solution with all nodes observed. . . . .	134

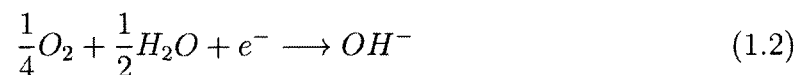
5.26	Comparison of the inverse solution of Configuration 4 with 40 observed nodes, the forward solution and the control solution with all nodes observed. . . . .	135
5.27	Comparison of the inverse solution of Configuration 4 with 30 observed nodes, the forward solution and the control solution with all nodes observed. . . . .	136
5.28	Comparison of the inverse solution of Configuration 4 with 24 observed nodes, the forward solution and the control solution with all nodes observed. . . . .	137

# Chapter 1

## Introduction

### 1.1 Background

Corrosion is a destructive electrochemical process consisting of two half-cell reactions: oxidation and reduction [1,2]. In the case of corrosion of steel in concrete, oxidation and reduction reactions can be described by Equations (1.1) and (1.2), respectively [3,4]:



The oxidation reaction, which leads to metal (Fe) loss, takes place at the anodes while the reduction reaction takes place at the cathodes. The electrons that are produced by the anodic reaction are consumed at the cathodes, and the electrochemical circuit is completed by the migration of ions between cathodes and the anodes. When two reactions occur in widely separated locations, they form a macro-cell, and the

process is called macro-cell corrosion. When they occur close together and essentially at the same location, they form a micro-cell, and the process is called micro-cell corrosion.

Steel reinforcement in concrete is generally well protected against corrosion by a passive film that is quite stable in the highly alkaline environment of concrete ( $\text{pH} > 12.5$ ) [3]. However, the penetration of aggressive agents such as chloride through the concrete cover and/or the carbonation of that cover may result in the destruction of this passive film (depassivation) and the initiation of active corrosion. The first phase of the corrosion process, the penetration of the aggressive agents through the concrete cover to the level of reinforcing steel, is called the initiation stage, and the second phase, after the depassivation of the reinforcing steel, is referred as the propagation stage. The depassivation of steel marks the end of the initiation stage and the beginning of propagation stage [5].

During the propagation phase, ions migrate through the concrete pore solution. The reaction of iron and hydroxide ions in the pore solution results in expansive corrosion products (iron oxides) that may lead to cracking, delamination and spalling of the concrete cover and the loss of the bond between steel and concrete. Reduced cross section of the steel reinforcement at the anodic locations due to consumption of iron in the oxidation reaction may also lead to reduction in load carrying capacity of the structural member [3].

In reinforcement that is undergoing active corrosion, the electric potentials of anodes are more negative than the electric potentials of cathodes by as much as 700 mV measured with respect to a reference electrode, for example, the copper sulfate electrode (CSE) or the standard calomel electrode (SCE). Therefore, the actively corroding areas (anodic sites) can be identified by areas of more negative potential on the steel surface [3]. In practice, since the reinforcement is embedded in concrete,

it is not possible to measure potentials on the steel surface without. Instead, it is assumed that potential measurements on the surface of concrete are correlated with the potentials on the steel surface, and that these surface potentials can be used as indicators for the corrosion process. This assumption establishes the basis of the half-cell potential mapping process [6]: relatively more negative measurements on the concrete surface are associated with actively corroding anodic sites.

Half-cell potential mapping is a standardized [6] non-destructive technique that is used to predict the probability of steel corrosion in reinforced concrete members. In this method, the potential difference between an external reference electrode, located at the surface of the concrete, and the embedded reinforcement is measured with a high impedance voltmeter. A direct electrical connection, established through a wire between the reinforcement and the voltmeter, and an ionic connection between the external electrode and the reinforcement through the concrete cover are used to obtain the potential measurements. Figure 1.1 schematically illustrates the test setup for a typical half-cell potential test in reinforced concrete members.

ASTM C876 2009 [6] states that the more negative the measured surface potential, the greater probability of corrosion: half-cell potential measurements less than -350 mV with respect to the copper/copper sulfate electrode (CSE) corresponds to a 90% probability. When the measurement is greater than -200 mV (CSE) the probability is less than 10%. When the potential is between -350 mV (CSE) and -200 mV (CSE), the corrosion state of the rebar cannot be predicted. Figure 1.2 illustrates an example half-cell potential plot on a 240 cm x 240 cm concrete surface.

Despite its widespread application, the interpretation of half-cell potential mapping results continues to be a major challenge for engineers. One of the main reasons

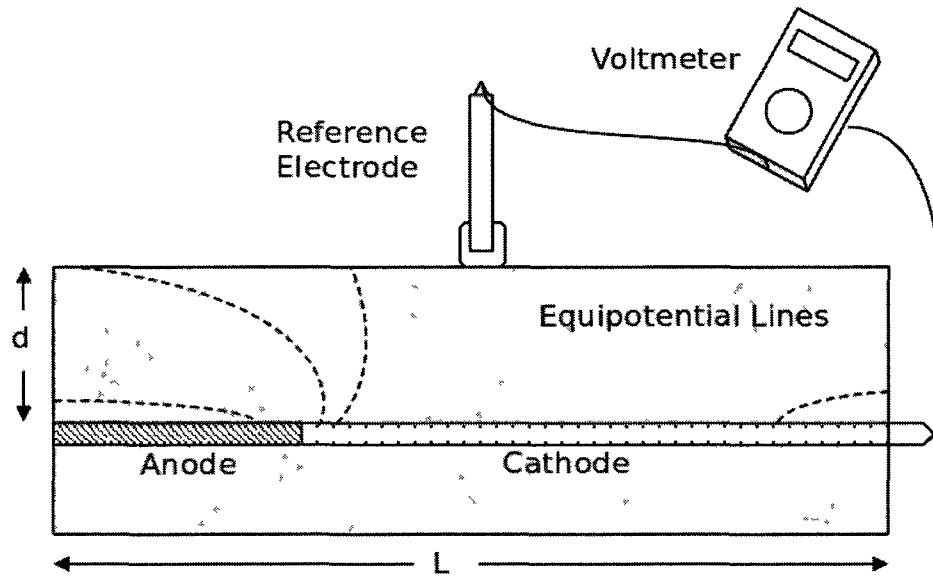


**Figure 1.1:** Schematic illustration of the half cell potential measurement process (taken from [1])

for this difficulty is that half-cell potential mapping only provides information to predict the probability of the occurrence of corrosion without giving any insight into the rate (or kinetics) of corrosion. Pour-Ghaz et al. [1] showed that, for the same corrosion rate, one can measure different potentials at the surface of concrete, corresponding to different values of concrete resistivity, and thus have more than one estimated probability of corrosion for the same actual state of corrosion. Furthermore, potential ranges indicating the corrosion probability of steel in concrete have been subject to debate since they have been set based on a limited number of experimental studies [3].

In addition, the correlation between the half cell potentials on the concrete surface and the probability of corrosion are quite sensitive to not only to the concrete resistivity, but also to the anode-to-cathode surface area ratio ( $A/C$  ratio) and cover thickness [3.7.8]. Figures 1.3 and 1.4 provide the results of a numerical investigation by Pour-Ghaz et al. [1], in which they studied the effects of these factors on

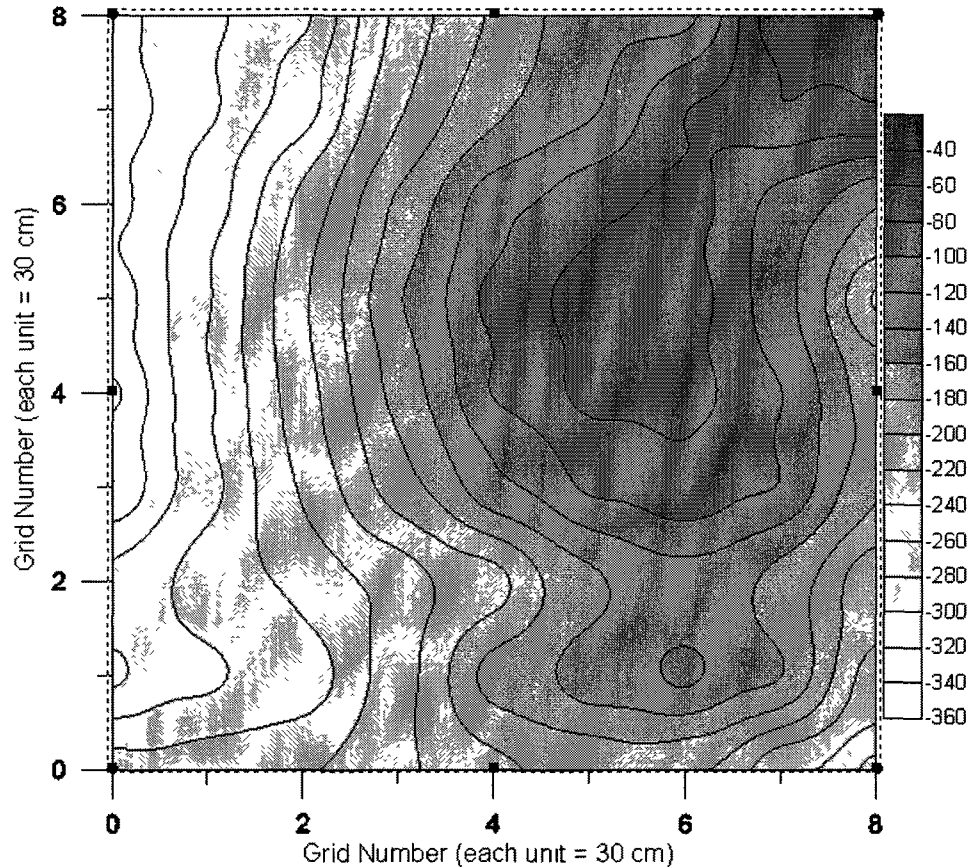


**Figure 1.2:** A typical potential map created from half-cell measurements on the surface a 240 cm  $\times$  240 cm concrete slab. Potentials measured in mV vs CSE.

the correlation between potentials on the concrete surface and on the concrete/steel interface. It can be observed from these figures that larger concrete resistivity (Figure 1.3) or larger cover thickness (Figure 1.4) result in weaker correlation between the two potentials, making the interpretation of half cell data on the concrete surface difficult as well as hindering the assessment of the probability of active corrosion on the concrete/steel interface.

It should also be noted that half-cell potential measurement is a function of the type of corrosion. In the case of uniform micro-cell corrosion, in which the A/C ratio is near unity, the potential readings at the surface of concrete are typically close to

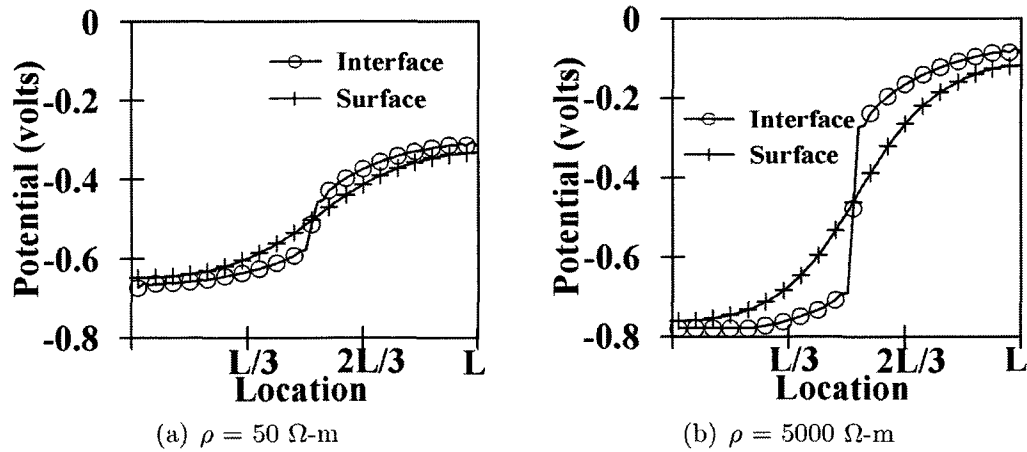


**Figure 1.3:** Potential distributions at the surface of concrete and at the steel/concrete interface at different concrete resistivities ( $\rho$ ) (reported by [1] for a numerical case study). Cover thickness and A/C ratio are the same for both cases.

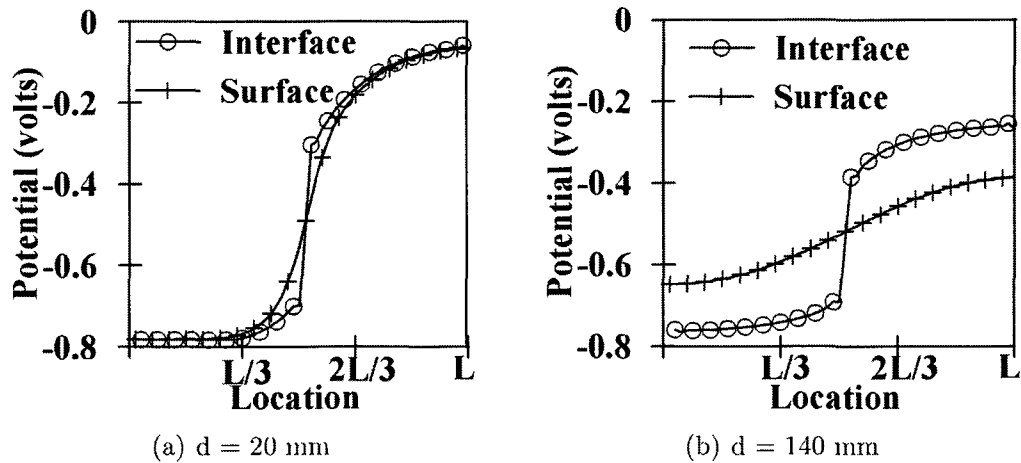


**Figure 1.4:** Potential distributions at the surface of concrete and at the steel/concrete interface at different concrete cover thicknesses ( $d$ ) (reported by [1] for a numerical case study). Concrete resistivity and A/C ratio are the same for both cases.

the potential at the interface of steel and concrete [9]; however, in the case of non-uniform macro-cell corrosion, local or pitting corrosion with a small A/C ratio, the measured potentials at the surface of concrete can be substantially different from those of the steel/concrete interface. As illustrated in Figure 1.5, Pour-Ghaz et al. [1]

showed that when the average potential at the surface of concrete is a large value (i.e., more positive) the probability of the occurrence of corrosion is low, as per ASTM C-876 2009 [6]; however the rate of such a corrosion, if it occurs in the form of localized corrosion, can be very high. On the other hand, if the average potential at the surface of concrete is a small value (i.e. more negative), the probability of the corrosion is higher, but such corrosion may proceed more uniformly. Accurate detection of localized corrosion, in which A/C ratio can be small, may not be feasible with half-cell potential measurement method unless supplementary information is provided.

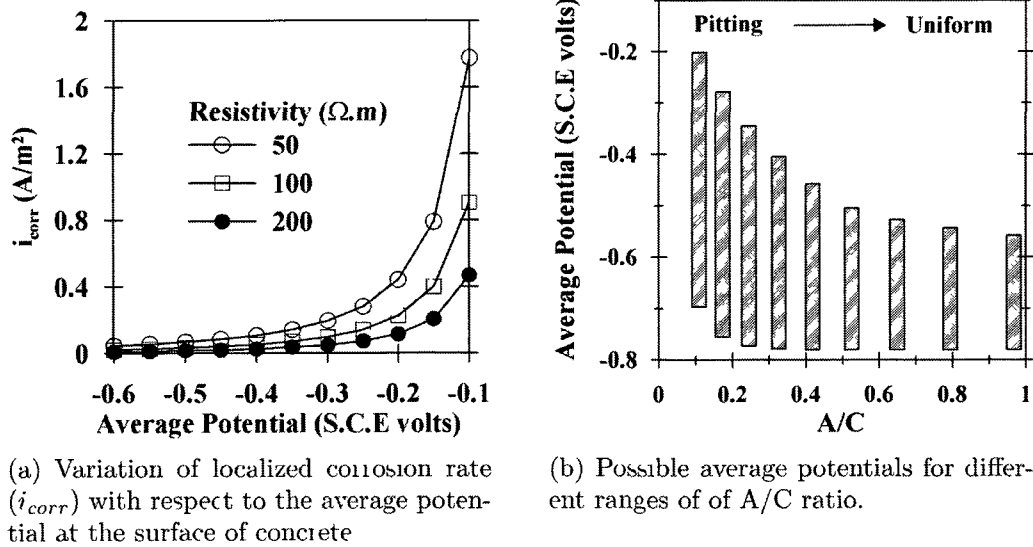


**Figure 1.5:** Analyses on the average potentials at the surface of the concrete (reported by [1] for a numerical case study).

In summary, half cell potential mapping, as it is used in current practice, is prone to errors and misinterpretation. In most cases, half-cell tests provide ambiguous data that cannot even be used to identify anodic (active) zones of corrosion accurately. Without complementing the half-cell data with corrosion rate measurements

using either corrosion rate measurement devices or predictions through modelling, reliable estimates about the corrosion state of the structural members cannot be made. Unfortunately, existing corrosion rate measurement devices have inherent accuracy problems [10, 11] and models for prediction corrosion rates require knowledge of the anodic and cathodic locations on the reinforcement surface, which is not a trivial requirement.

## 1.2 Objectives and Scope

The main objective of the present work is to provide practicing engineers with a tool that they can use to better interpret the results of half-cell potential measurements. In this research it is hypothesized that half cell measurements on the surface of the concrete can be used, beyond their originally intended purpose, to identify the locations and sizes of anodic and cathodic sites on the steel reinforcement by means of inverse modelling algorithms. The problem, simply put, is a boundary identification problem: given the electric potential measurements on the surface of the concrete, identify the anodic and cathodic boundaries on the surface of the reinforcement. Once the anodic and cathodic sites are identified, it is also possible to determine corrosion rates through well-established forward solution algorithms [1, 4, 9, 12–14]. It is assumed in this research that anodic and cathodic sites on the reinforcement surface are distinctly separated; i.e., macro-cell corrosion is the main form of corrosion to be detected.

With this main goal, the following specific objectives are identified:

1. Given the boundary conditions (i.e., anodic and cathodic sites on the steel surface and other boundary conditions on the other surfaces), develop and verify a forward solution algorithm to solve the potential distribution over a specified

domain. This forward model can be used to analyze and predict corrosion rates on the steel surface. The forward solution algorithm will be implemented (coded) using the finite element method, and it will be used both as part of the inverse modelling algorithm and to generate data to be used in the identical twin numerical experiments.

2. Formulate an inverse modelling algorithm that uses the given the electric potential measurements on the surface of the concrete to identify the anodic and cathodic boundaries on the surface of the reinforcement.
3. Implement and code the inverse modelling algorithm.
4. Carry out identical twin numerical experiments, in which the solution of a well-posed and validated forward model, for which all boundary conditions and system parameters are defined, are used both to generate input data for, and to verify the predictions of the inverse problem.
5. Carry out parametric investigations to study the performance of this inverse modelling algorithm.

## 1.3 Organization of the Thesis

**Chapter 1:** A brief summary of corrosion and corrosion measurement processes is provided. The objectives and scope of the thesis are presented.

**Chapter 2:** This chapter gives a brief background on inverse modeling, examines the literature and highlights the strengths and weaknesses of the methods of existing inverse solution methods. The different types of corrosion problems and the proposed

methods of solution are discussed. It is demonstrated that there is a need for a new inverse modelling approach to assimilate half-cell potential surface measurements.

**Chapter 3:** The mathematical basis of the proposed method of inverse solution of the corrosion problem is laid out. Both the forward and inverse model are discussed, and the model framework is explained. The algorithm is presented and its effectiveness is demonstrated with a sample analysis.

**Chapter 4:** A series of preliminary tests are conducted to determine the ideal initial conditions for the model. Using these initial conditions, a parametric analysis is carried out to examine the behaviour of the model with a single localised anode. Different parameters including cover thickness, resistivity, etc. are varied over a reasonable range to determine the applicability of the model to realistic situations.

**Chapter 5:** The parametric study in Chapter 4 is expanded to systems with multiple anodes and cathodes. Four different configurations of anodes and cathodes are selected to test the behaviour of the model.

**Chapter 6:** The main conclusions of the research are presented. The strengths and weaknesses of the developed model are discussed. Future work to expand and improve the model is also discussed.

## Chapter 2

# Background

### 2.1 General

This chapter provides a basic background on inverse modelling, its application to typical corrosion problems and existing literature on its use for applications relating to the corrosion of steel in concrete structures. Since the literature on inverse modelling is vast and dates back many decades, it will not be one of the objectives of this chapter to provide a detailed review of the topic; only an overview of the basic principles is provided here. The following books on inverse modelling are more appropriate for a detailed review: [15–18].

Although inverse modelling techniques have been used to study corrosion in applications other than reinforced concrete [13, 19–22], the work on the use of inverse modelling in reinforced concrete has been quite limited. After covering the use of inverse modeling for general corrosion applications by several authors, this chapter will review the work that is most relevant to the present study, namely, inverse modelling as applied to the corrosion of steel in concrete. Among these are the studies by Ridha et al. [23, 24], which used inverse modelling to interpret half-cell potential data taken on the concrete surface and characterized steel corrosion in concrete using the

boundary element method and a multi-step genetic algorithm. A similar study by Leelalerkiet et al. [25] will also be presented. The work of Kranc and Sagues [26] further demonstrates the potential of inverse modelling to study reinforcement corrosion in reinforced concrete structures and is also reviewed in this chapter.

## 2.2 Inverse Modelling - Basic Overview

One of the main methods of representing physical phenomena in science and engineering is by means of mathematical models, which usually take the form of boundary value problems defined over a domain with specific boundary and initial conditions. The problem in the domain is typically described using governing ordinary or partial differential equations. Given a complete description of a mathematical model, engineers and scientists can make predictions about the outcome of the physical phenomenon under investigation. This problem of predicting the measured results of a physical system with known parameters is called the forward problem.

In many cases, however, mathematical models depend on parameters that are poorly known or cannot be measured; in these cases, inverse models become useful. An inverse problem consists of using the actual result of some measurements to infer the values of the parameters that characterize the physical system [15]. The corrosion of steel in concrete is a typical example, in which the forward problem of predicting the electric potential distribution in the domain of the analysis requires prior knowledge of the locations and sizes of the anodes and cathodes on the embedded steel. Obtaining the locations of anodes and cathodes is not practical without destroying the reinforced concrete member and exposing the embedded steel. In most cases, this is not even possible even after exposing the steel since the anodes and cathodes may not be distinguishable by visual inspection. Therefore, finding the locations and sizes of

anodes and cathodes on the embedded steel in a reinforced concrete member is an inverse problem, generally defined as a boundary identification problem [27].

Since a continuum model is impractical (or impossible) to solve directly, most inverse problems use numerical solutions to solve a discretised model. Numerical techniques that are based on Galerkin approaches (e.g. finite element method) [15, 28, 29] and Fourier techniques [15, 30, 31] are widely used to solve these discrete inverse problems.

As the forward and inverse model equations are generally nonlinear, the parameter estimation (or boundary identification) problem constitutes a non-linear optimization problem, in which the objective is to find the parameter values that minimise a measure of badness of fit. Badness of fit is defined using a cost (or objective) function, usually as a least squares function or a weighted sum of squared residuals [15].

The most simple form of minimisation algorithm is the random search method [32, 33]. In this approach every possible combination of input variables is tried and the best solution is selected. This method is prohibitively computationally expensive and slow to converge. Computationally more efficient gradient based minimisation methods [27, 34–43] calculate the gradient of the cost function to be minimised and search for the minimum in the direction of steepest descent. These methods usually converge much faster than other methods, however, they can be computationally expensive and can have problems differentiating between local minima and the actual global minimum of the cost function [41–43].

Genetic algorithms and neural networks are numerical methods that adaptively search and learn the system behaviour. They are based on the procedures of genetic propagation and the workings of the human brain [44]. These methods can be used to model a system where there is little or no knowledge of the governing equations since they rely on random numbers and the statistical behaviour of a system to

predict the outcome. They can also be used in conjunction with a model as the minimisation algorithm to find the minimum of the cost function. They can be very robust when they are constructed properly but can also be less efficient than gradient based methods for minimisation purposes [45–48].

If the physical processes are not well understood, but the behaviour of the system can be observed for long periods of time, statistical methods of inverse modelling can be used. Methods such as recursive Bayesian estimation or Monte Carlo modelling [15, 49, 50] determine the most statistically feasible values for the parameters under investigation. These models can also be useful in cases for which there is a high degree of uncertainty inherent in the system. Like genetic algorithms and neural networks, statistical methods can be used either as the model, or in conjunction with an existing model to minimise a cost function.

Inverse problems are generally ill-posed [51] in the sense that solutions may not be unique. This non-uniqueness issue needs to be addressed by optimizing the number and locations of measurement points to obtain the global minimum of the cost function. However, these optimization algorithms may still not guarantee uniqueness; therefore, different executions of the model with different sets of measured data may need to be carried out to study the uniqueness of the solution [51].

Furthermore, solutions of inverse problems may exhibit non-physical oscillations, and in order to reduce these oscillations regularization schemes may need to be used. Regularization generally works by adding terms to the cost function to penalize oscillations. Depending on the frequency of the oscillations, these methods can apply a norm to the set of all possible solutions to find the minimum. Regularisation is usually used to eliminate noise and insures that the solution that is chosen is as regular and smooth as possible. A regularised solution is not necessarily the solution that best

fits the data, but it is the solution that conforms best to theoretical knowledge. Additional information about the system, such as experimentally determined bounds, theoretical knowledge and desired characteristics such as smoothness or shape can also be achieved with the use of regularization [52–59].

In summary, the majority of inverse modeling problems in corrosion are composed of a forward model, a cost or objective function that is used to evaluate the goodness of the solution and a minimisation algorithm that minimised the cost function to find the ideal solution. The choice of the forward model depends on the problem geometry, the governing equations and the available information. The cost function may or may not include regularisation terms and is minimised by an algorithm that is chosen based on robustness, computational expense and rate of convergence. These three aspects are balanced based on available resources, and the size and characteristics of the problem.

## 2.3 Inverse Modelling of Corrosion

Corrosion is a pervasive problem that affects many engineering applications. In corrosion problems where the corroding metal is easily observable, inverse modelling is generally not required. However, in cases for which the corroding metal is not accessible, inverse modelling can provide valuable information. Such cases include the corrosion of steel reinforcement in concrete, buried pipelines and other buried metallic structures, as well as containers, ships and other metallic structures that are in contact with sea-water, for which one side of the metal is submerged or not easily observable. This review is divided in two parts: inverse problems in corrosion other than steel corrosion in concrete and inverse problems dealing with the corrosion of steel in concrete.

### 2.3.1 General Corrosion Problems

In this review, works by Fasino and Inglese [20], Xin et al. [29], Yan et al. [60], Qui and Orazem [61], Wrobel and Miltiadou [62], and Lesnic et al. [14] are presented.

#### **Fasino and Inglese (1999) [13]**

This paper deals with the inverse problem of detecting corrosion damage on an inaccessible part of a thin metal plate from surface electrostatic data. A simplified model was used which incorporates a Robin boundary condition, which is a linear combination of a Dirichlet and a Neumann boundary condition. The Robin condition that was used is  $u_n + \gamma u = \phi$ , where  $\gamma$  is called the corrosion coefficient and is a function that varies with location,  $u$  is the potential and  $u_n$  is the normal gradient of the potential. The general corrosion problem is therefore simplified to the recovery of this single corrosion coefficient  $\gamma$  from data on the observed section of the metallic specimen.

Three methods of recovery of this coefficient were proposed, the thin plate approximation (TPA), the trigonometric Galerkin method, and the quasi-reversibility method. The TPA depends on the assumed physical characteristics of the physical system. In this method, the problem is expanded in terms of the thickness of the metal and higher order terms are neglected, resulting in an expression that can be solved analytically. Since this method was developed to deal with buried pipelines for which the thickness is much smaller than the length, this assumption holds true. The trigonometric Galerkin method begins with an expansion of the potential function over the domain by using the cosine-Fourier transform. The resulting equations are rearranged and simplified and the problem is then reduced to a discrete linear system by the use of the Galerkin method. The solution to this system is an approximation

for  $\gamma$ . The quasi-reversibility method was presented and discussed in a separate paper. This paper only discusses the discretisation of the quasi-reversibility equation using finite differences and the application the TPA to the discretised system.

The thin plate approximation is a simple and elegant solution to the problem, but it depends completely on the problem geometry, and the analytical solution is very difficult to generalise. Both numerical methods depend on assumptions and simplifications to reduce the computational expense. This reduces the time for convergence but also limits the use of the method for other problems. It also does not take advantage of the fact that computational power is much cheaper than it was when the paper was written. With the current computational power the cost of solving the non-simplified problem is not prohibitive.

#### **Xin et al. (2005) [29]**

The interior of a pipe is inaccessible to direct observation; therefore, the state of corrosion on the interior surface must be inferred from observed data on the exterior surface. In some cases, parts of the exterior may also be inaccessible, limiting the available data. Some pipes may also be thick enough that the thin plate approximation no longer holds true. Xin et al. developed their method to solve cases such as these. A Robin boundary condition is assumed for simplicity; however, the problem is defined as the recovery of the Cauchy data, namely the flux and the potential, at the unobservable boundary. This is done by the use of an iterative boundary element method.

Iterative boundary element methods are methods of successive boundary element forward solution with each iteration approaching the ideal solution until the objective function is reduced below an acceptable criteria. The main contribution of this paper is a method to simplify the iterative boundary element method so that it is reduced

to the solution of two linear equations per iteration. This greatly reduces the computational expense by taking advantage of known values from the problem geometry. A convergence analysis of the new method is also presented. The numerical experiments prove that the algorithm performs well as long as enough data are observed on the surface.

This approach is an elegant simplification of the iterative boundary element method. The main weakness of this approach is that the simplification is only applicable to the specific physical geometry of a pipe. The boundary element method in general is only effective and efficient when the boundaries compose the majority of the problem, when the surface to volume ratio is high, making it ideal for a pipe, but inefficient for any other problem geometries. This method also assumes that the steel is directly observable and that both the potential and the current density are measured on the observable surface.

#### **Yan et al. (2009) [60]**

This paper deals with corrosion on the interior of buried gas and oil pipelines. The pipelines were assumed to be pressurized which would affect both the method and rate of corrosion and the possible methods of detection. The flow of pressurized fluid through a pipeline adds the erosion effect to the the corrosion process. When combined, the rate of corrosion is much faster than either phenomenon by themselves. Besides increasing the rate of corrosion, the erosion effect would also tend to concentrate the effect of material loss in areas with greater friction between the fluid and the pipe wall (e.g. curves or bends). Since the pipeline was under pressure, it was possible to measure the working strain to use it to estimate material loss. The pipe was modeled using concentric circles, and the corrosion/erosion was measured by the eccentricity of the inner diameter compared to the outer diameter.

The finite element method was used to construct a forward model to solve the strain for given boundary conditions and system parameters. A cost function was constructed with two parts. the least squares data misfit measure to express the error between the observed strains and the calculated strains, and the punishment (or regularisation) function to constrain the solution depending on state and design variables. This total cost function was minimised by repeated forward solutions with the use of the conjugate gradient method [40]. The iterations were allowed to continue until the change between two successive iterations or the solution was less than a specified tolerance.

This method is both generalisable and fast, only the definition of a new cost function and forward model would be necessary to generalise this method to a different set of physical parameters. Since the assumption was made that the exterior of the pipe was directly observable and that all necessary measurements could be made, and since the resistivity was assumed to be constant and negligible, the problem geometry had little to no effect on the final solution. This would not be the case for the problem of the corrosion of steel reinforcement in concrete.

### **Qiu and Orazem (2004) [61]**

Most buried pipelines are protected from corrosion by use of coatings. If the coating is damaged, the exterior of the pipe will start to corrode at that location, which will cause a potential distribution through the soil above. In this paper, the inverse problem was the detection of these coating holidays on a buried pipeline from potential measurements taken on the surface of the soil.

Qiu and Orazem developed a three dimensional forward model using boundary element software packages to model soil surface potentials given the location of the anode and the coating properties. A least squares objective function was used with a

weighing function to take into account variations in the soil properties. This objective function was minimised using simulated annealing [63] since the observed data includes noise. The simulated annealing minimisation method is based on the annealing process as a metallic alloy cools to room temperature. The resulting crystalline structure corresponds to the minimum energy state of the system. The global minimum of the objective function can be considered as the minimum energy level of the numerical system. This method does not depend on the calculation of the gradient which makes it computationally cheap. It can also accept uphill steps so that it has less tendency to get caught in a local minima and is robust enough to deal with a significant level of noise.

The inverse problem was simplified by defining a single function for the resistivity of the surface coating that included the coating properties as well as specifying the location of the coating holidays. The soil was assumed to be homogeneous so that the surface potential distribution was only dependent on the condition of the coating.

This procedure used the boundary element method, meaning that the model would be inefficient if generalised to problems where the conditions over the domain have a significant effect on the final solution. However, the main weakness of this method is the lack of efficiency of the simulated annealing algorithm, which may take large number of iterations to reach convergence. Even though the computational expense per iteration is likely to be decreased by the use of the simulated annealing algorithm, the large number of required iterations means that the overall efficiency is poor. Qiu and Orazem accepted this inefficiency for the added robustness needed in their model.

### **Wrobel and Miltiadou (2004) [62]**

Cathodic protection [2] is used to mitigate the effects of corrosion for many different applications including buried pipelines and steel surfaces exposed to salt water. This

method of protection depends on the efficient placement of the sacrificial anodes and on the resulting protective cathodic protection film remaining undamaged.

The authors of this paper developed a forward model that used the boundary element method and included variables to control the placement of sacrificial anodes. The boundary conditions on which the forward solution depend included parameters that could be optimised in the inverse solution. An objective function was constructed using a least squares approach, normalised by the number of observed data points, and minimised using a genetic algorithm. The result was a three dimensional inverse model that could be used to determine the parameters of the boundary conditions, to optimise the placement of sacrificial anodes and to identify damages to cathodic protection.

A genetic algorithm mimics the evolutionary process, starting off with a set of "parent" solutions and generating "offspring" every iteration (or generation) using genetic operations that include a "mutation" process to incorporate randomness. These offspring are evaluated using a fitness function, and the offspring that are the most fit are used as the parents for the next generation [44].

The model can be used for a variety of steel structures: it was tested with a buried pipeline and a ship in salt water. Since the boundary element methods includes no information about the effect of the domain on the physical processes, the distance between the sensors and steel object was taken into account by using a function to simulate noise. The inverse model was compared with the forward model using identical twin numerical experiments, and the genetic algorithm performed very well, especially if the distance between the sensors and the steel was small enough to reduce the simulated noise.

The advantage of this system is its robustness and its generality. It is very difficult for this system to get caught in a local minima since the original population covers

the entire spread of possible solutions and since the genetic operations incorporate random elements. However, the method is slow because multiple solutions need to be evaluated for each generation, and a large number of generations is necessary to reach an optimal solution. Since the boundary element method was used, more work would need to be done on the assumed noise distributions to fully account for the properties of all materials through which measurements might be made.

### **Lesnic et al. (2002) [14]**

The method developed by Lesnic et al. determined the state of corrosion on an inaccessible boundary by determining the shape of that boundary. Instead of attempting to determine the potentials on a fixed boundary, this method assumed an analytical function on the surface of the inaccessible boundary and then determined the shape of the boundary to represent the process of material loss; hence the state of corrosion can be determined by comparing the corroded shape with the original shape. Cauchy data (potentials and current densities) were both assumed to be measurable on the accessible boundary, with one variable being measured and one variable being calculated.

The boundary element method was used since the problem was posed as a boundary value problem and since the boundary element method does not require the mesh to change shape as the unknown boundary changes shape. This model was used to solve for the potential (or the current density) on the observed boundary depending on the shape of the unknown anodic boundary. The goodness of the solution was evaluated with a two-part objective function. The first part, the data misfit measure, is a least squared determination of the error between the predicted values and the calculated values, and the second part is a Tikhonov regularisation term [54] with a regularisation coefficient defined as the difference between the calculated coordinates

for each node. The method was tested using a circular domain with only the upper part of the domain being observable and the corrosion and material loss occurring on the unobservable part. All anodic regions were assumed to have lost material and to be detectable by determining where the corroded shape differs from the uncorroded shape.

This method is flexible since it can be used to determine either the current density or the potential on the unknown boundary. It can also be used for many different problem geometries. However, it assumes that the resistivity is negligible and that the shape of the unknown boundary has no effect on the corrosion process. It also assumes that both the potential and current density can be directly measured from the observable portion of the corroding material.

### **2.3.2 Corrosion of Steel in Concrete**

Although there is limited work on the inverse modeling of the corrosion of reinforcing steel in concrete, some notable contributions exist and are reviewed in this section.

#### **Leelalerkiet et al. (2004) [25]**

A numerical model was constructed to represent a physical rectangular concrete experimental setup. Two sections of reinforcement were run lengthwise and four sections were run widthwise through the concrete sample resulting in a grid. To initiate corrosion, half of the rectangular sample was constructed with pure water in the concrete mix and the other half was constructed with a 3% NaCl solution. The cover between the reinforcing bars and the surface was small and equal in thickness above, below and to the sides. Potential readings were made on the surface of the concrete after suitable periods of time to allow corrosion to occur, and the numerical analyses were run on those readings. The results were then compared to the observed data and

to the actual state of corrosion which was later determined by visual inspection of the reinforcement. This helped to determine the effectiveness of both the methods of measurement and the numerical models themselves.

The boundary element method was used since the cover thickness was small and uniform. Both a forward model and an inverse model were constructed. The inverse model was used to calculate the potential on the steel/concrete interface by calculating the current density on the surface and modifying it by a factor to take into account the resistivity and another factor to take into account the spacing between nodes. Resistivity was taken into account as an average applied homogeneously over the entire concrete domain. While this is an approximate method, it is justifiable since the resistivity is known and the cover thickness is uniformly thin.

When compared to the actual surface potential distributions and locations where corrosion was occurring, both the forward and inverse models performed well. The main weakness of the inverse model is the approximation that was used to relate the surface and interface potentials. The model also makes use of the boundary element method which is only effective for small volumes and large surfaces; it is difficult to generalise the model to other geometries. No information was given as to the method of solution of the boundary element models, so it is assumed that either a package, or the simplest possible minimisation algorithm was used. The forward model did not perform as well, because of the assumptions that were made about the location of the anodes. The entire area that had been treated with salt water was assumed to be anodic, and only that area, an assumption that proved to be false.

### **Ridha et al. (2001) [23]**

This paper deals with the inverse problem of finding the anodic areas on a two-dimensional reinforcing grid. The grid was assumed to be uniform and the cover

thickness was assumed to be thin. The forward solution was constructed using the boundary element method and the inverse model minimised a least squares cost function which compared the calculated surface potentials with the surface potentials generated by the forward problem in twin numerical experiments. A genetic algorithm was used to minimise the cost function, where the location and occurrence of corrosion was encoded into a binary string. Since in the interests of accuracy, the mesh on the reinforcement grid should be small, and since a small grid would lead to very large binary strings, a multistep algorithm was used.

The domain was discretised into a coarse grid and each segment had the possibility of being labeled as either corroding or non-corroding. Each string represents one possible solution and its fitness was determined using a fitness function. Since the cost function decreases as the solution approaches congruence with the data, and since the fitness should increase as the solution approached the true solution, the inverse of the cost function was used as the fitness function. The algorithm was run until either the cost function dropped below a specified tolerance for a specific solution or a maximum number of generations occurs. The next step of the algorithm discretised the areas where corrosion was found to be occurring with a finer mesh and ran the algorithm again on each section until the same convergence criteria were met. As many steps were taken as was necessary to refine the mesh to the point where each segment represented one junction of the reinforcement grid.

In the coarse grid steps, each segment represented many junctions between reinforcing bars. However, if the segment was encoded as corroding, only the middle junction was considered to be corroding for the sake of the forward solution and the evaluation of the cost function. This was to ensure that even small areas of corrosion could be detected by this algorithm.

This algorithm performed well and was very efficient. However, since the data

were encoded as a binary string, the only information this method gives was the occurrence or non-occurrence of corrosion; no information on the potentials at the steel/concrete interface or about the rate of corrosion was obtained. The forward solution is a boundary element method solution using experimentally determined polarisation curves. While the use of these curves simplifies the calculations and the linearisation of the curves simplifies them even more, these curves are only exact for the experiments that constructed them, they are not general in scope. The cover thickness is also assumed to be small and constant above and below the reinforcement, and the resistivity of the concrete is not taken into account at all.

**Ridha et al. (2005) [24]**

Current corrosion detection methods rely on the potential at the surface of the concrete. A new method of measurement was proposed where magnetic flux would be measured instead by using a Superconducting Quantum Interference Device (SQUID) [64] sensor. A current was impressed on the reinforced concrete to increase the magnetic flux to levels that were more easily detectable and the resulting magnetic field was measured. Since the current flow in the reinforcement is dependent on the size, number and location of the corroded sections, the resulting magnetic flux contains all the necessary information to determine the state of corrosion. Some simplifications were made to the calculations including assuming a high magnetic permeability for concrete and neglecting the ferromagnetic contributions of the reinforcement. The reinforcement was discretised into sections and each section was assumed to either be corroding or non-corroding.

The inverse problem was solved by minimising a least squares cost function comparing the calculated and observed data. In this study, the minimisation was accomplished by calculation of the value of the cost function for every possible combination

of corroding or non-corroding sections of reinforcement and selecting the configuration that had the lowest cost. Depending on whether a magnetometer or a gradiometer was used, the cost function either compared the magnetic flux density or the gradient magnetic flux density. The advantage to the gradiometer is that it does not require a shielded environment to achieve accurate results. The forward problem is implemented using the boundary element method to calculate the potentials and the current densities on the surface which are then converted into magnetic fluxes by the use of the Biot-Savart law.

This method was used to find both small anodes and deep corrosion in a second layer of steel. It is an elegant method that shows promise. However, until the future work is done, and until the simplifications that were introduced in the calculations are studied, this method remains a promising theoretical approach. This method also uses the same boundary element method based forward solution as the previous paper with the same issues.

### **Kranc and Sagues (2006) [26]**

This paper presents an inverse model for the calculation of potentials and current densities at the steel/concrete interface verified by an idealised physical experimental setup. The inverse problem was formulated by transforming the boundary value problem into an initial value problem and using an approximation for the current density. Both the forward and inverse problems were solved using the finite difference method. This method was used to determine both the potential distribution and the state of polarisation.

The potential distribution at the reinforcement was determined by providing the inverse model with the potential distribution on the surface of the concrete. The

forward model was also used to generate data for the inverse model in a twin numerical experimental setup. The physical experimental set up was a cylinder with a single reinforcing bar running through the center with an area of known size undergoing corrosion. The algorithm successfully located the area undergoing corrosion and predicted the potential and current density.

The state of polarisation was determined using a series of independently controlled counter electrodes along the opposite side of the concrete cylinder. The metal concrete interface at the counter electrodes was assumed to not be polarised. This allowed the current density at the interface to be directly inferred and used in the model. The model performed well when tested with both experimental and simulated data.

While this method provides both information about the state of polarisation and the potential distribution, it is very limited in scope and applicability. The inverse model depends on a transformation and an approximation, which simplifies it considerably, but also limits its applicability.

## 2.4 Summary

As demonstrated in this review, although the literature on the general topic of inverse modelling is quite developed, literature on the use of this approach for the identification of the locations of anodes and cathodes on corroding steel reinforcement from the measurements or observations on the accessible surfaces of concrete is new and sparse. The existing work is mainly based on genetic algorithms, which may not be necessarily based on the phenomenological understanding of the process of steel corrosion in concrete. In addition, these models are mostly developed using the boundary element method, which has limitations in the definitions of different problem geometries and materials properties of the domain of interest. A need for

a more systematic inverse modelling algorithm - for example, one that is based on a gradient based minimisation method (e.g. conjugate gradient method) and that is built using the finite element analysis technique - is evident.

## Chapter 3

# Formulation of the Inverse Modelling Algorithm

### 3.1 General

This chapter presents the formulation of the inverse modelling algorithm that was developed and implemented in this research. The algorithm is based on the minimisation of the cost function using the conjugate gradient method [40]. The chapter starts with the formulation of the forward problem, which is an intermediate step in the inverse solution algorithm and is also used as the tool to generate observed data for the identical twin numerical experiments. The inverse formulation includes the description of the cost function and its gradient, the conjugate gradient method and the final algorithm. Initial conditions, starting values and the convergence criterion are also discussed in this chapter. The Dolfin software development package from the FEniCS project [65] that is used to code the forward and inverse modelling algorithms is introduced. Finally, a sample inverse analysis is presented.

## 3.2 Forward Model

The electrical potential distribution,  $\phi$ , in concrete due to the corrosion of the reinforcement can be determined by solving Laplace's equation:

$$\nabla^2 \phi = 0 \quad (3.1)$$

with boundary conditions defined on the anodic and cathodic surfaces of the reinforcement as well as on other boundaries of the domain, as illustrated in Figure 3.1:

$$\phi_a = \phi_{Fe}^0 + \beta_a \log \frac{i_a}{i_{oa}} \quad \text{on } \Gamma_a \quad (3.2)$$

$$\phi_c = \phi_{O_2}^0 + \beta_c \log \frac{i_c}{i_{oc}} - \frac{2.303RT}{z_c F} \log \frac{i_L}{i_L - i_c} \quad \text{on } \Gamma_c \quad (3.3)$$

$$\frac{\partial \phi}{\partial n} = 0 \quad \text{on } \Gamma_{ct} + \Gamma_{cs,1} + \Gamma_{cs,2} \quad (3.4)$$

where

$\phi_{Fe}^0$  = standard equilibrium potential for the oxidization of iron (V)

$\phi_{O_2}^0$  = standard equilibrium potential for the reduction of oxygen (V)

$\beta_a$  = anodic Tafel slope [V/dec]

$\beta_c$  = cathodic Tafel slope [V/dec]

$i_a$  = anodic current density [A/m<sup>2</sup>]

$i_c$  = cathodic current density [A/m<sup>2</sup>]

$i_{oa}$  = anodic exchange current density [A/m<sup>2</sup>]

$i_{oc}$  = cathodic exchange current density [A/m<sup>2</sup>]

- $R$  = universal gas constant [ 8.314 J/mol.K]  
 $F$  = Faradays constant [ 96500 C/mole]  
 $z$  = number of electrons in the reaction  
 $T$  = temperature [K]  
 $i_L$  = limiting current density [A/m<sup>2</sup>]  
 $n$  = direction normal to the equipotential lines.

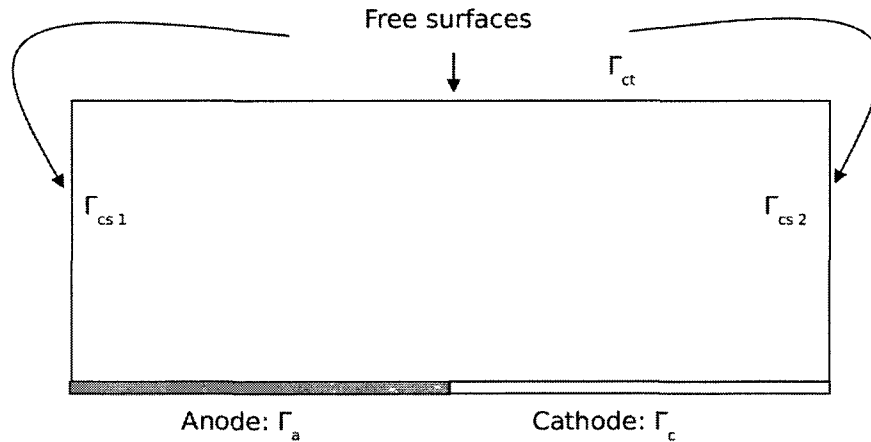


**Figure 3.1:** Boundary conditions for the forward problem.

Current density at anodic and cathodic surfaces is calculated locally at every discretization node on the steel surface by applying the Ohms law (Equation 3.5):

$$i = -\frac{1}{\rho} \frac{\partial \phi}{\partial n} \quad (3.5)$$

where  $i$  is the current density [A/m<sup>2</sup>] and  $\rho$  is the electrical resistivity of concrete [ $\Omega$ -m].

The dependence of the boundary conditions (3.2) and (3.3) on Equation (3.4) requires a non-linear solution algorithm using Picard iterations, which is described in detail elsewhere [4].

## 3.3 Inverse Model

### 3.3.1 The Cost Function

The inverse problem is described as the identification of the anodic and cathodic boundary conditions on the surface of the reinforcement ( $\Gamma_a + \Gamma_c$ ) from half-cell potential measurements on the concrete surface ( $\Gamma_{ct}$ ). The inverse model requires the minimization of a cost function,  $J$ . This function is called a cost function because it is used to describe the error in the system and to assign penalties, or costs, to solutions that are undesirable. The cost function is also sometimes called the objective function because it is used to describe the objectives of the problem and to determine which solution meet the objectives. The cost function can be expressed by equation (3.6):

$$J(\phi) = J_D(\phi) + \omega J_R(\phi) \quad \text{on the concrete surface} \quad (3.6)$$

where  $J_D$  is the data misfit measure,  $J_R$  is the model character measure (regularisation function) and  $w$  is the weighing function determining the contribution of the regularisation function to the cost function as a whole.

The purpose of the model character measure,  $J_R$ , is to introduce a way to evaluate the solution on the basis of characteristics, such as smoothness or conformity to experimentally determined bounds. It also provides a way to force the solution towards a particular shape or to eliminate undesirable traits. The regularisation technique

that is used in this research is discussed later in this chapter. Until then, this formulation will assume that the cost function is only composed of the data misfit measure, which can be written as (3.7):

$$J_D(\phi) = \sum_{k=1}^{N_s} (\phi_{obs}^k - \phi_s^k)^2 \quad \text{on } \Gamma_{ct} \quad (3.7)$$

where  $N_s$  is the number of surface nodes at which the half-cell potential readings are carried out,  $k$  is the index for counting,  $\phi_{obs}$  is the half-cell potential measurements on the concrete surface and  $\phi_s$  is the half-cell potential predictions on the concrete surface.

### 3.3.2 The Gradient of the Cost Function

Although there are many methods of minimization for the cost function [33, 66.67], in this research, the conjugate gradient method [40] is used for the minimization of the cost function. The conjugate gradient method requires the determination of the gradient of the cost function, which can be used for detecting the direction of the steepest descent towards the minimum. The gradient of the cost function (which is defined on the surface of the concrete) with respect to the change in potential at the interface between the steel and concrete is calculated as:

$$\frac{\partial J}{\partial \phi_i} \approx J(\phi_s + \partial \phi_{s,i}) - J(\phi_s) \quad (3.8)$$

where  $\partial \phi_i$  represents the change in potential on the interface and  $\partial \phi_{s,i}$  represents the change in potential on the surface with respect to the change in potential on the interface. This equation is a tangent linear approximation and is only valid over a small interval around the current value of  $\phi_s$ . A tangent linear approximation is one

where the slope of the function is taken at a specific point and the true function is approximated by a linear function with that slope passing through that point. Since this linear function is tangent to the true function at that point, it is called the tangent linear approximation. Linearity in this case refers to the shape of the surface. If the surface can be reasonably approximated by a plane in however many dimensions that there are in the problem, then the problem is considered to be linear. Alternatively, linearity refers to a linear relation between the effect of each variable and the effect on the main function. Since the relation between the value of the cost function and a small change in the potential of a single node on the interface is not linear, this problem is considered to be extremely non-linear.

Combining equations 3.7 and 3.8 we obtain:

$$\frac{\partial J}{\partial \phi_i} = \sum_{k=1}^{N_s} [\phi_{obs}^k - (\phi_s + \partial \phi_{s,i}^k)]^2 - \sum_{k=1}^{N_s} (\phi_{obs}^k - \phi_s)^2 \quad (3.9)$$

Simplifying and rearranging:

$$\frac{\partial J}{\partial \phi_i} = \sum_{k=1}^{N_s} \underbrace{(\phi_{obs}^k - \phi_s - \partial \phi_{s,i}^k)}_A^2 - \sum_{k=1}^{N_s} \underbrace{(\phi_{obs}^k - \phi_s)}_A^2 \quad (3.10)$$

$$= \sum_{k=1}^{N_s} (A - \partial \phi_{s,i}^k)^2 - \sum_{k=1}^{N_s} A^2 \quad (3.11)$$

$$= \sum_{k=1}^{N_s} (A^2 - 2A\partial \phi_{s,i}^k + (\partial \phi_{s,i}^k)^2 - A^2) \quad (3.12)$$

Therefore,

$$\frac{\partial J}{\partial \phi_i} = -2 \sum_{k=1}^{N_s} (\phi_{obs}^k - \phi_s) \partial \phi_{s,i}^k + \sum_{k=1}^{N_s} (\partial \phi_{s,i}^k)^2 \quad (3.13)$$

In practice, the  $\partial \phi_{s,i}$  term is drawn from the sensitivity matrix which related perturbations on the interface to perturbations on the surface. There are different

methods for calculating sensitivity [27, 68], in this formulation the sensitivity matrix is obtained by the method of direct perturbation by successively applying a small perturbation to a single node on the steel/concrete interface and solving the forward problem to calculate the changes in potentials for each of the nodes on the concrete surface. The change in potential at each surface node for a perturbation of a single interface node forms one row of the sensitivity matrix. Therefore there are as many rows in the sensitivity matrix as there are nodes on the interface and as many columns as there are nodes on the concrete surface. Since the domain is discretised with the same number of nodes on the surface of the concrete as on the interface, the sensitivity matrix is square. This means that each  $\partial\phi_{s,i}^k$  term can be expressed as:

$$\partial\phi_{s,i}^k = \sum_{j=1}^{N_i} S^{kj} \quad (3.14)$$

where  $S$  is the sensitivity matrix.

The cost function can also be considered as the sum of the residuals,  $r^k$ . A residual is the difference between the current solution and the true, or target, solution. In this case, the residuals are the error function at each surface node. The cost function can therefore be expressed as:

$$\frac{\partial J}{\partial\phi_i} = \sum_{k=1}^{N_s} r^k \quad (3.15)$$

Using equations 3.14 and 3.13, each residual can therefore be expressed as:

$$r^k = -2(\phi_{obs}^k - \phi_s^k) \sum_{j=1}^{N_i} S^{kj} + \sum_{j=1}^{N_i} (S^{kj})^2 \quad (3.16)$$

The residuals equation is much more useful since it gives information about the error of each node. This allows each node to be individually adjusted to reach the optimal final solution.

### 3.3.3 Conjugate Gradient Method

To find the potentials on the steel/concrete interface, the cost function is minimised by use of the conjugate gradient method. This method works by iteratively finding new solutions that minimises the cost function following the direction that points most closely toward the minimum.

The simplest gradient methods use the negative of the gradient as the direction of search. This is called the direction of steepest descent. The problem with this method is that, unless the function is perfectly symmetric, the direction of steepest descent does not point towards the minimum of the function, it only points in the general area of the minimum requiring several iterations to reach the minimum. The answer is conjugate directions. In essence, the method of conjugate directions transforms the problem into a space where it is perfectly symmetric to find the search direction. This results in a direction of search vector that points directly towards the minimum. However, the method of conjugate directions requires that previous search directions be stored in memory. The conjugate gradient method used the residuals to determine the search directions which significantly improves the memory requirements and the computational simplicity of the method. The derivations and detailed explanations of all these methods is presented by Shewchuk [40].

The conjugate gradient method can be expressed as:

$$\phi_i^{n+1} = \phi_i^n + \alpha^n d^n \quad (3.17)$$

where  $n$  is the current iteration step,  $\alpha^n$  is the step size and  $d^n$  is the direction of search [27]. The direction of search is found using:

$$d^n = r^n + \gamma^n d^{n-1} \quad (3.18)$$

where  $r^n$  is the residual and  $\gamma$  is a scalar coefficient.

There are two main expressions for  $\gamma$  [40], the Fletcher-Reeves equation and the Polak-Ribiere equation, which are given by the following two equations respectively:

$$\gamma_n^{FR} = \frac{r_n^T r_n}{r_{n-1}^T r_{n-1}} \quad (3.19)$$

$$\gamma_n^{PR} = \frac{r_n^T (r_n - r_{n-1})}{r_{n-1}^T r_{n-1}} \quad (3.20)$$

The Fletcher-Reeves equation is considered to be more robust, while the Polak-Ribiere equation has been shown to converge faster in some cases [40]. The residuals in both equations are calculated using equation 3.16.

In the standard linear conjugate gradient method, the step size,  $\alpha$ , can be calculated directly by use of the conjugate gradient equations [40]. The tangent linear approximation of the cost function is linear with respect to the potential at each interface node. It is not, however, linear with respect to the value of  $\alpha$ . This means that the simplified equations no longer apply and that some sort of minimisation algorithm is required to minimise the cost function with respect to  $\alpha$ . Since the shape of the cost function is an approximation, the minimisation need not be extremely precise; the most computationally simple minimisation algorithm is desired, not the most accurate. While it is possible to find the exact minimum of the cost function by the use of methods such as Newton-Raphson, or other minimisation algorithms, a simple quadratic approximation is chosen here for its simplicity.

The quadratic interpolation algorithm takes three points a certain distance apart, finds the quadratic that best fits through these three points and then returns the minimum of that quadratic. The first point is the value of the cost function based on the current estimate of the interface potential distribution ( $\phi_i^n$ ); or an evaluation of the conjugate gradient equation (Equation 3.17) with  $\alpha$  set to zero. The second and

third points are chosen by selecting two equally spaced values for  $\alpha$  and reevaluating the conjugate gradient equation (Equation 3.17) to get two different estimates for the next iteration of the interface potential distribution. The forward solver is then used to convert these estimates to surface potential distributions which can be used to reevaluate the cost function. This gives three points with a value for  $\alpha$  corresponding to a value for the cost function. The quadratic interpolation is used on these three points to find the value of  $\alpha$  that locally minimises the cost function. The interval between the three points needs to be optimised. A preliminary analysis on the optimisation of the quadratic approximation method will be presented in the following chapter.

### 3.4 Regularisation

To be effective, the model characteristic measure, or regularization vector, part of the cost function, ( $J_R$ ), needs to be expressed as a cost per node. That way each node can be adjusted individually to conform to the applied constraints. This is done by simply subtracting the current solution from a selected regularisation function such that

$$J_R^n = \phi^n - \phi_R \quad (3.21)$$

where  $n$  is the current iteration and  $\phi_R$  is the regularisation function. The result is not squared, nor is the absolute value taken, so that the cost function will incorporate a measure of the direction of the error as well as the magnitude.  $J_r$  is then linearly combined with the data misfit measure (Equation 3.6) and when the cost function is minimised, the difference between the regularisation function and the current solution is also minimised, forcing the solution into the desired shape. The contribution of the regularisation term in the cost function is controlled by the use of a regularisation

coefficient  $\omega$  (Equation 3.6). The difficulty comes in selecting which function to use as  $\phi_R$ . For this study, two different functions were investigated, the smooth curve and the idealised solution.

The smooth curve was smoothened using the five point average method, a simple method which assigns a point the average value of itself and the two points preceding and following it. Since there are two points before, two points after and the point under consideration, for a total of five points, this is called the five point average method. The method is run twice, once in one direction, starting at the first node, and once in the opposite direction, starting at the last node. This results in a curve that is similar to the current estimation for the interface potential distribution except with reduced oscillations. Since this function is based on the current solution, it changes every iteration and adapts to the shape of the solution. No information about the final shape of the solution is required to construct this function making it simple and robust.

The purpose of the idealised solution is to construct a distribution of potentials along the steel/concrete interface that is as close to the final solution as possible. To implement this, the points of inflection in the plot of the observed data are calculated. A square pulse function is then constructed with the standard anodic equilibrium potential in the anodic region between a pair of inflection points and the standard cathodic equilibrium potential in the cathodic regions between two inflection points. This square function is then recombined with the observed data using an idealisation coefficient,  $\kappa$ . The idealisation coefficient modifies the observed data according to a ratio from 0 to 1, in which 0 is the observed data and 1 is the square function.

### 3.4.1 Initial Conditions and Starting Values of the Analysis

Since during the first iteration, the  $\phi_i$  and  $d^n$  terms in equation 3.17 will not yet have been calculated, suitable starting values must be selected. The search direction vector is constructed by assuming  $\gamma = 0$  so that  $d^0 = r^0$  where  $r^0$  is the initial vector of residuals calculated according to Equation 3.16.

The initial value refers to the initial assumed shape of the potential distribution on the interface,  $\phi_i^0$ . This distribution can be assumed to be constant at any value or vary according to any function or distribution. The size of the perturbation used to construct the sensitivity analysis also needs to be determined. A preliminary analysis on the initial values and starting conditions will be presented in the following chapter. One of the initial potential distributions that is investigated is the idealised solution that was originally constructed for the regularisation process.

### 3.4.2 Convergence Criterion

When the cost function is sufficiently small, the error can be assumed to be negligible and the algorithm can be considered to have converged. The cost function (Equation 3.7) is evaluated at each iteration and compared to an acceptable error. The smaller the acceptable error, the better the solution will reflect the true state of the system. A preliminary analysis on the convergence criterion will be presented in the following chapter.

## 3.5 Implementation: FEniCS / Dolfin framework

The forward modelling algorithms developed in this research have been coded using an open source finite element software library from the FEniCS project [65]. The FEniCS project is the outcome of a long-term collaboration by scientific software

developers from around the world to create an open source library to help the scientific community in the development of customized finite element codes.

The FEniCS project is composed of several complementary sub-libraries that build on each other. The libraries are coded in two programming languages: Python and C++. The C++ programming library was used in this research since the coding for the inverse modelling algorithms (e.g. conjugate gradient iterations, etc.) were to be carried out in C++ as well.

The main finite element library from the FEniCS project used in this research is the Dolfin package [65]. This package allows the solution of a finite element problem through built-in domain classes and boundary condition classes. The governing equations to be solved over the domain can be directly solved using built-in solvers. This way of solving finite element problems is both flexible and simple and allows the implementation and integration of the inverse modelling algorithms.

The FEniCS libraries are also compatible with the Unified Form Language (UFL) [69]; therefore, codes for many algorithms that are part of a typical finite element solution process can be generated automatically (in C++) with minimum programming effort. For example, a UFL code can be written to define the governing equation of the problem, usually a PDE (in the current research, the Laplace's equation), which can then be compiled with the Unified Form Compiler (UFC) that comes with the FEniCS package. This compilation automatically generates a C++ class defining the problem which can then be used with the Dolfin package. The geometry and discretization of the domain and the boundary conditions can be either specified or imported from a third-party mesh generation software into built-in data classes. Sink/source terms and boundary conditions can be defined as functions and can be applied to previously defined boundaries. The finite element calculations are handled by a solver class which takes the domain, the governing equation, any boundary conditions and

source terms as input and outputs the solution at every node in the domain. Gradients, (in the research: current densities) of the field variable (in this research: electric potentials) can be calculated in a similar manner. The inverse modelling algorithms call the forward solver to check the convergence of the system and the gradient solver to find the needed components for the conjugate gradient method.

Using this framework, the non-linear forward solution of the Laplace's equation with the specified boundary conditions as described in section 3.2 is carried out using Picard iterations [71]. The benchmark verification of the forward solution algorithms that are developed in this research has been carried out by comparing the solution of numerous cases with the solutions of a well-established commercial finite element package, COMSOL [70] and a specialized finite element software for modelling steel corrosion in concrete, CONDUR [71]. These extensive benchmark verification studies are not presented in this thesis.

A detailed summary of the classes that make up the inverse model, including the automatically generated Dolfin classes, and the inter-dependencies is listed in the appendices.

### **3.5.1 Inverse Solution Algorithm**

1. Directly calculate the sensitivity matrix by applying a small perturbation to each node on the steel/concrete interface in turn and solving the forward problem to calculate the potential distribution for each of the nodes on the concrete surface caused by the perturbation of the single interface node. The change in potential at each node on the concrete surface for the perturbation of a single interface node forms one row of the sensitivity matrix.
2. Choose the perturbation size, convergence criteria and the interval size for the

quadratic approximation of  $\alpha$  and set the starting value. Set any other variables that may arise from the finite element implementation, such as domain size and element type.

3. Begin Conjugate Gradient iterations.
4. Calculate the residual vector,  $r$ , for each surface node using equation 3.16.
5. Calculate  $\gamma$  using either equation 3.19 or equation 3.20.
6. Calculate a new search vector,  $d$ , using equation 3.18.
7. Calculate  $\alpha$  using quadratic approximation to minimise the cost function.
8. Solve the conjugate gradient equation (3.17) to find a new potential distribution on the interface between steel and concrete.
9. Evaluate the cost function using equation 3.7 and compare it to the chosen acceptable error norm to determine convergence.
10. If convergence is reached, end the iterations, if not repeat from step 3 until convergence.

## 3.6 Identical Twin Numerical Experiments

The corrosion of rebar in concrete is a long-term process, and physical experiments that test this phenomenon have inherent difficulties. These difficulties originate from the fact that the control of some of the important parameters in corrosion tests, such as concrete and steel properties and environmental parameters such as relative humidity and temperature, is extremely challenging. Even in well designed and well

controlled environments and under accelerated conditions (that may reduce the duration of these tests from years to months), the collected experimental data contains a high degree of uncertainty. The uncertainty in this data is also related to the inherent deficiencies in the existing corrosion monitoring devices [10, 11].

In the current research, the developed inverse modelling algorithm requires that the potential measurements on the concrete surface be taken as input. The model then outputs the potential distribution on the interface from which the location of the anodic and cathodic regions can be determined. Even if one assumes that difficulties associated with physical experiments are overcome (i.e. duration, parameter control and deficiencies of corrosion measurement devices) and that reliable test data can be obtained, it is not practical, and in most cases, not even possible, to accurately determine the anodic and cathodic locations without exposing the steel surface and destroying each test sample. This issue, which is a common problem in inverse modelling studies, can be overcome by using identical twin numerical experiments.

When using identical twin numerical experiments, the solution of a well-posed and validated forward model, for which all boundary conditions and system parameters are defined, is used to generate input data for the inverse problem and to verify its predictions. For the case of corrosion of steel in concrete, forward models that receive the locations of anodic and cathodic areas on the steel surface as input and predict the potential distribution within the domain of analysis have been shown to produce reliable and accurate predictions [1, 4, 12, 26]. Therefore the use of a forward model to generate data for the inverse model is an accepted practice in the field of corrosion research.

The use of identical twin numerical experiments also has the advantage that a wide variety of conditions can be examined. The forward model can be used to generate data using a large number of parameters (e.g. concrete resistivities, cover

thicknesses, etc.) and can vary each parameter separately while keeping the other parameters constant, something that would be extremely difficult, if not impossible, to do using physical experiments. In this way, the effect of a single parameter can be studied to better understand both the physical phenomenon and the performance of model.

### 3.7 Sample Analysis

This section presents a sample analysis to demonstrate the functionality of the developed inverse modelling algorithm. The domain of the analysis was rectangular with the boundary conditions illustrated in Figure 3.1. The initial potentials on the steel surface were assumed to be zero, an arbitrary selection. Ideally, the inverse algorithm should be able find a potential distribution on the steel/concrete interface regardless of the assumed initial values. Table 3.1 provides all input data parameters that are used both in the forward and inverse models.

Convergence of the sample analysis case was achieved in 198 iterations with a run time of 73.24 seconds using a Pentium(R) Dual-Core CPU T4200 @ 2.00 GHz with 2 GB of memory. All subsequent tests were run on the same computer. Even though the starting potentials on the steel surface was arbitrarily chosen to be zero, the model still converged to a reasonably good approximation of the shape of the desired forward solution (Figure 3.2). This shows that the algorithm is fairly robust and is not very dependent on the starting conditions.

The results of each iteration were output from the program and were compared to each other to determine the behaviour of the model as it approached convergence. As can be seen from figure 3.3, the algorithm converges fairly rapidly from the initial starting condition to a shape that closely approximates the final solution. The

**Table 3.1:** Input data for the sample analysis.

Forward Model	
Resistivity, $\rho$ ( $\Omega$ -m)	1500
Anodic Tafel Slope, $\beta_a$ (V/dec)	0.090
Cathodic Tafel Slope, $\beta_c$ (V/dec)	-0.180
Anodic Equilibrium Potential, $\phi_{Fe}^0$ (V)	-0.78
Cathodic Equilibrium Potential, $\phi_{O_2}^0$ (V)	0.16
Anodic Exchange Current Density, $i_{oa}$ (A/m <sup>2</sup> )	0.0003
Cathodic Exchange Current Density, $i_{oc}$ (A/m <sup>2</sup> )	0.00001
A/C ratio	0.5
Anode Location	middle
Temperature (K)	298
Picard Iteration Weight [71]	0.001
Inverse Model	
Domain size (m)	$1.2 \times 0.16$
Element size (mm)	$10 \times 10$
Element style	crossed diagonals
Acceptable error	$1 \times 10^{-8}$
Maximum number of iterations	5000
Initial condition	constant zero potential

remainder of the iterations are a refining of the solution to achieve the desired degree of accuracy.

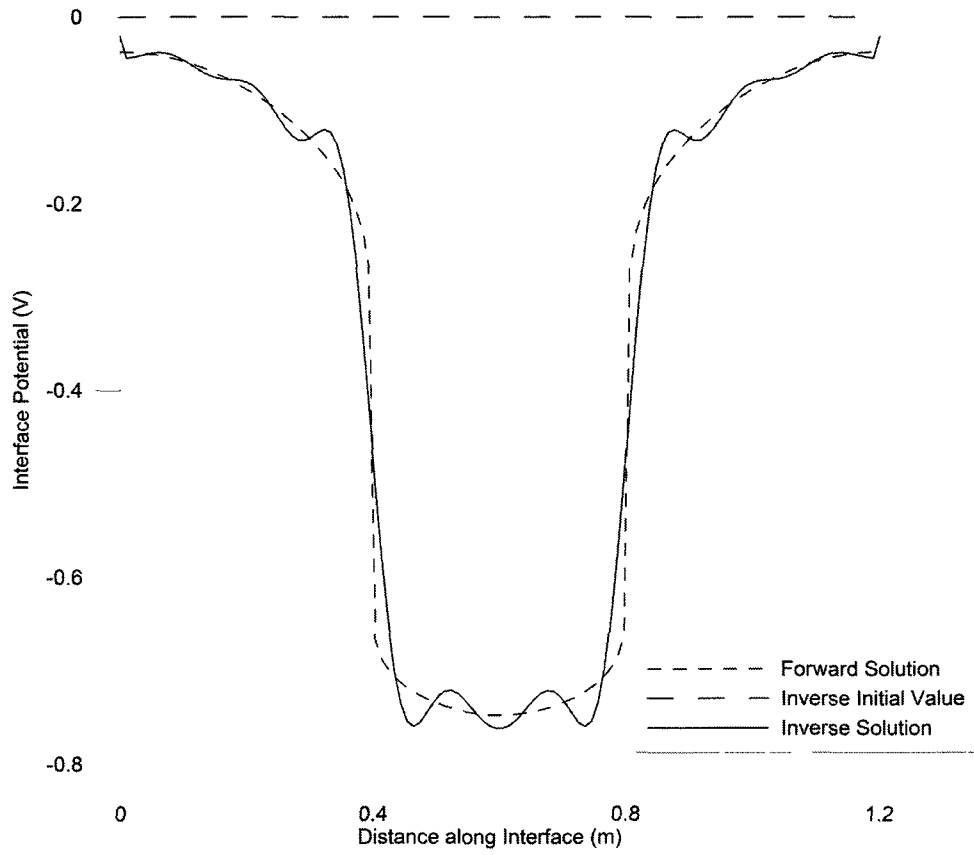


**Figure 3.2:** Comparison of the results of the sample analysis to the initial value and the target forward solution.

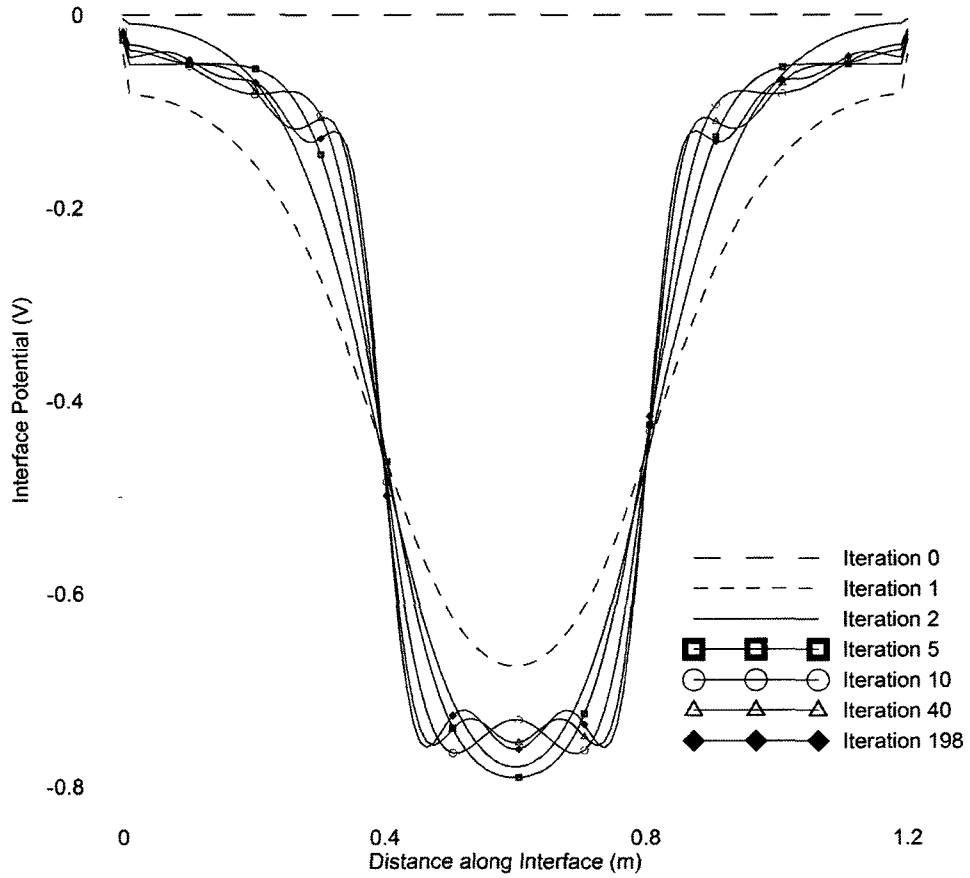


**Figure 3.3:** Convergence of the sample analysis. Comparison of the intermediary solutions at different iterations to show the progression of the solution.

## Chapter 4

# Studies on Systems with a Localized Single Anode

### 4.1 General

Typical localized (e.g. pitting) corrosion on the reinforcement in concrete can be modelled by a single anode surrounded by cathodic surfaces. From a computational point of view, a localized single anode is the most basic corrosion scenario to study. The ability to adequately detect localised corrosion is also very important in a numerical model. Therefore, in this chapter, the performance of the developed inverse model is investigated using identical twin numerical experiments on steel reinforcement in concrete with a localized single anode.

The investigation is carried out on a single-reinforcement-in-concrete system discretized into a two-dimensional rectangular domain. As presented in Chapter 3, the developed inverse model depends on several parameters. Some of these parameters are used in the numerical operations of the algorithm (e.g. discretization technique, the step size in the conjugate gradient method, initial values); others are related to the analyzed system (e.g. A/C ratio, concrete resistivity, concrete cover thickness).

To study both types of parameters, the simulations presented in this chapter are carried out in two stages: preliminary analysis and parametric investigation.

It should be noted that all simulations in this research are carried out on a personal laptop computer with the specifications given in Table 4.1. When presenting the results in this chapter, the computational time is used as a performance parameter: therefore, it is important to note the computer specifications associated with the reported computational times in the simulations.

**Table 4.1:** Specifications of the computer used in the identical twin numerical experiments.

CPU	Pentium(R) Dual-Core CPU T4200
Speed (GHz)	2.00
Memory (GB)	2
Operating System	Ubuntu 10.04 LTS - the Lucid Lynx

## 4.2 Preliminary Analysis

The preliminary analysis is carried out to find the optimal parameters that are used in the numerical operations of the inverse modelling algorithm. Table 4.2 summarizes all simulations carried out in this section. The preliminary analysis cases and investigated parameters are as follows:

- PA 1: Perturbation size in obtaining the sensitivity matrix
- PA 2: Interval size used in determining the step size for the conjugate gradient algorithm,  $\alpha$
- PA 3: Discretization parameters: element type, element size and domain size

- PA 4: Initial potential values along the steel/concrete interface
- PA 5: Convergence criterion

As discussed in Chapter 3, the sensitivity matrix used in the developed inverse solution algorithm is obtained directly by successively applying a small perturbation on each node on the steel/concrete interface and solving the forward problem to calculate the changes in potentials for each of the nodes on the concrete surface. The size of the perturbation is a critical element in optimizing the performance of the inverse solution. When large perturbations are used, the sensitivity matrix may not produce the required results; however, very small perturbations may cause convergence issues. Therefore, the size of the perturbation is optimised in the preliminary analysis.

Since the step size,  $\alpha$ , directly affects the mechanics of the algorithm, it is also investigated in the preliminary analysis. The step size in the conjugate gradient method is calculated through a local minimisation of the cost function, which in this research, is implemented using quadratic interpolation. In the quadratic approximation, three values of  $\alpha$  are used to find three different points on the cost function and a quadratic polynomial is fit to these points. The minimum is directly calculated from the polynomial and the value of  $\alpha$  corresponding to the minimum cost function is used for the next iteration step. In the investigation, the interval between the three points is varied to determine the optimal spacing.

The element type and size are factors of the discretization scheme (e.g. the number of nodes and elements in a domain as well as the interpolation within the finite element analysis), therefore, they have a considerable effect on both the shape and convergence of the inverse solution. The Dolfin package allows automatic discretization or importation of a discretized domain (from a third-party mesh generator); in this study, the automatic discretization option is used. To ensure that there is no bias

**Table 4.2:** Preliminary analysis test grid.

	PA 1	PA 2	PA 3	PA 3	PA 3	PA 4	PA 5
Perturbation (V)	9 test cases <sup>a</sup>	$10^{-5}$	$10^{-5}$	$10^{-5}$	$10^{-5}$	$10^{-5}$	$10^{-5}$
Step size, $\alpha$	0.1	5 test cases <sup>b</sup>	1	1	1	1	1
Element Type	crossed	crossed	4 test cases <sup>c</sup>	crossed	crossed	crossed	crossed
Element Size (mm)	10	10	10	5, 10, 16, 20	10	10	10
Width (mm)	1200	1200	1200	1200	800, 1200	1200	1200
Cover (mm)	80	80	80	80	40, 80, 160	80	80
Resistivity ( $\Omega$ -m)	150	150	150	150	150, 1500	150, 1500	150
Initial Value	IP 1	IP 1	IP 1	IP 1	IP 1	IP 1 to IP 7	IP 4
Tolerance	$10^{-8}$	$10^{-8}$	$10^{-8}$	$10^{-8}$	$10^{-8}$	$10^{-8}$	5 test cases <sup>d</sup>

<sup>a</sup>1,  $10^{-1}$ ,  $10^{-2}$ ,  $10^{-3}$ ,  $10^{-4}$ ,  $10^{-5}$ ,  $10^{-6}$ ,  $10^{-7}$ ,  $10^{-8}$

<sup>b</sup>10, 1, 0.1, 0.01, 0.001

<sup>c</sup>square elements with left facing diagonals (left), right facing diagonals (right), alternating left and right facing diagonals (left/right) crossed diagonals (crossed)

<sup>d</sup> $10^{-8}$ ,  $10^{-9}$ ,  $10^{-10}$ ,  $10^{-11}$ ,  $10^{-12}$

introduced into the solution due to an unstructured mesh, triangularization is carried out within the square units covering the rectangular domain of analysis. The Dolfin package has the option of creating triangular elements in each square unit using left or right facing diagonals, alternating left and right diagonals, or crossed diagonals. For all cases except for the crossed diagonal option, this operation divides each square unit into two triangular elements with nodes on all four corners of the square. In the case of the crossed diagonals, the square is divided into four elements with an extra node in the middle where the diagonals cross (Figure 4.1). Although all configurations result in triangular elements, the elements are referred to as "square elements with diagonals" for convenience. The preliminary analysis was carried out to determine which configuration of diagonals produced the optimal results. In addition, the effect of the domain size on the simulation is also investigated as this parameter is closely linked with concrete resistivity [1].

Both the initial potential values along the steel/concrete interface and the convergence criterion affect the success and the rate of convergence of the inverse solution algorithm. Although the developed algorithm is robust enough to converge from an arbitrary initial condition imposed on the steel/concrete interface, a more appropriate starting condition can be found that results in a smoother final solution and a faster convergence rate. To investigate the effect of initial potential values along the steel/concrete interface, the following seven cases were investigated in the preliminary analysis:

- IP 1: Initial potential distribution set to zero
- IP 2: Initial potential distribution set to the standard anodic equilibrium potential (-0.780 V)
- IP 3: Initial potential distribution set to the standard cathodic equilibrium

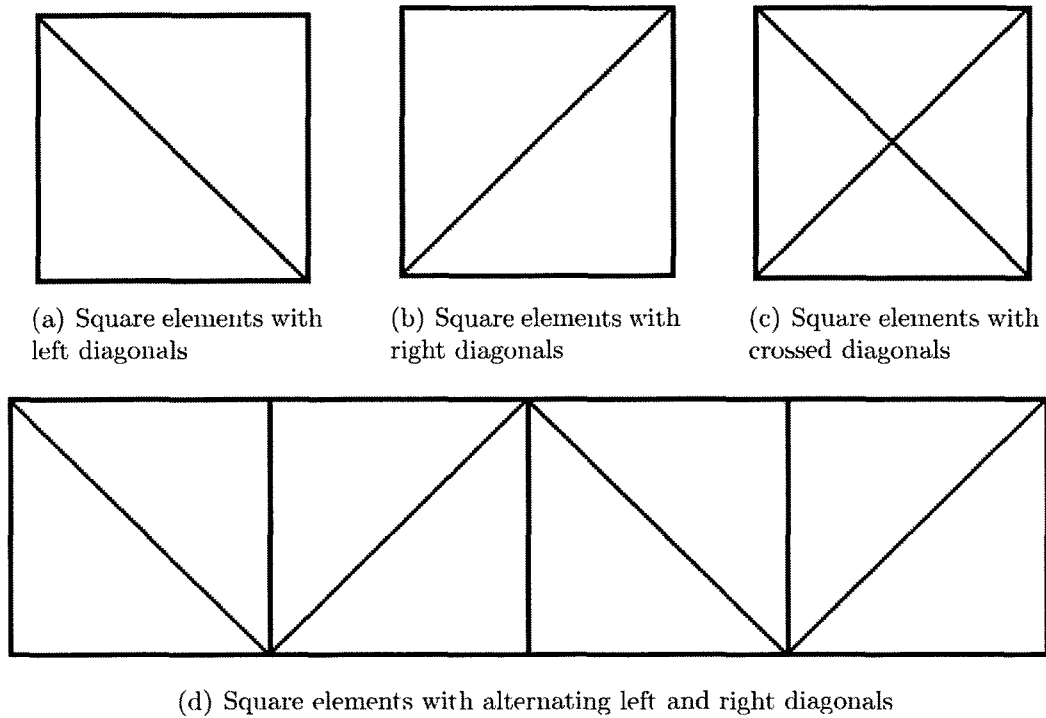


**Figure 4.1:** Discretization schemes used in the preliminary analysis

potential (0.160 V)

- IP 4: Initial potential distribution set to the observed potentials on the surface of concrete
- IP 5: Initial potential distribution set to the idealised function with  $\kappa$  set to 0.1
- IP 6: Initial potential distribution set to the idealised function with  $\kappa$  set to 0.25
- IP 7: Initial potential distribution set to the idealised function with  $\kappa$  set to 0.5

Figure 4.2 illustrates the initial potential distributions set using the measured potentials on the surface of concrete. Three different values of the idealisation coefficient,  $\kappa$ , for use in the idealised function as discussed in chapter 3 are used resulting

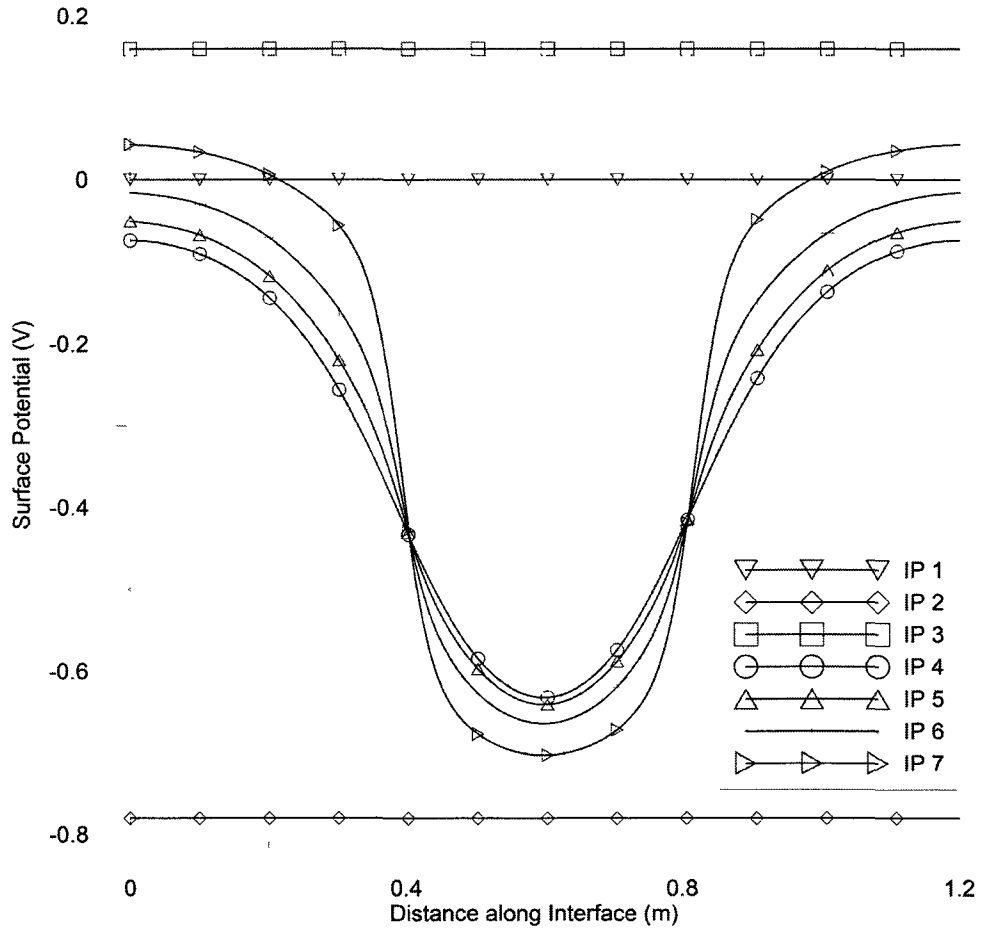


**Figure 4.2:** Possible selections for the initial potential distribution along the steel/concrete interface.

in the total of seven test cases.

In the convergence criterion analysis, the tolerance is varied to determine if a decreased tolerance would result in a more accurate solution without a prohibitive computational expense.

### 4.3 Parametric Study

While the preliminary analysis primarily investigates the effect of numerical or algorithm-specific parameters on the performance of the developed inverse model,

it is also important to study the effects of the physical parameters that define the corroding system. These parameters of interest, as summarized in Table 4.3, are:

- Location of the anode
- A/C ratio
- Concrete resistivity
- Concrete cover thickness
- Frequency of measurement points on concrete surface

**Table 4.3:** Parametric study test grid.

Anode location	end, middle
A/C ratio	0.11, 0.25, 0.50
Concrete resistivity ( $\Omega\text{-m}$ )	150, 1500
Concrete cover thickness (mm)	80, 160
Number of observed nodes	120, 60, 40, 30, 24

As discussed in Chapter 1, half-cell potential measurements on the surface of the concrete are a function of the type of corrosion that is occurring on the steel/concrete interface. In the case of uniform corrosion, in which the A/C ratio is near unity, the potential readings at the surface of the concrete are typically close to the potential at the steel/concrete interface [9]; however, in the case of non-uniform corrosion, local or pitting corrosion with a small A/C ratio, the measured potentials at the surface of concrete can be substantially different from those of the steel/concrete interface. Accurate detection of localized corrosion, in which the A/C ratio can be small, may not be feasible with half-cell potential measurement method unless supplementary

information is provided. As a result, the A/C ratio is varied to determine if the algorithm has trouble detecting small anodes that appear in pitting corrosion. A single localised anode can appear at the end of the domain (i.e., end of the reinforcement) or in the middle of the domain; therefore both cases were investigated to see if the location had any effect on the performance of the algorithm.

In addition, as pointed out by Pour-Ghaz et al. [1], an increase in the resistivity of the concrete or the cover thickness will generally cause a weaker correlation between the potentials on the steel/concrete interface and on the concrete surface. This may make it harder for the inverse modeling algorithm to converge to a solution. To investigate these effects, concrete resistivity and concrete cover thickness are chosen as additional parameters to investigate in the parametric study.

The discretization scheme has a node at every 10 mm along the surface of the concrete. While this provides good accuracy for the model, unless a specialised method of measurement is developed, it is impractical to expect measurements to be made at such small intervals. The number of observed nodes that were used in the algorithm was therefore varied to determine the model's response to data that was measured at larger intervals.

It is important to note that the effect of the removal of observed nodes was investigated with a single set of physical parameters. The parameters discussed above were all comprehensively investigated, and a case was selected representing both the worse case scenario from the point of computational difficulty and a safe assumption minimising some of the side effects that were discovered over the course of the comprehensive analysis.

## 4.4 Results and Discussion: Preliminary Analysis

### 4.4.1 PA 1: Perturbation Analysis

Perturbation sizes were tested in  $1 \times 10^{-1}$  increments from 1 V to  $1 \times 10^{-8}$  V. Only three test cases reached convergence:  $1 \times 10^{-5}$ ,  $1 \times 10^{-6}$  and  $1 \times 10^{-7}$ .

As discussed in Chapter 3, the sensitivity matrix represents a tangent linear approximation of the sensitivity of the surface potential to changes in the interface potential. If the problem were linear, these sensitivities could be used to directly calculate the solution in a single iteration. However, since the problem is non-linear, the perturbation must be small enough that a linear approximation of the behaviour of the system can accurately represent the actual behaviour of the system. This explains why the system did not converge when the perturbation was increased beyond  $1 \times 10^{-5}$ ; the perturbations were too large and the linear approximation no longer held true.

The non-convergence of the system for a perturbation smaller than  $1 \times 10^{-7}$  is harder to explain. This is not an issue with the mathematical processes, the non-convergence must instead be the result of internal round off errors within the forward solver. These small errors introduce enough inaccuracy into the sensitivity matrix that the algorithm no longer has enough information to reach convergence.

### 4.4.2 PA 2: Interpolation of $\alpha$

The interval size determines the spacing of the three values of  $\alpha$  from which the quadratic approximation of the behaviour of the cost function is calculated. Interval sizes of 10, 1, 0.1, 0.01 and 0.001 were chosen for this analysis. Interval sizes of 1 and 10 performed the best both in time of convergence and in number of iterations

**Table 4.4:** Inverse convergence rates depending on the  $\alpha$  interval size used in the quadratic interpolation algorithm.

Interval size	Time (s)	Iterations	Initial step	Final step	Max step	Min step
10	13.5	77	-62609.1	-82581.7	-33273.8	-120720
1	13.84	79	-62609.9	-47267.6	-12888.5	-120769
0.1	54.68	312	-62497.4	-2187.42	1578110	-218628
0.01	144.32	820	-70040.8	-2045.55	813486	-576387
0.001	889.32	5087	4808.57	-155.933	991199	-152058

to convergence (Table 4.4).

As can be seen from examining the maximum and minimum step sizes in table 4.4, once the interval size increases beyond 0.1, the approximation of  $\alpha$  produced results that were consistently negative. Since  $\alpha$  determines how far the algorithm moves along the search direction vector, and since the algorithm is stepping towards a minimum, negative step sizes indicate that the algorithm is consistently moving in the right direction. For smaller interval sizes, the algorithm gets stuck in false minima and occasionally needs to produce a positive value for  $\alpha$  (a step backwards) to get out of these false minima. This process is demonstrated in figure 4.3. The values of  $\alpha$  calculated using the three smallest interval sizes closely follow each other for the first few iterations until step sizes calculated using an interval of 0.1 slowly begins to diverge from the others. Eventually, the algorithms using that interval size needs to produce a large positive value for  $\alpha$  to get back on track. The values of  $\alpha$  that were produced using an interval size of 0.01 diverge immediately and require a much larger number of positive steps. The plot of the smallest interval size was not included in the comparison for clarity. As can be seen from table 4.4, the interval size of 0.001 performed even more poorly requiring over 6 times the number of iterations to reach convergence compared to the 0.01 size for the interval.

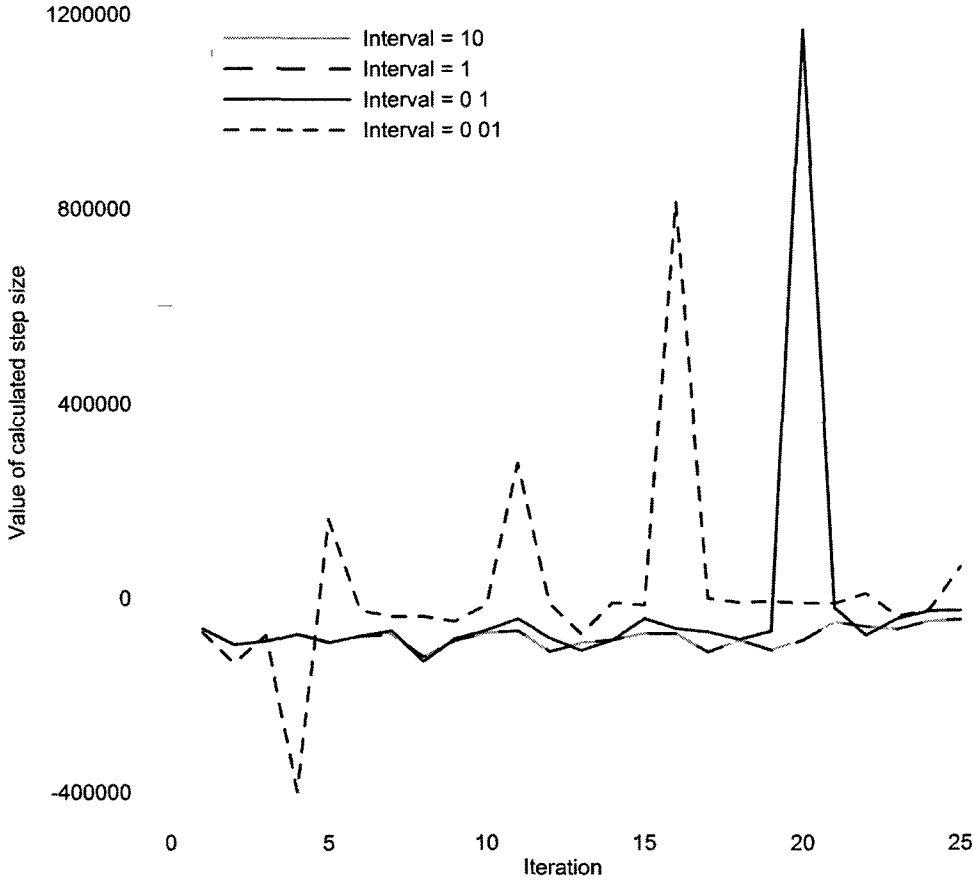


**Figure 4.3:** Comparison of four proposed  $\alpha$  interval sizes over 25 iterations showing the divergence of the calculated value for  $\alpha$  when the two smallest intervals are used.

An interval size of 1 was chosen since it is the smallest interval above the threshold where positive value were no longer produced for  $\alpha$ . The smaller interval size is desirable to reduce the possibility of lost information due to the interpolation process.

### 4.4.3 PA 3: Element Type

As illustrated in Figures 4.4 and 4.4, different element types produce similar inverse solutions with small local differences near the transition zones where the curvature of the solution changes drastically. The smoothest solution is obtained when elements with crossed diagonals are used. The other three element type options introduce

a bias in the solution near the zones where curvature changes. Although elements with crossed diagonals increase the computational expense since there are twice the number of elements and 20% more nodes than in any of the other three cases, they are the optimal choice among the tested element types because of the elimination of this bias. Local abnormalities, especially in zones where the curvature changes significantly (e.g. near the interfaces between anodes and cathodes) have the potential to create convergence issues for the inverse solution; therefore, in the identical twin numerical experiments in this thesis, elements with crossed diagonals are used.

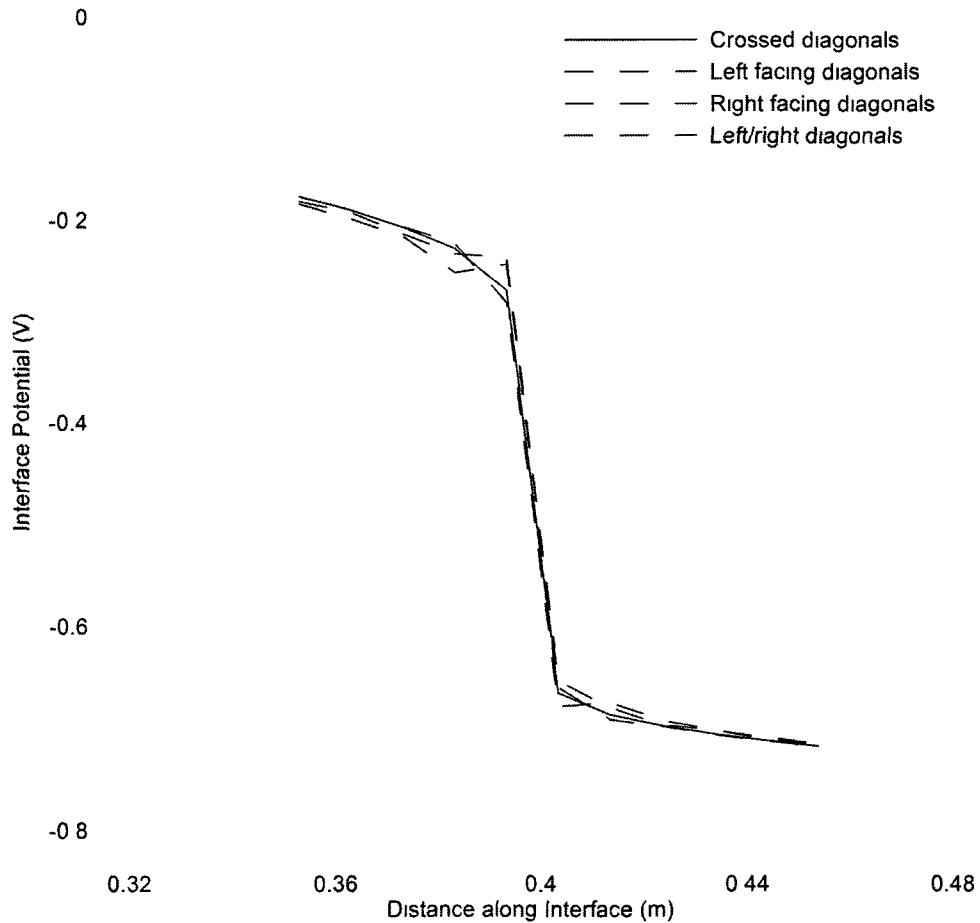


**Figure 4.4:** Close up comparison of the forward solution using different diagonals for the discretisation scheme at the left transition zone between anodic and cathodic potentials. Middle location for the anode, A/C ratio = 0.5.  $\rho = 150 \Omega\text{-m}$ .

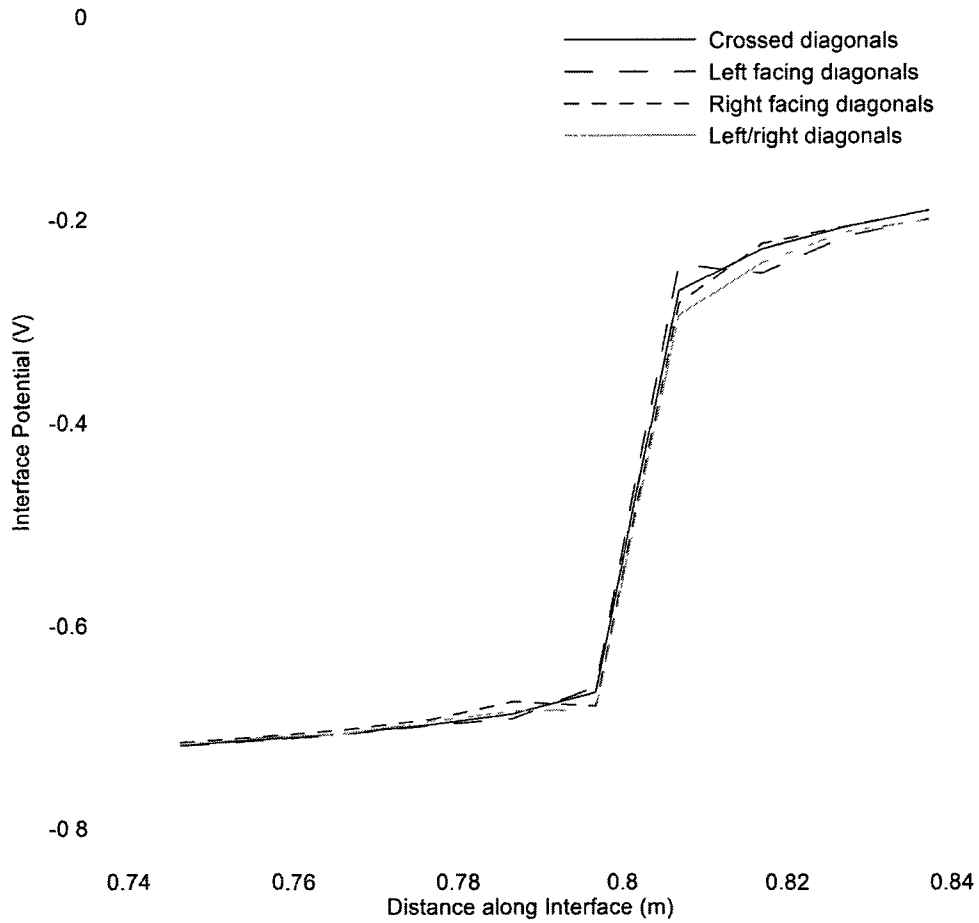


**Figure 4.5:** Close up comparison of the forward solution using different diagonals for the discretisation scheme at the right transition zone between anodic and cathodic potentials. Middle location for the anode, A/C ratio = 0.5,  $\rho = 150 \Omega\text{-m}$ .

#### 4.4.4 PA 3: Element Size

The element size analysis was carried on a 1200 mm (length)  $\times$  80 mm (cover) domain. The domain was divided into square units that were discretized with crossed diagonals. Four different sizes for the square units were chosen for comparison purposes: 5 mm, 10 mm, 16 mm, and 20 mm. The results were compared for accuracy and for rate of convergence.

The forward problem did not converge to a sensible answer when 5 mm square

units were used as illustrated in Figure 4.6. This is a problem that was also encountered by other researchers [72]. When very small elements are used, the non-linear solution of the forward problem experiences convergence issues; therefore, the forward solution shows oscillations and noise. Because of the issues associated with the forward solution, 5 mm square units were not used in the remaining analysis cases of this investigation.

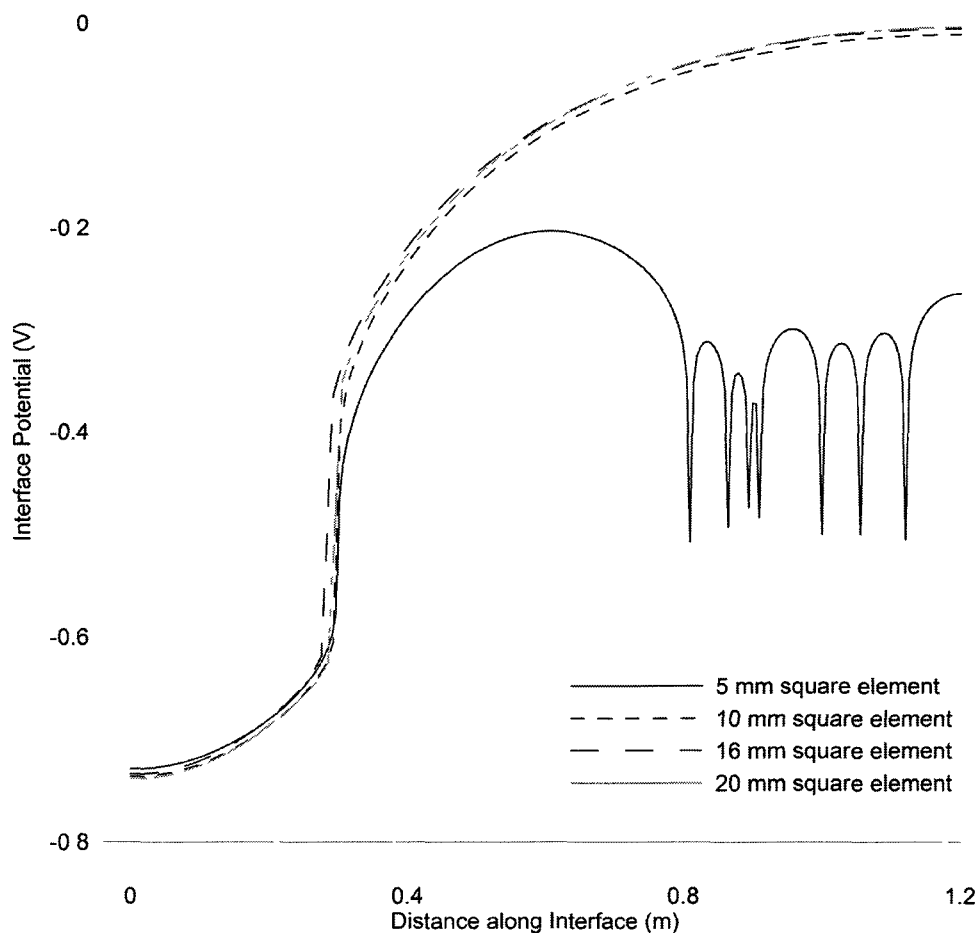


**Figure 4.6:** Forward solution of the potential distribution along the steel/concrete interface for different element sizes.

In a comparison among the remaining three element sizes, the smallest possible element size is desired so that the resolution of the final solution will be as high as

possible. Once the performance of the algorithm is fully understood, the element size can be increased to mimic real life spacing between measurements. Since the 10 mm element is the smallest element that converged it represents the optimal choice for use in the remaining simulations, even though the times of convergence were much higher than when using the larger elements (Table 4.5).

**Table 4.5:** Convergence rates of the inverse solution depending on element size.

Element Size	Computational Time (s)	Number of Iterations
10 mm	16.06	91
16 mm	5.55	81
20 mm	3.53	78

It should be noted that the number of iterations to obtain a converged inverse solution for all three element sizes is quite similar while the computational times show significant variability. It is obvious that each iteration would take more time as the element size is decreased since the matrices involved will now become larger. However this cannot fully explain why there is such a small difference in the number of iterations to convergence. The main reason for this lies within the determination of the sensitivity matrix, which takes a considerable amount of time since they involve multiple forward solutions also involving large matrices.

#### 4.4.5 PA 3: Domain Size

Changing the resistivity of the concrete does not affect the inverse solution, but it does affect the forward solution resulting in different sets of input data. A system with a high resistivity results in a potential distribution on the interface that contains areas with a high rate of change and both a smaller minimum value and larger maximum value. The difference between the surface potential distribution and the

interface potential distribution also increases as the resistivity increases. Since the total resistance is a function of both the resistivity of the material and the distance the current must flow through that material, the domain size, and especially the cover thickness, will have a large effect on the difference between the observed surface potential and the final calculated value for the potential on the interface. The effects of the domain size were therefore investigated at two different resistivities, 150  $\Omega\text{-m}$  and 1500  $\Omega\text{-m}$  using a domain discretized in 10 mm square units based on the previous analyses. Three different cover thicknesses, 40 mm, 80 mm and 160 mm and two different domain lengths, 800 mm and 1200 mm, were selected for the simulations in this section.

The inverse solution algorithm did not converge for a cover thickness of 40 mm in three out of the four cases (Table 4.6), therefore that cover size was not used further in this analysis. Because there are so few nodes between the interface and the concrete surface, small oscillations that occur naturally at the interface as a result of the inverse solution process are almost directly reflected on the concrete surface. This results in a phenomenon where the interface oscillations are magnified by the surface oscillations, resulting in a feedback loop, and leading to non-convergence.

Test cases that were run with a cover thickness of 160 mm consistently took longer to converge than those with a cover thickness of 80 mm (Table 4.6). This result was expected because of the relation between total resistance and cover thickness described above and confirmed the assumption that the steeper the true value of the potential distribution on the interface, the harder it is for the algorithm to reach convergence. The times of convergence with a resistivity of 1500  $\Omega\text{-m}$  were less than with a resistivity of 150  $\Omega\text{-m}$ . This result was also expected since the resistivity was increased by a factor of 10 while the cover thickness was only increased by a factor

**Table 4.6:** Inverse convergence rates depending on domain dimensions with two different resistivities.

Resistivity of 150 $\Omega$ -m		
Domain size	Computational Time (s)	Number of Iterations
800 mm $\times$ 80 mm	9.17	77
800 mm $\times$ 160 mm	52.51	211
1200 mm $\times$ 80 mm	16.05	91
1200 mm $\times$ 160 mm	31.93	85

Resistivity of 1500 $\Omega$ -m		
Domain size	Computational Time (s)	Number of Iterations
800 mm $\times$ 80 mm	11.54	99
800 mm $\times$ 160 mm	43.77	178
1200 mm $\times$ 80 mm	17.39	100
1200 mm $\times$ 160 mm	49.02	134

of 2. This means that the higher resistivity has a much greater effect than the larger cover thickness, lessening the difference in the time of convergence between cases with different cover thicknesses and a high resistivity.

Since the cases with a cover thickness of 160 mm took longer to converge, and since an 80 mm cover is a more realistic assumption, as well as an assumption that will be more likely to lead to corrosion, 80 mm was determined to be the optimal size for the cover.

Since there was very little difference in the time of convergence between the 800 mm and the 1200 mm length for the domain, indicating that the domain length had little effect on the performance of the algorithm, and since in one case the time of convergence for the 800 mm length was actually longer than for the 1200 mm length, the 1200 mm length was determined to be the optimal value, as the more realistic

assumption with little to no computational penalty.

#### 4.4.6 PA 4: Initial Potentials along Steel/Concrete Interface

Even though the algorithm is robust enough to converge from a initial potential distribution of zero, it was discovered that the initial potential distribution does affect the shape of the final solution. While the algorithm has no trouble with convergence in the middle of the domain, the shape of the ends depends heavily on the initial value (Figure 4.7). The initial potential distribution that results in the smoothest graph would therefore be the optimum initial distribution. By examining the detail plots at both ends of the graphs and excluding the constant initial conditions which all result in extreme oscillations at the ends (Figures 4.8 and 4.9), it can be clearly seen that both the observed data and the idealised function with a coefficient of 0.1 seem to result in the smoothest curves at the end.

The optimal choice is therefore narrowed down to the observed data and the idealised solution with  $\kappa$  equal to 0.1. If the decision is based on the time of convergence, evaluated by either the number of iterations or the total time, then the observed data would be the clear choice (Table 4.7). Since a smaller value for the idealisation coefficient means that the idealised function is approaching the observed data, this strongly supports the choice of the observed data. The observed data is also a much simpler choice from the computational point of view, and less likely to result in errors because of the process of construction of the idealised solution; therefore, the observed data was determined to be the optimum initial potential value and was used for all further studies.

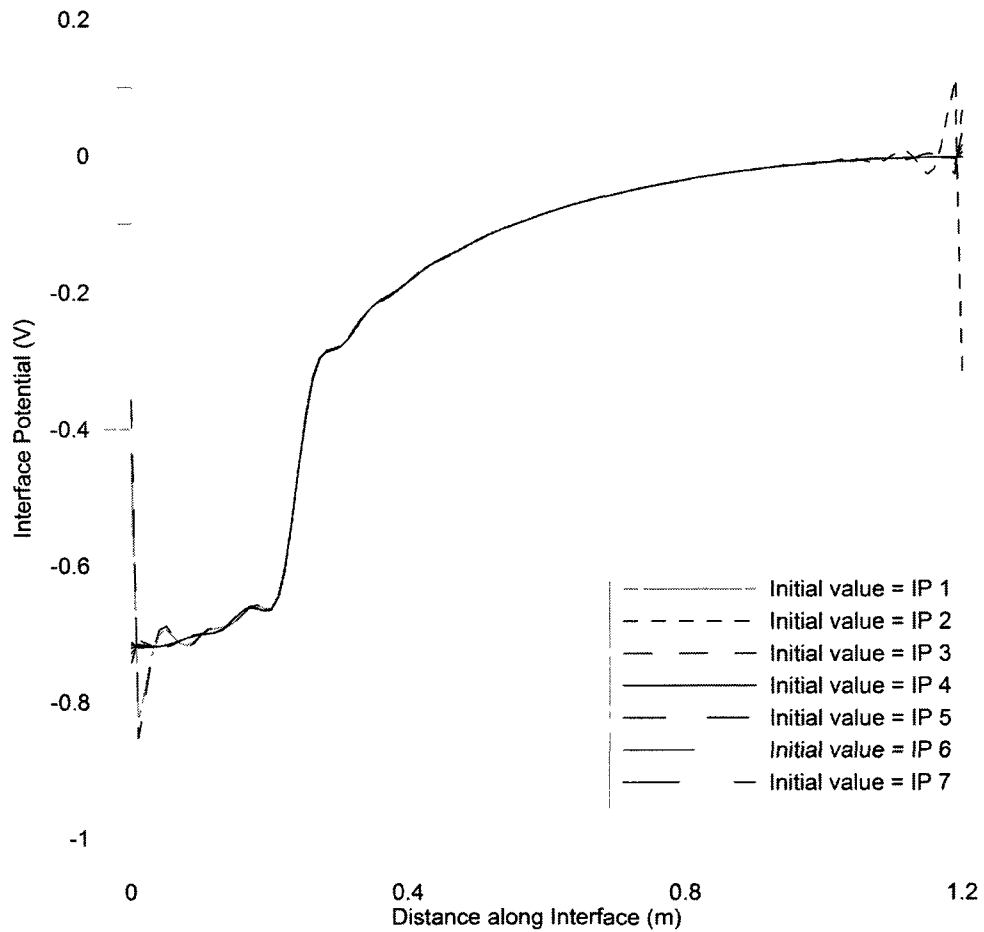


**Figure 4.7:** Inverse solution for the interface potential depending on the initial potential distribution.

#### 4.4.7 PA 5: Convergence Criteria Analysis

The test cases were run with tolerances of  $10^{-9}$ ,  $10^{-10}$ ,  $10^{-11}$  and  $10^{-12}$ . The maximum number of iterations was raised from 5000 to 25000 to try and ensure convergence, however, none of the test cases below  $10^{-8}$  converged. Therefore a tolerance of  $10^{-8}$  was used for the parametric study.

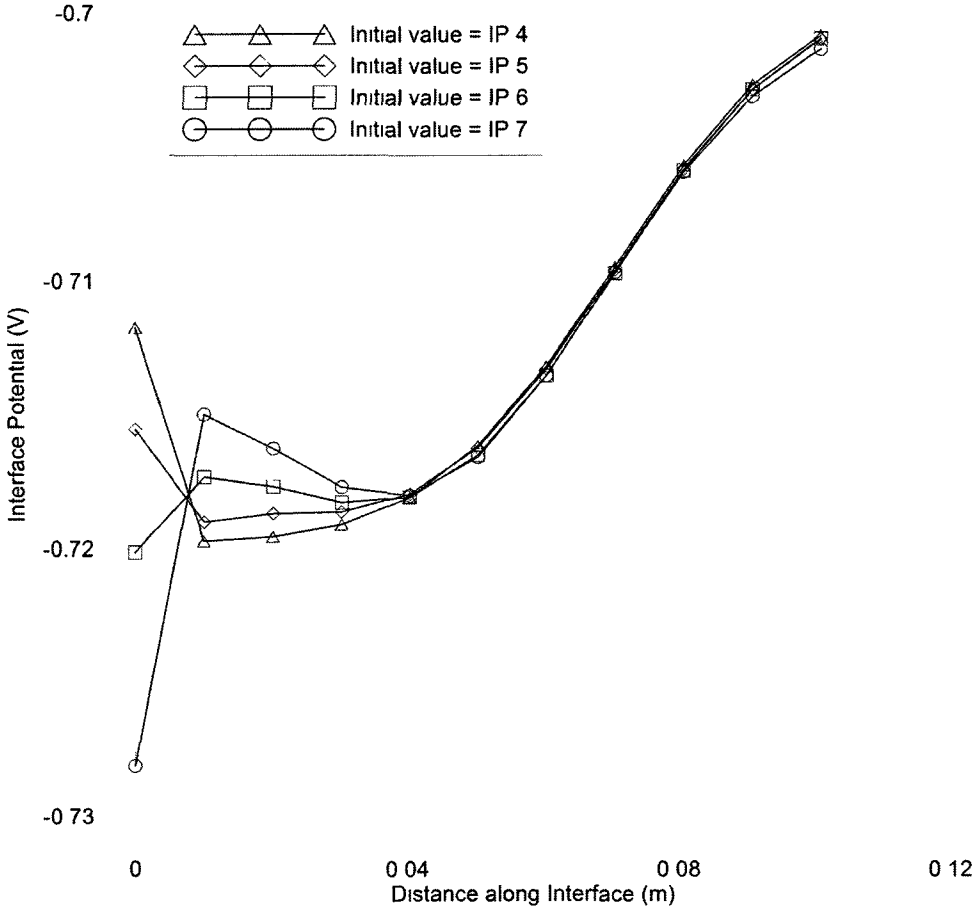
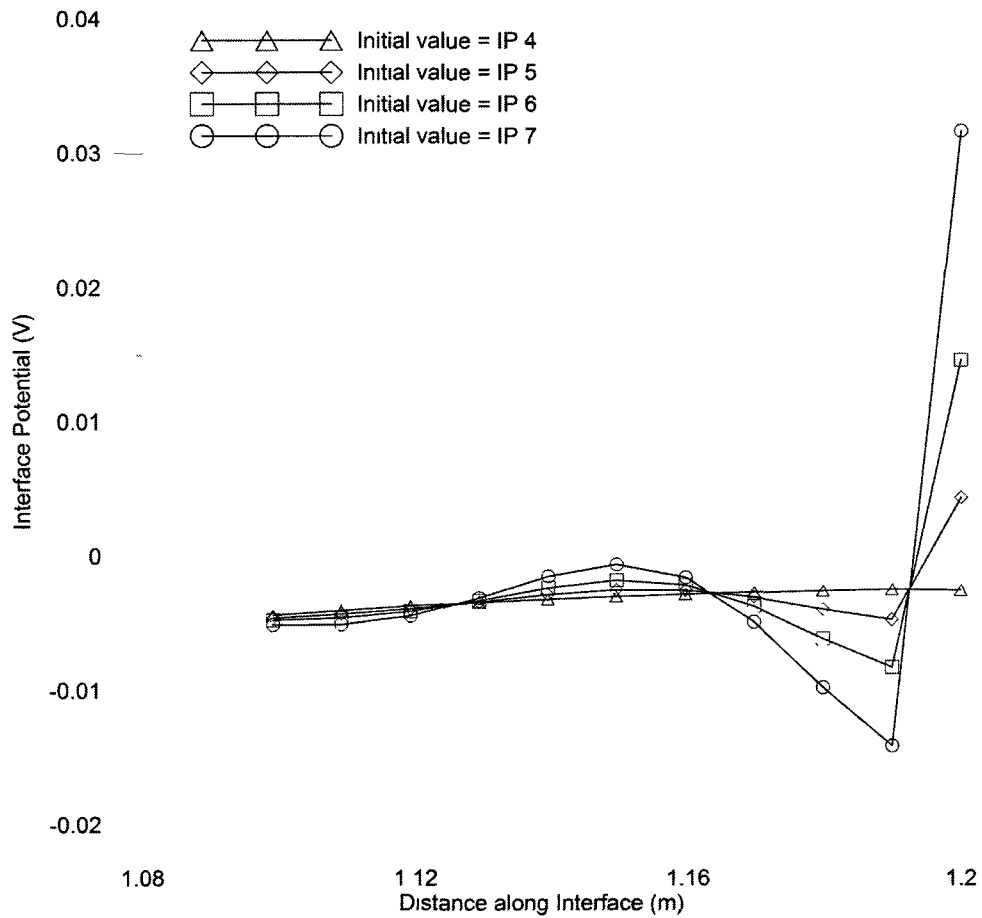


Figure 4.8: Detail of the left side of the plot of the inverse solution for the interface potential depending on the initial potential distribution.

### 4.4.8 Summary of the Preliminary Analysis

Based on the preliminary analysis results, the following optimal conditions have been identified for the identical twin numerical experiments in the parametric study.

- Square elements with crossed diagonals are the optimum, resulting in four triangular elements with a node at each corner of the square and a node in the center where the diagonals intersect.
- A perturbation of  $10^{-5}$  V is optimum.
- A step size of value 1 was selected as the optimum increment for  $\alpha$  to determine



**Figure 4.9:** Detail of the right side of the plot of the inverse solution for the interface potential depending on the initial potential distribution.

the points to use in the quadratic interpolation algorithm for the finding of the value of  $\alpha$  that minimises the cost function.

- An element size of 10 mm  $\times$  10 mm for the side length of the square was determined to be the optimal size.
- A domain size of 1200 mm length by 80 mm height.
- The use of the observed data as the initial value for the algorithm was determined to be optimal.
- A tolerance of  $10^{-8}$  was determined to be the optimum since none of the more

**Table 4.7:** Inverse convergence rates depending on the initial potential distribution.

Initial Value	$\rho = 150$		$\rho = 1500$	
	Time (s)	Iterations	Time (s)	Iterations
IP 1: Zero Potential	15.88	91	17.77	100
IP 2: Anodic Potential	15.04	86	19.74	114
IP 3: Cathodic Potential	15.54	89	18.02	103
IP 4: Observed Potentials	9.77	56	13.72	77
IP 5: Ideal with $\kappa = 0.1$	13.20	77	17.42	100
IP 6: Ideal with $\kappa = 0.25$	11.17	65	17.52	98
IP 7: Ideal with $\kappa = 0.5$	10.75	62	14.05	79

stringent criteria resulted in convergence.

## 4.5 Results and Discussion: Parametric study

A comprehensive set of test cases was run to investigate the performance of the inverse model under different operating conditions. The behaviour of the system is first discussed in depth and samples of the results are referenced to illustrate points of discussion. The complete results are then presented in graphical form at end of the chapter. Since all the parameters are studied simultaneously, all of the results can be used to represent the effect of each parameter, therefore, instead of showing the same results more than once, the majority of the results are presented at the end of the chapter.

### 4.5.1 Effect of Residual Equations

Both the Fletcher-Reeves equation (Equation 3.19) and the Polak-Ribiere equation (Equation 3.20) for the calculation of the  $\gamma$  coefficient of the conjugate gradient

method were used in this investigation. None of the test cases using the Polak-Ribiere equation converged. Therefore it can be concluded that the stability and robustness of the Fletcher-Reeve equation is required for this algorithm.

### 4.5.2 Effect of Anode Location

The anodic location was varied over two cases:

- Case I: Anode at one end of the domain. This results in a single cathode as well, which begins as soon as the anodic region ends and continues to the end of the reinforcement.
- Case II: Anode in the middle of the domain. This results in two smaller cathodes, one to either side of the anode. Since the A/C ratio is maintained, the cathodes in this case are half the length of the cathodes in Case I.

In all cases, the algorithm performed well and converged to a solution with a close congruence with the forward results. Figures 4.14 and 4.15 show the final potential distribution generated by the inverse model under Case I with different resistivities. Figures 4.20 and 4.21 show the results of the inverse model under Case II and with both resistivities. From examination of these figures it can be seen that the model converged to a reasonable approximation of the forward solution. It can also be seen that the location of the anode does not affect the quality of the solution. The only effect the anode location has is on the times of convergence.

If the anode is located in the middle of the interface (Case II), the algorithm has more trouble achieving convergence than if the anode is located at the end of the interface (Case I). In two thirds of the cases, the time of convergence was larger for the middle location than for the end location. In one case, the solution for a middle location never converged. For the test cases where the middle location had a shorter

time of convergence than the end location, there was much less of a time difference than for the cases where the opposite held true (Table 4.8).

These results were unexpected since, in general, end conditions that have a high rate of change or a steep slope tend to cause trouble for convergence. However, since the A/C ratio is assumed to always be less than or equal to one, the regions with the most change, and hence the regions where the algorithm will have the most trouble, are the anodic regions. In the case of the end location, the anode effects much less of the total potential distribution since all the effect is confined on one end of the interface. In the case of the middle location, the effect of the anode is maximised. Alternatively, Case I has only a single anode and cathode, and therefore only one area with a steep rate of change, Case II has two cathodes and therefore two transition zones with a high rate of change. This explains why the algorithm has more trouble with the middle location.

### 4.5.3 Effect of A/C Ratio

The A/C ratio was varied over three values, 0.11, 0.25 and 0.5. The value of 0.11 was chosen for convenience since the number of anodes is divisible by three. The inverse model converged to solutions that are similar in shape to the solutions obtained from the forward model. Only one solution did not converge below the specified tolerance of  $1 \times 10^{-8}$ , the case with the smallest A/C ratio, lowest resistivity and smallest cover thickness. The final solution produced by the case that did not converge had a final cost function of  $1.138 \times 10^{-8}$  after 5000 iterations, which is almost at the convergence criteria. It also produced a reasonable solution for the interface potential distribution (Figure 4.10).

In the remaining test cases, the inverse solution converged to values that were

**Table 4.8:** Inverse convergence rates depending on anode location for a given A/C ratio, resistivity and cover thicknesses.

Resistivity ( $\Omega$ -m)	Cover (mm)	End		Middle	
		Time (s)	Iterations	Time (s)	Iterations
A/C Ratio = 0.11					
150	80	8.35	48	857.03	5002
	160	18.89	52	16.7	46
1500	80	11.91	69	33.32	194
	160	33.15	91	21.81	60
A/C Ratio = 0.25					
150	80	9.71	56	10.29	69
	160	19.42	53	78.05	214
1500	80	13.3	77	12.88	75
	160	26.77	74	53.24	174
A/C ratio = 0.5					
150	80	9.6	56	10.47	61
	160	20.02	55	27.75	75
1500	80	13.05	76	13.78	80
	160	36.47	100	31.32	86

good approximations of the forward solution. Figures 4.12 and 4.18 show a sample of the results with a low A/C ratio compared figures 4.16 and 4.22 which show a sample of the results for a large A/C ratio. All figures show results at a resistivity of 150  $\Omega$ -m. It can be seen in these figures that the convergence of the system is not affected by the A/C ratio. However, it can also be seen that the solution with the smallest A/C ratio generates oscillations of higher amplitude in the anodic region than the the solution with the largest A/C ratio. The same effects are noticeable in

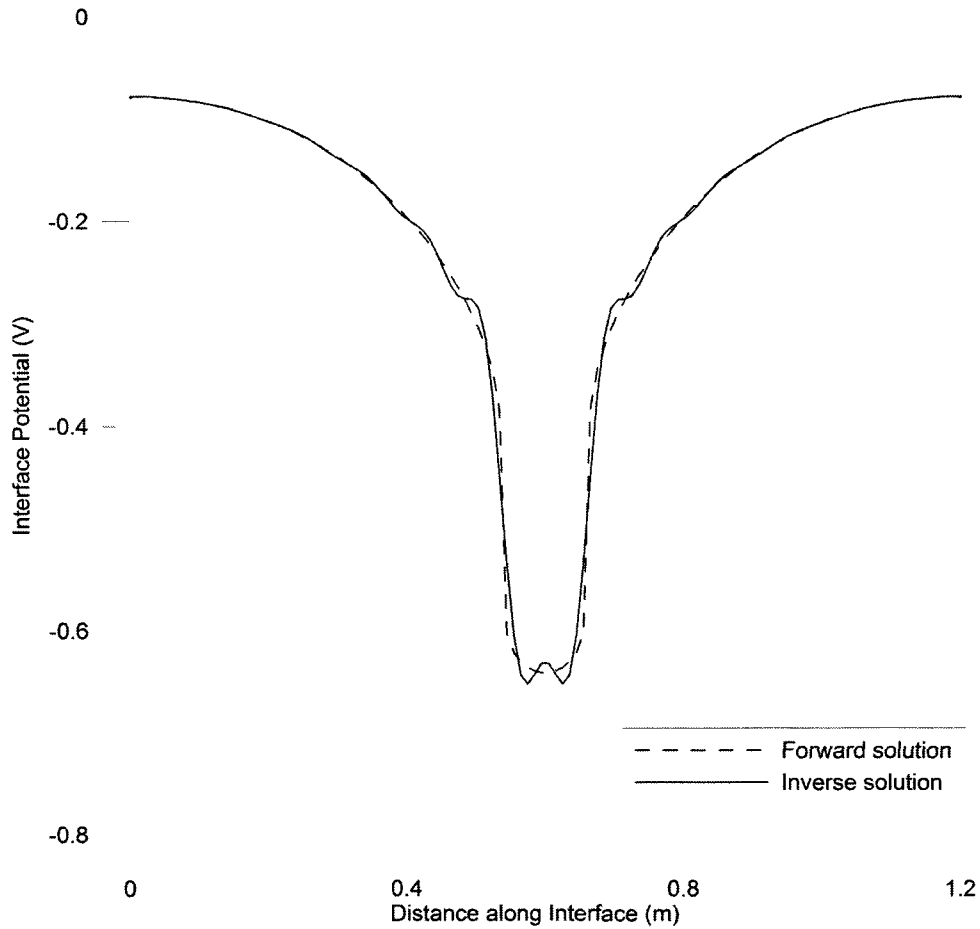


**Figure 4.10:** Inverse solution that did not converge below tolerance of  $10^{-8}$ . Middle anodic location, A/C ratio = 0.11,  $\rho = 150 \Omega\text{-m}$ , cover thickness = 80 mm.

the cases with higher resistivity. This is easily explained by noting that the strongest oscillations occur in the areas of the potential distribution with the highest rates of change. Since the smallest A/C ratio creates a narrow trough, the rate of change in the anodic region is high, and therefore the oscillations also have higher amplitude. A comparison of all three cases for the A/C ratio with a resistivity of  $1500 \Omega\text{-m}$  can be seen by examining figures 4.13, 4.15 and 4.17.

The A/C ratio has two effects on the solution. In general it tends to cause the time of convergence to increase as the A/C ratio increases. However if the A/C ratio is too small, then the solution does not converge, or has difficulty converging (Table

4.8).

These results are consistent with the results obtained in the previous section. As the A/C ratio increases, the anodic region and the transition zone has more affect on the total solution making convergence harder to achieve and increasing the time of convergence.

The fact that decreasing the A/C ratio can cause non-convergence is also easily explained. Since the estimate of the final solution oscillates with each iteration, the algorithm will have trouble finding a solution that matches such a small and sharp potential difference. When the A/C ratio is larger, the potential difference caused by the anode is more spread out and the change is more gradual, allowing for easier convergence. This can also be explained by the same phenomenon as discussed in the preliminary element size study. Since the case that did not converge had the smallest cover thickness and lowest resistivity, the correlation between the interface and surface potentials was too strong, causing feedback and non-convergence. It should be noted that the cause of non-convergence was a combination of factors, and not solely the result of the ratio.

#### **4.5.4 Effect of Resistivity and Concrete Cover Thickness**

The resistivity was varied over two values: 150  $\Omega$ -m and 1500  $\Omega$ -m and the cover thickness was varied over two values: 80 mm and 160 mm. These two factors did not affect convergence, except in the case noted in the previous section. Figures 4.18 and 4.19 show a sample of the results at both resistivities with a small A/C ratio, figures 4.16 and 4.23 show the same with a large A/C ratio. These results clearly show the effect the cover thickness has on the forward solution. As previously demonstrated, as the cover thickness increases, the correlation between the surface potentials and the interface potentials decreases. These results also show the effect of resistivity, as the

resistivity increases, the shape of the potential distribution becomes more extreme. This effect was also previously discussed. There was very little difference between the congruence of the inverse solution to the forward solution when either the resistivity or the cover thickness was varied. The amplitude and frequency of the oscillations were not affected by these factors.

Increasing either the resistivity or the cover thickness will consistently cause the algorithm to take longer to reach convergence. The effect of resistivity is easily explained by an examination of the differences between a forward solution with a resistivity of 150  $\Omega$ -m and one with a resistivity of 1500  $\Omega$ -m (Figure 4.11). Since the higher resistivity causes more extreme variations in the forward solution, which is the solution to which the inverse algorithm is supposed to converge, higher resistivity will result in a more complicated problem, which will result in a larger time of convergence.

## 4.6 Removal of Observation Points

The algorithm to deal with the removal of observation points is very simple, designed only to see how the main algorithm will handle the removal without making any effort to adjust the results. The initial potential distribution is interpolated from the observed data points using a Bezier curve [73]. This interpolated observed data is passed to the inverse problem to use as the initial value. The algorithm is then allowed to run as usual except that convergence is only evaluated at the remaining nodes. The potential is still calculated for all surface nodes.

Since the observation point removal test cases were expected to have the most trouble at the ends of the solution, the selected test case has a middle location for the anode. Any errors and oscillations that would occur in the test case would have to be the result of the algorithm, not of the end conditions, making it possible to

accurately assess the capabilities of the algorithm. An A/C ratio of 0.5 was used for the same reason. The selected test case had a resistivity of 1500  $\Omega$ -m and a cover thickness of 160 mm to eliminate any possible feedback effects.

Five test cases were run, a control test case with all 120 surface nodes, and then four more cases with 60, 40, 30 and 24 observed surface nodes. As expected none of the test cases converged and in general, the fewer the nodes that were observed, the larger the oscillations in the final solution.

Although it was expected that there would be a direct correlation between the number of observed data points and size of the oscillations, only a general trend was detected: some cases with fewer observed nodes had less oscillation. All test cases had the most oscillations in the transition area between the anode and cathode (Figures 4.24, 4.25, 4.26 and 4.27). The case with 24 observed nodes (Figure 4.27) had the largest oscillations, so large, in fact, that the shape of the potential distribution is obscured, however, the locations of the transition zones are fairly obvious from visual examination of the plot. This means that even if the inverse problem cannot give the exact shape of the potential distribution when fewer nodes are observed, the results are still useful for the determination of the locations of the anodes.

The effects of cover thickness are also easy to explain. If the cover thickness is decreased, there will be a better correlation between the potential on the interface and the potential on the surface, which would make it easier to find a solution on the interface with a cost function evaluated on the surface. The observed data which is used as the initial potential distribution will also be closer to the final solution, resulting in faster convergence. Unless the cover thickness is decreased to a point where feedback occurs, as previously discussed in PA 3: Domain Size, this assumption seems true in general.

It is useful to note that the case where 60 nodes were observed (Figure 4.24)

reached a final solution that is nearly identical to the control case where every node was observed. The location of the oscillations was different in this case, however, the amplitude appears to be no larger. This shows a strong robustness and resistance to oscillations for a small amount of missing data.

## 4.7 Summary of the Parametric Study

The inverse model produced results that were closely congruent to the data produced by the forward model. While the inverse model naturally produces small oscillations in the shape of the potential distribution, these oscillations do not obscure the shape of the distribution and information about the state of corrosion on the interface can still be drawn from the output potentials. Only test cases that used the Fletcher-Reeves equation converged because of that equations robustness. Test cases that had the anode located at one end of the domain in general had better rates of convergence. Except in a few cases where the anode was too small. the larger the anode, the more difficulty the algorithm had in reaching convergence. Resistivity and cover thickness both consistently cause the the time of convergence to increase as they increase.

The removal of observation points usually results in extreme oscillations and non-convergence, except in the case where every second node is observed. In this case the solution is consistently similar in shape and in the magnitude and frequency of oscillations to the control solution with all nodes observed. In other cases, despite the oscillations, it was possible to visually identify the anodic locations on the steel surface. However, it can be concluded in general that the fewer surface nodes are observed, the greater the amplitude of the oscillations in the final solution.

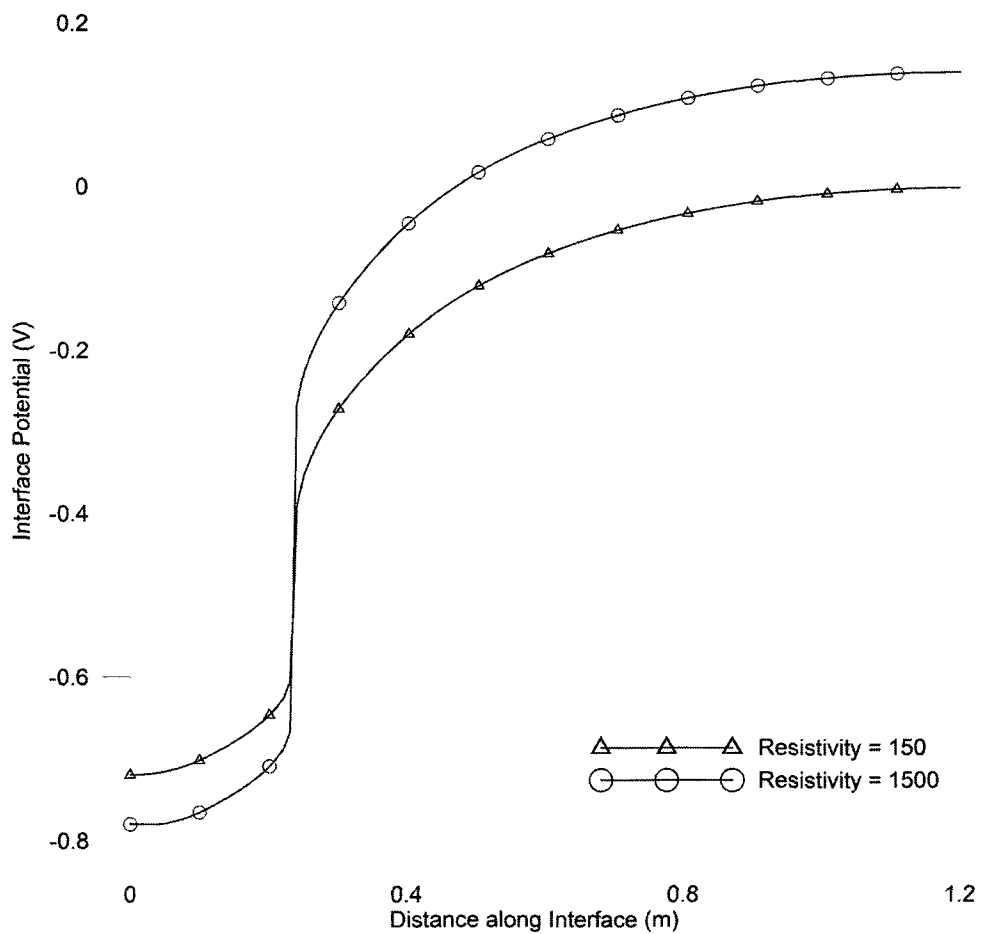


**Figure 4.11:** Comparison of the forward solution for two values of resistivity. Resistivity measure in  $\Omega\text{-m}$ .

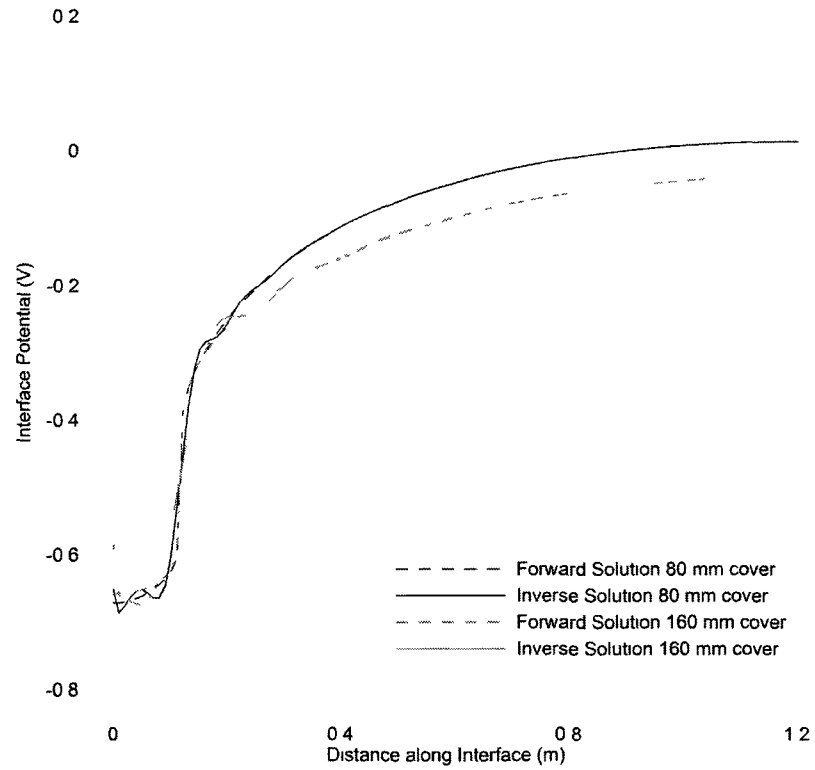


**Figure 4.12:** Comparison of the forward and inverse solutions with an end location for the anode, A/C ratio of 0.11, resistivity of 150  $\Omega$ -m.

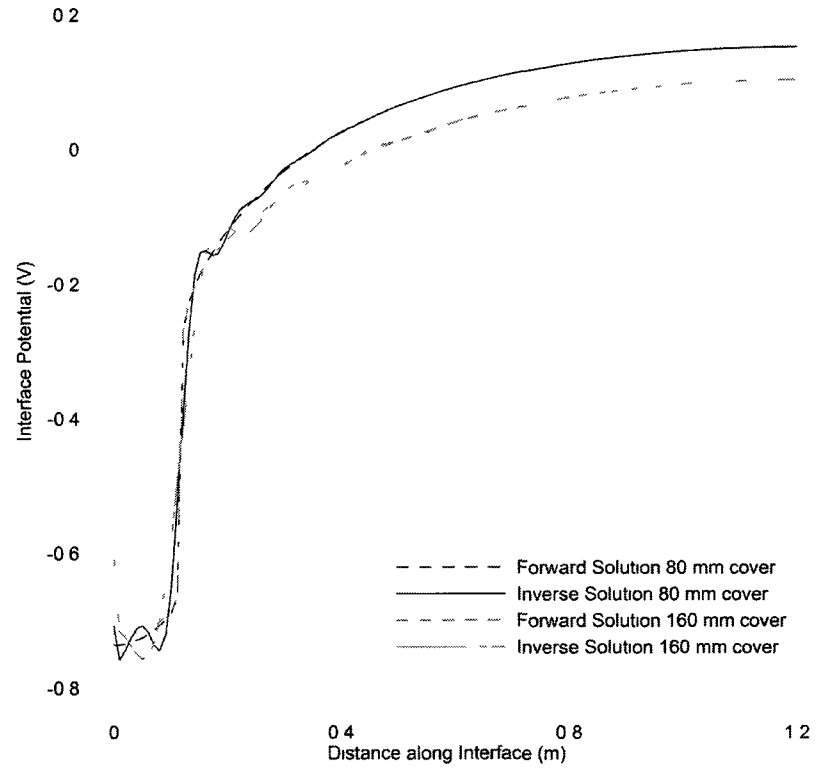


**Figure 4.13:** Comparison of the forward and inverse solutions with an end location for the anode, A/C ratio of 0.11, resistivity of 1500  $\Omega$ -m.

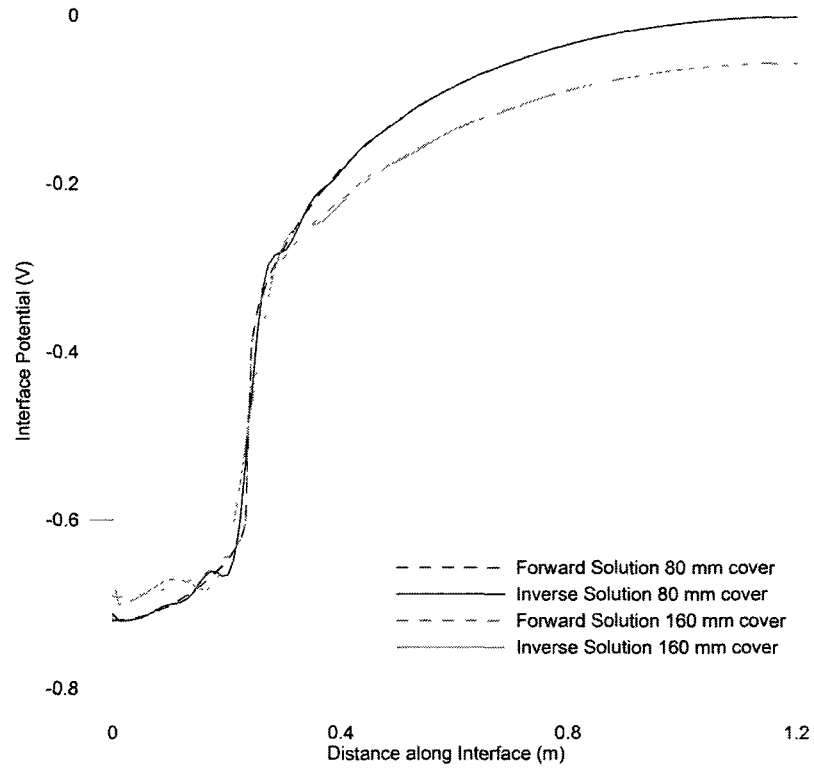


**Figure 4.14:** Comparison of the forward and inverse solutions with an end location for the anode, A/C ratio of 0.25, resistivity of  $150 \Omega\text{-m}$ .

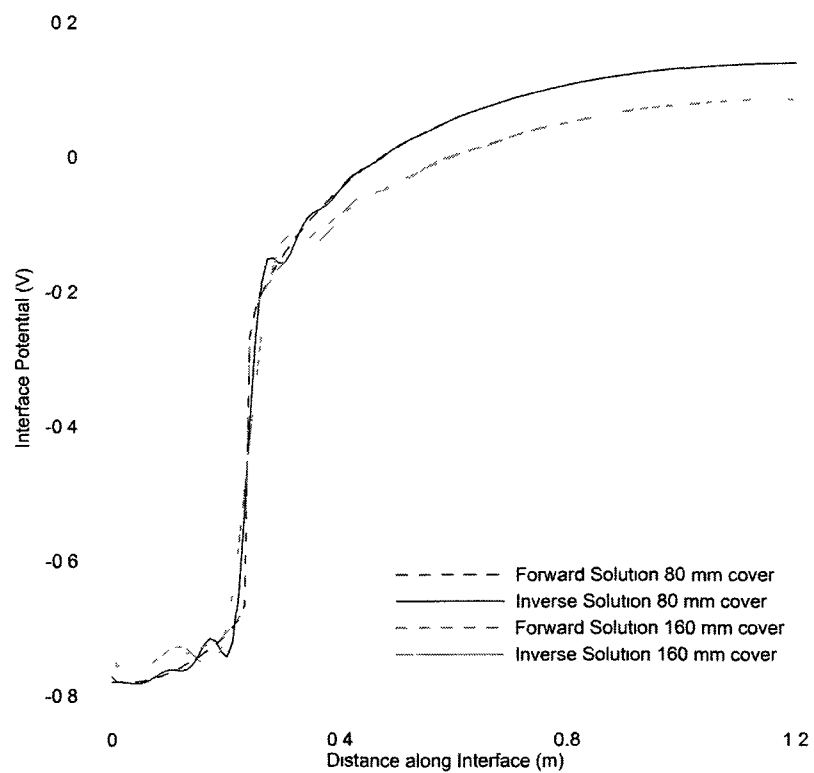


**Figure 4.15:** Comparison of the forward and inverse solutions with an end location for the anode, A/C ratio of 0.25, resistivity of  $1500 \Omega\text{-m}$ .

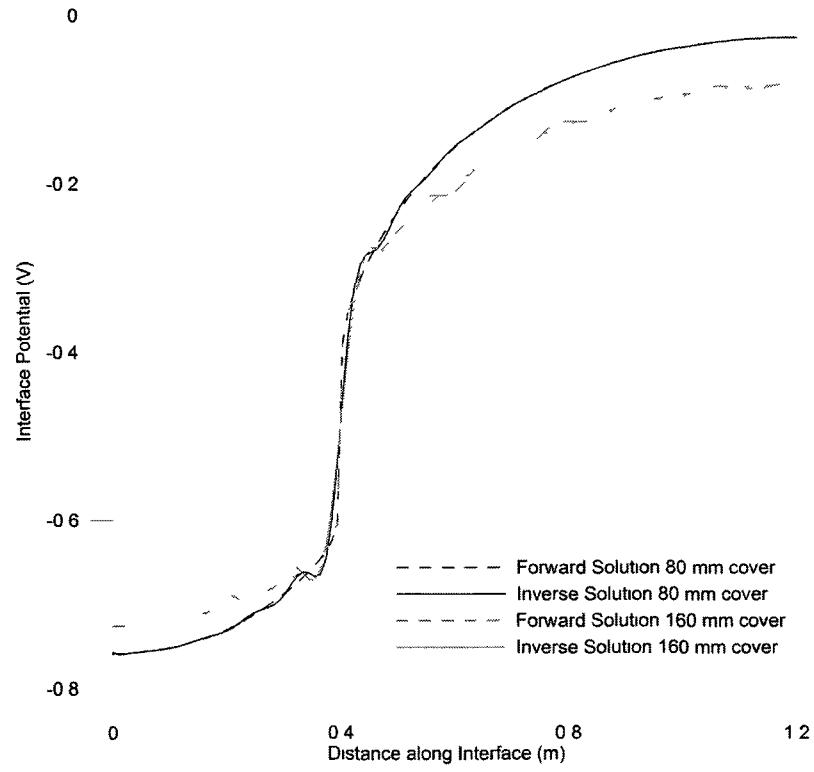


**Figure 4.16:** Comparison of the forward and inverse solutions with an end location for the anode, A/C ratio of 0.5. resistivity of 150  $\Omega$ -m.

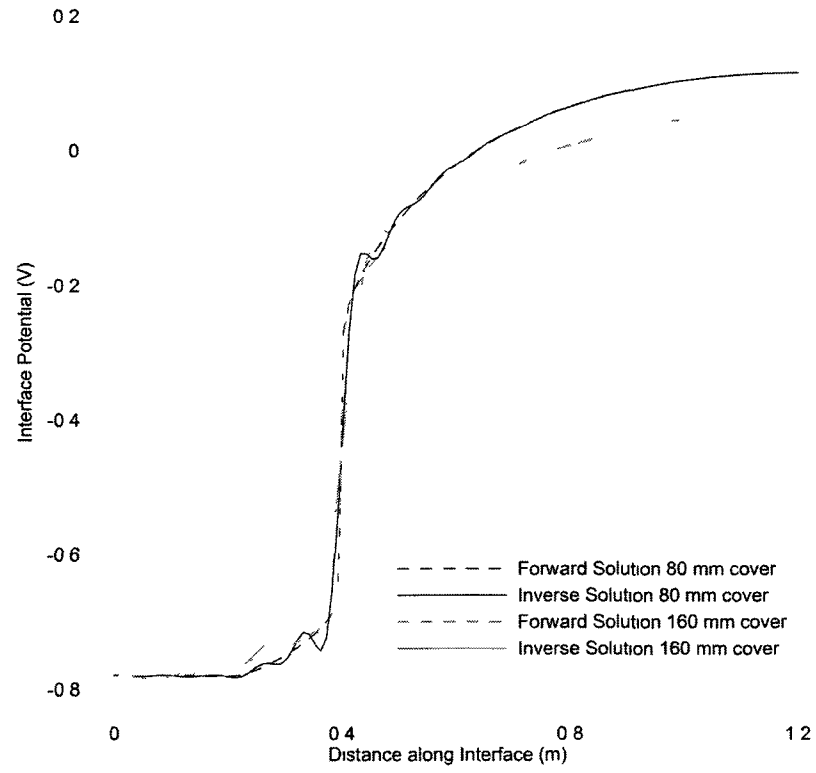


**Figure 4.17:** Comparison of the forward and inverse solutions with an end location for the anode, A/C ratio of 0.5, resistivity of 1500  $\Omega$ -m.

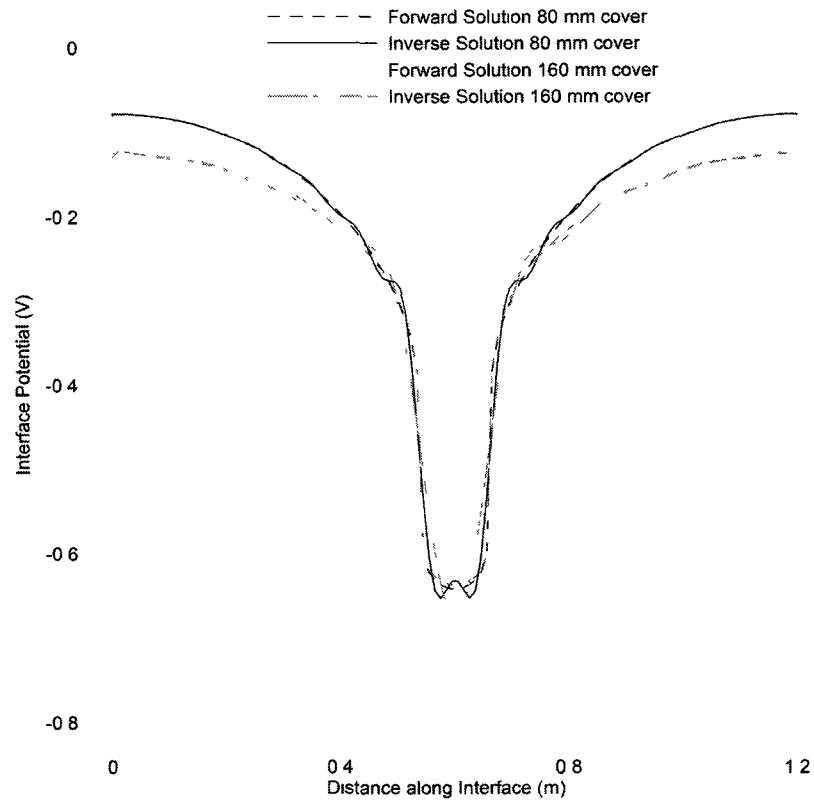


**Figure 4.18:** Comparison of the forward and inverse solutions with a middle location for the anode, A/C ratio of 0.11, resistivity of 150  $\Omega$ -m.

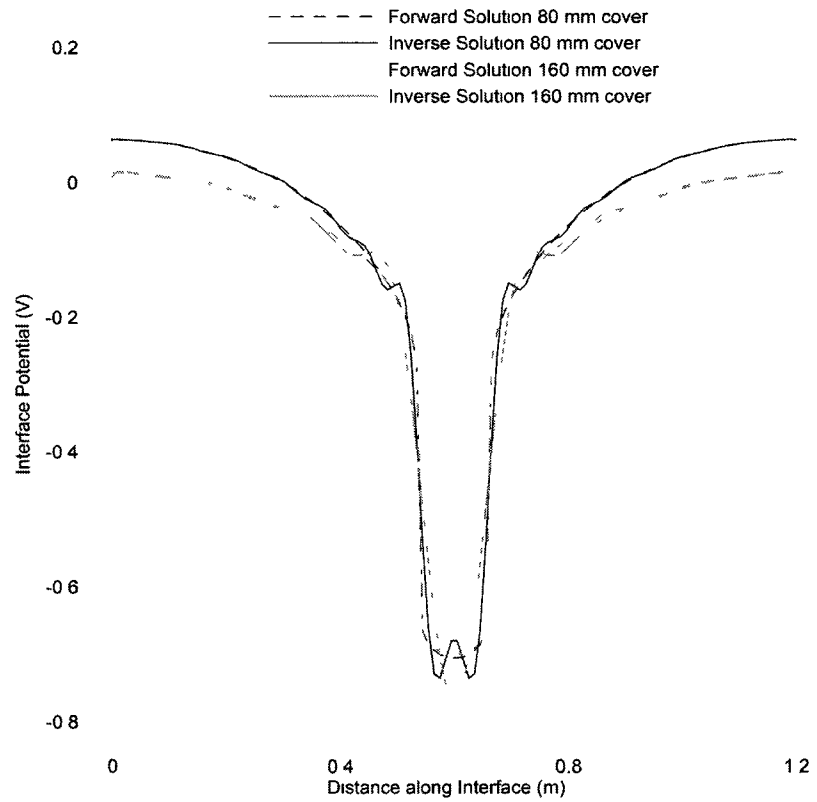


**Figure 4.19:** Comparison of the forward and inverse solutions with a middle location for the anode, A/C ratio of 0.11, resistivity of 1500  $\Omega$ -m.

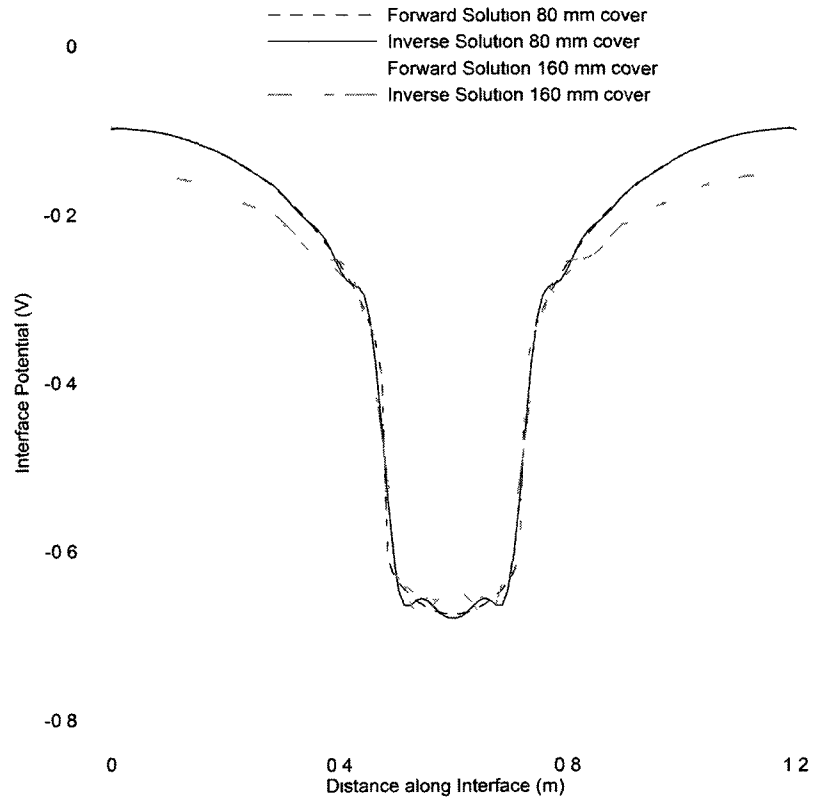


**Figure 4.20:** Comparison of the forward and inverse solutions with a middle location for the anode, A/C ratio of 0.25, resistivity of 150  $\Omega$ -m.

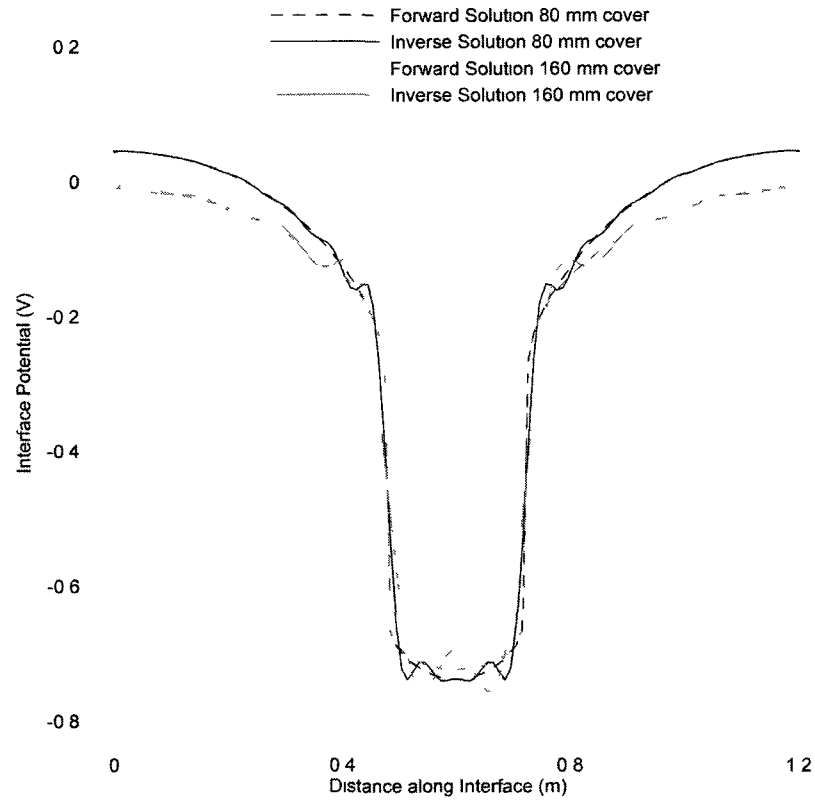


**Figure 4.21:** Comparison of the forward and inverse solutions with a middle location for the anode, A/C ratio of 0.25, resistivity of 1500  $\Omega$ -m.

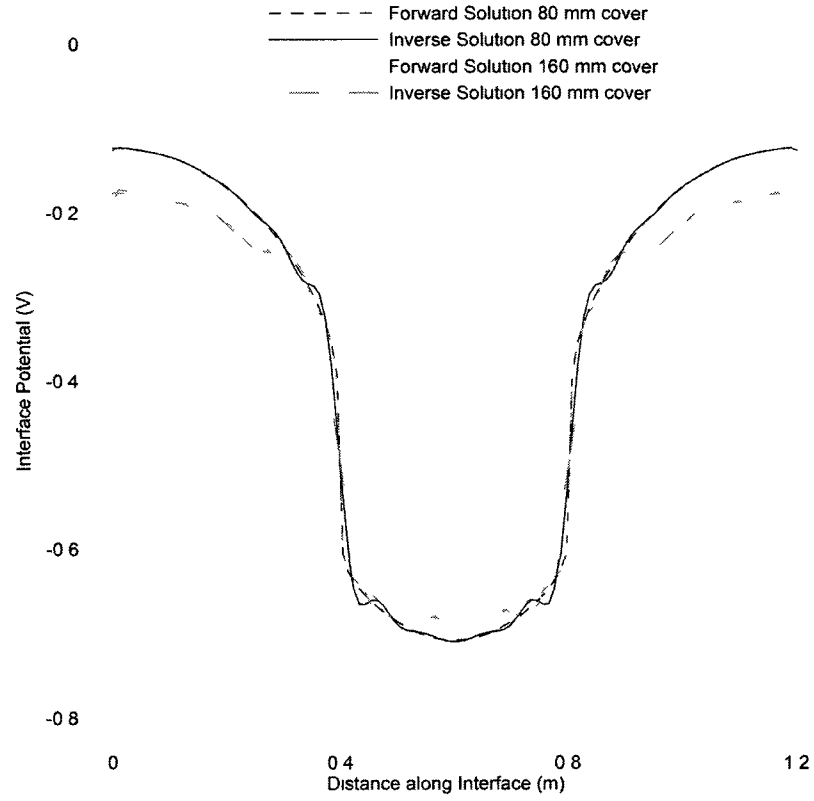


**Figure 4.22:** Comparison of the forward and inverse solutions with a middle location for the anode, A/C ratio of 0.5, resistivity of 150  $\Omega$ -m.

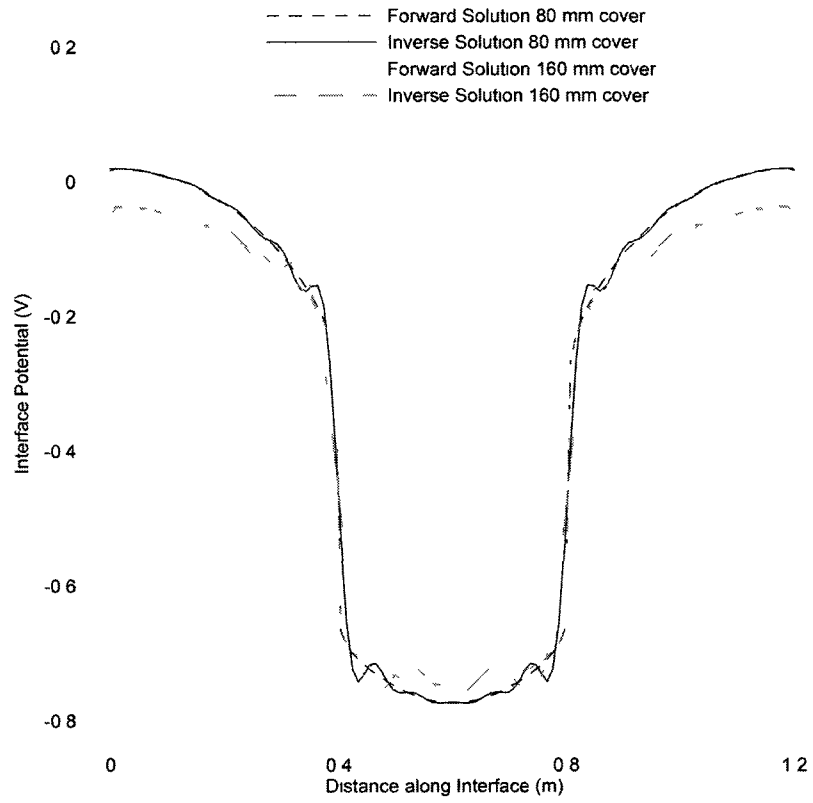


**Figure 4.23:** Comparison of the forward and inverse solutions with a middle location for the anode, A/C ratio of 0.5, resistivity of 1500  $\Omega$ -m.

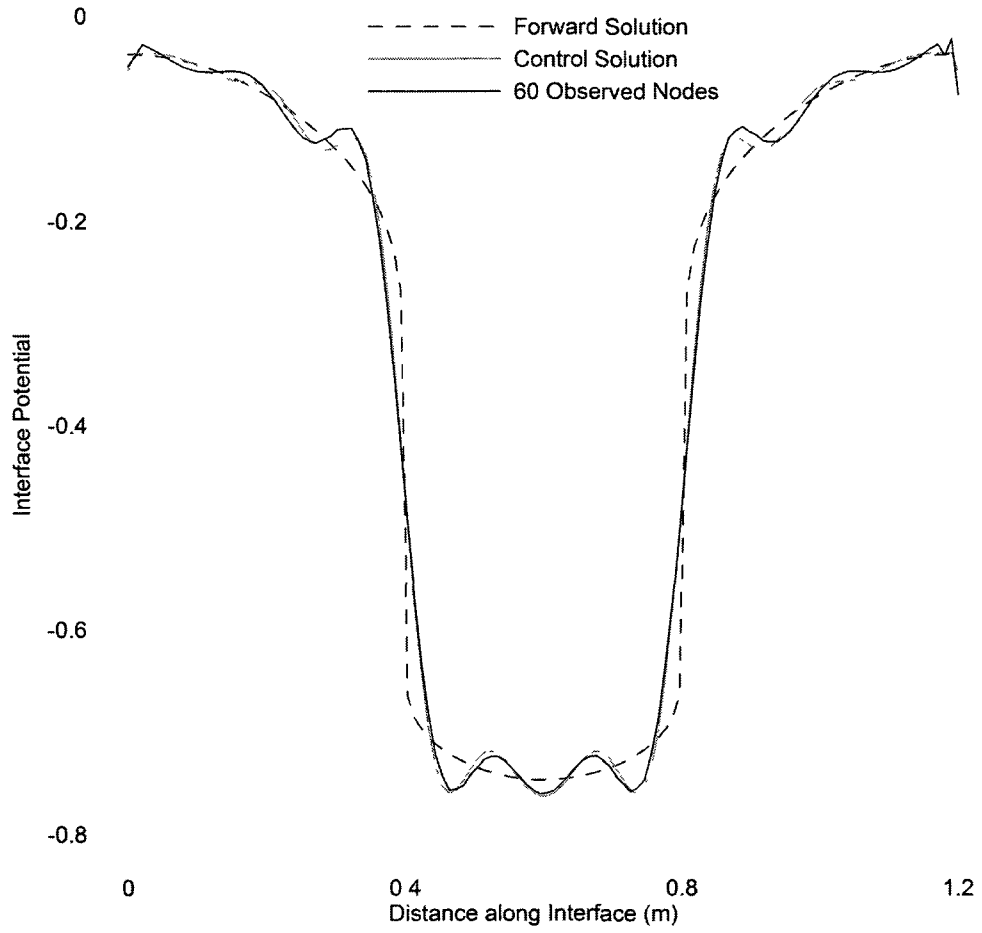


**Figure 4.24:** Comparison of the inverse solution with 60 observed nodes to the control solution and the forward solution.

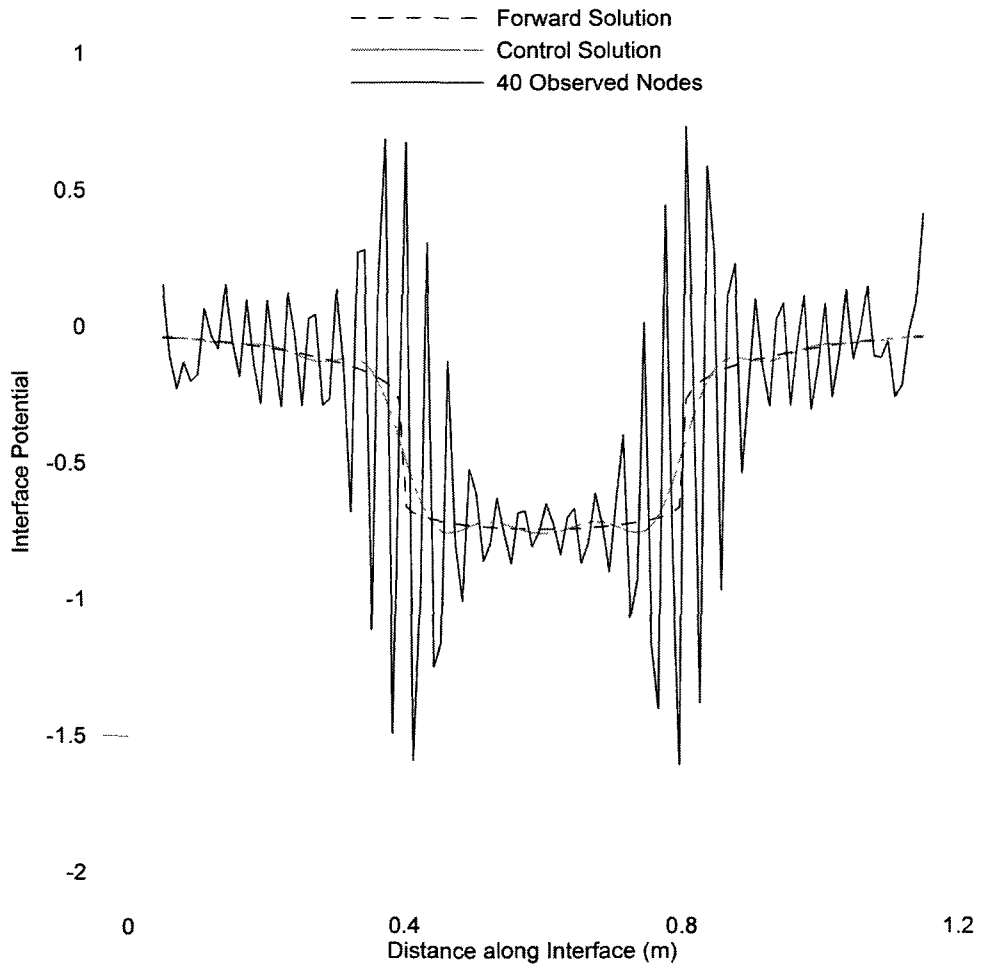


**Figure 4.25:** Comparison of the inverse solution with 40 observed nodes to the control solution and the forward solution.

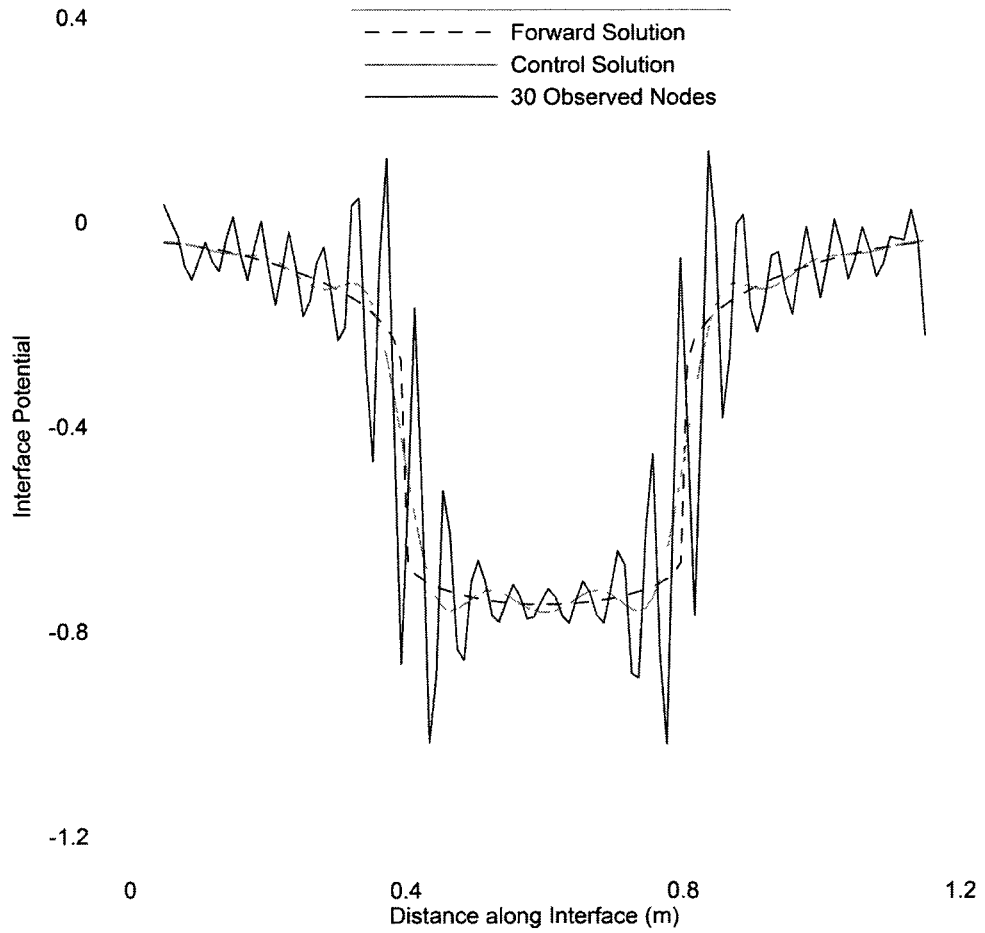


**Figure 4.26:** Comparison of the inverse solution with 30 observed nodes to the control solution and the forward solution.

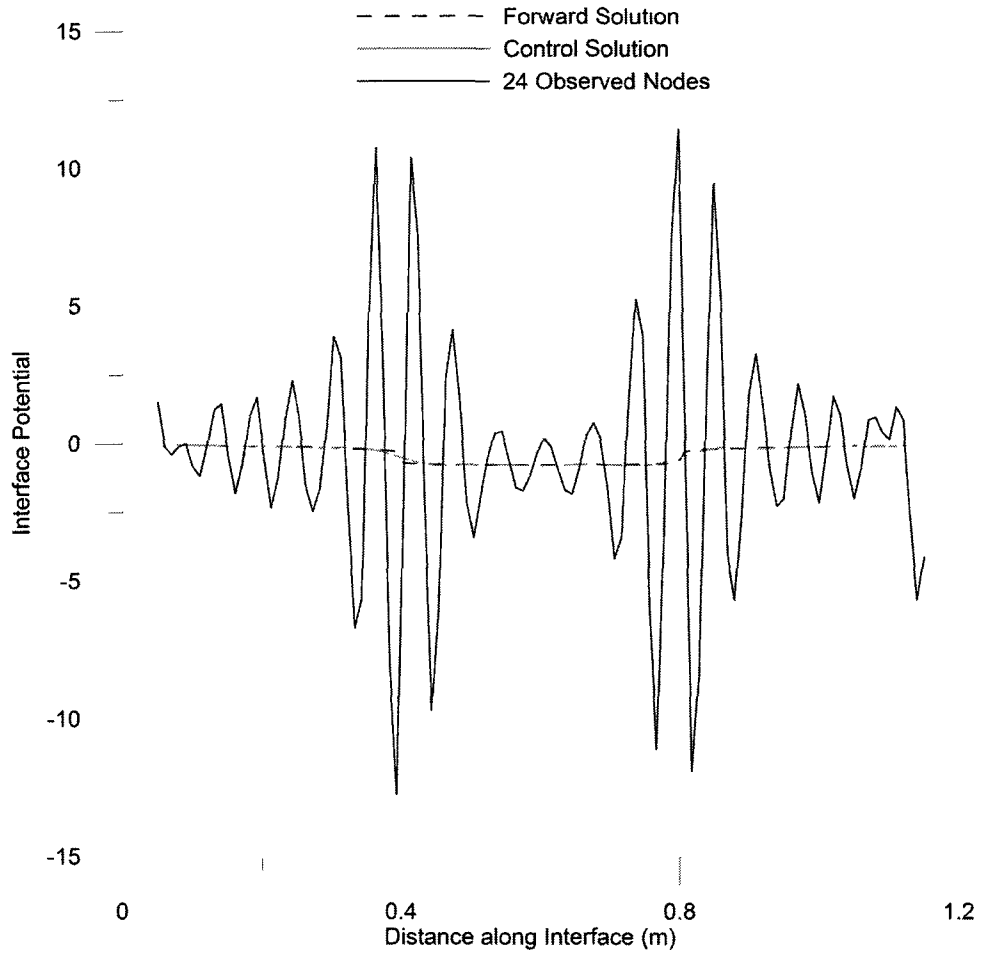


**Figure 4.27:** Comparison of the inverse solution with 24 observed nodes to the control solution and the forward solution.

## Chapter 5

# Studies on Systems with Multiple Anodes

### 5.1 General

While some cases of the corrosion of reinforcement in concrete can be represented by a single anode, as in the case of a single corroding pit on a reinforcement, the cases with multiple anodes separated by multiple cathodes are more commonly observed. Unless there is local damage, either to the reinforcement or to the concrete, depassivation usually takes place fairly randomly, and the initiation of the active stage of corrosion occurs at multiple locations on steel. Therefore, this chapter is dedicated to the investigation of the performance of the developed inverse model in identifying the sizes and locations of multiple anodes on a single reinforcement in concrete.

As in the previous chapter, the study of systems with multiple anodes was carried out in two stages: the preliminary analysis and parametric study. The same personal laptop computer that had been used in the numerical experiments presented in the previous chapter was also used for the simulations in this chapter.

Since there are many possible configurations of anodes and cathodes, unlike the previous chapter, the location of the anodes cannot be expressed as a single parameter. Therefore, four different configurations of anodes and cathodes, as illustrated

in Figure 5.1, were chosen in the parametric study. The first two configurations are matching symmetrical configurations with two anodes, with the first configuration having an A/C ratio that is half that of the second configuration. The third configuration is similar to the second except that the number of anodes is larger (3 anodes and 4 cathodes as opposed to the 2 anodes and 3 cathodes of the second configuration). The fourth and the last configuration is an asymmetrical configuration with one large and one small anode. Table 5.1 provides further details about these four configurations.

**Table 5.1:** Description of the anode configurations used in the studies on systems with multiple anodes.

Configuration	A/C ratio	Number of anodes	Symmetry
1	0.25	2	symmetrical
2	0.5	2	symmetrical
3	0.5	3	symmetrical
4	0.5	2	asymmetrical

These four configurations represent the optimum number of cases required to adequately examine the behaviour of the algorithm. They cover varying A/C ratios, varying number of anodes, and symmetrical versus asymmetrical layouts. The performance of the algorithm can be extrapolated to other cases based on these four configurations.

## 5.2 Preliminary Analysis

Since a detailed preliminary analysis was already carried out in Chapter 4, a more focused analysis is all that is necessary in this chapter. For example, separate element

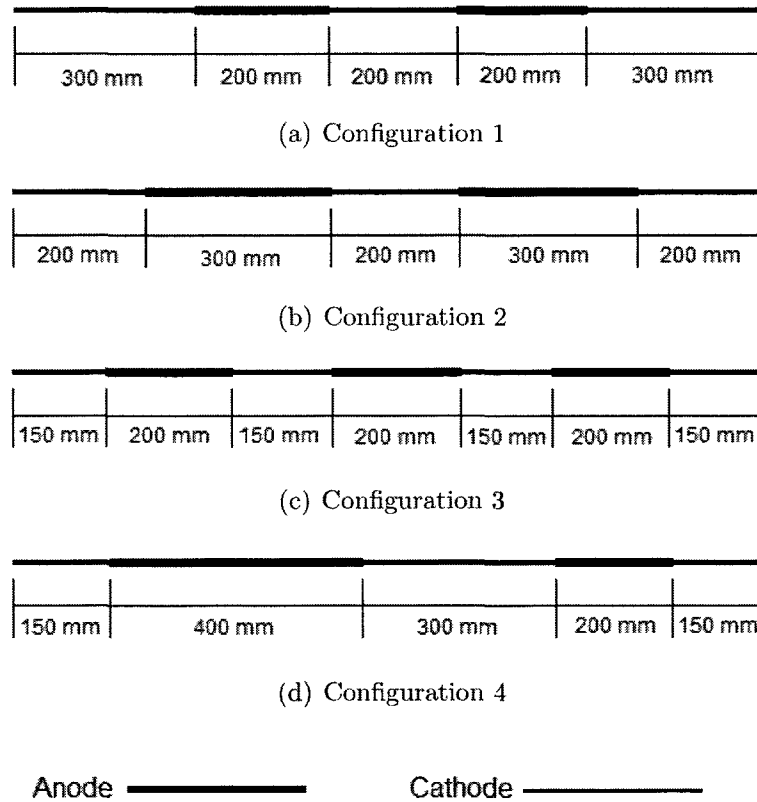


**Figure 5.1:** Anode configurations used in this study.

type, element size and domain size analyses were not carried out. The domain geometry for the identical twin numerical experiments in this chapter was the same as the one used in the parametric study of the previous chapter: 10 mm square units with crossed diagonals were used to discretise a 1200 mm long rectangular domain. The height of the domain, representing the concrete cover thickness, was varied as part of the parametric study.

The convergence tolerance of the inverse modelling algorithm was set to  $1 \times 10^{-8}$  for the single localised anode study. However, with multiple anodes, it is possible that the solution may tolerate a smaller limit; therefore, identical twin numerical experiments were designed to study the convergence criterion. Since the results from

the previous chapter showed that when the interval used in the calculation of  $\alpha$  was too small the algorithm had convergence issues, a new study was carried out to ensure that the value for the interval (1 as determined in the previous chapter) was large enough that the accuracy of the solution was not affected. The initial potential distribution along the steel/concrete interface was also investigated to determine if a more uniform or a more ideal initial distribution would help the convergence of a system with multiple anodes.

In the cases with a single anode and a cathode, the inverse solution did not experience significant oscillations. Minor oscillations may obscure the results slightly but since there is only one anode, its location is obvious from an examination of plot of the output potentials. In the case of multiple anodes, it is more desirable to smooth out the outputs so that small anodes will not be obscured by the oscillations of the algorithm. The algorithm needs to incorporate some form of regularisation to achieve these smoother results. Regularisation may also help to achieve convergence in cases experiencing difficulty.

In this investigation, four different regularisation cases were selected:

- R1: The smooth curve
- R2: The idealised solution with  $\kappa = 0.1$
- R3: The idealised solution with  $\kappa = 0.25$
- R4: The idealised solution with  $\kappa = 0.50$

Since the smooth curve, as discussed in chapter 3, is recalculated every iteration based on the current estimation for the solution, R1 is a dynamic regularisation method. Since the idealised solution is calculated once based on the observed data, R2, R3, and R4 are fixed. All test cases were run with a value of 0.1 for  $\omega$ . This

**Table 5.2:** Preliminary analysis test grid.

	Tolerance	$\alpha$ interval	Initial value	Regularisation
Perturbation (V)	$10^{-5}$	$10^{-5}$	$10^{-5}$	$10^{-5}$
$\alpha$ interval size	1	4 test cases <sup>a</sup>	1	1
Element Type	crossed	crossed	crossed	crossed
Element Size (mm)	10	10	10	10
Width (mm)	1200	1200	1200	1200
Cover (mm)	80	80	80	80
Resistivity ( $\Omega$ -m)	150	150	150, 1500	150
Initial Value	IP 4	IP 4	IP 1, IP 4, IP 5	IP 4
Tolerance	5 test cases <sup>b</sup>	$10^{-8}$	$10^{-8}$	$10^{-8}$
Regularisation	none	none	none	R1 to R4

<sup>a</sup>1, 10, 100, 1000

<sup>b</sup> $10^{-8}$ ,  $10^{-9}$ ,  $10^{-10}$ ,  $10^{-11}$ ,  $10^{-12}$

value represents the smallest value where the regularisation term can be expected to have a noticeable effect on the shape of the solution. This value was obtained by a comprehensive set of tests with a previous version of the algorithm using a single anode. A comparison was run between the current version of the algorithm and the previous version that determined that those results were still valid.

### 5.3 Parametric Study

The parametric study was carried out to determine the effect of physical parameters on the behaviour of the system. Since the four configurations of anodes described in Figure 5.1 and Table 5.1 are designed to cover different possibilities for A/C ratio, number of anodes and location of the anodes, these three parameters are not explicitly investigated. Only the resistivity and cover thickness need to be investigated. The

parameters varied over the course of these investigations are presented in table 5.3.

**Table 5.3:** Parameter study test grid.

Anode configuration	1, 2, 3 and 4
Concrete resistivity ( $\Omega\text{-m}$ )	150, 1500
Concrete cover thickness (mm)	80, 160

## 5.4 Results and Discussion: Preliminary Analysis

### 5.4.1 Convergence Criteria Analysis

In the hopes of improving the accuracy of the solution, a convergence criteria analysis was carried out. The tolerance was varied over 5 values:  $1 \times 10^{-8}$ ,  $1 \times 10^{-9}$ ,  $1 \times 10^{-10}$ ,  $1 \times 10^{-11}$  and  $1 \times 10^{-12}$ . Unfortunately, none of the test cases converged below a tolerance of  $1 \times 10^{-8}$ . This value was therefore used as the tolerance for the rest of the identical twin numerical experiments in this chapter.

### 5.4.2 Interpolation of $\alpha$

The interval size that is used in the quadratic interpolation process to determine the value of  $\alpha$  plays a large role in the determining the rate of convergence of the final solution. A study was carried out to determine if a value for the interval size that was larger than that used in the previous chapter would help improve the convergence of the cases with multiple anodes. Four interval sizes were investigated: 1, 10, 100 and 1000. The algorithm was allowed to run for a full 5000 iterations to see the value to which the cost function converges. Table 5.4 provides a summary of the results.

As it can be seen in Table 5.4. the interval size has very little effect on the final

value for the cost function. Although the efficiency may be improved by selecting a larger value, the studies in the previous chapter conclusively demonstrated that there is a marked increase in efficiency by using a value of 1 as opposed to a smaller value. In the interests of consistency, an investigation into the efficiency of the larger values for the interval size was not conducted; therefore, if the interval size of 1 resulted in the same accuracy for the final solution as the higher values for the interval, it was considered to be acceptable. The interval size of 1 for the calculation  $\alpha$  was therefore chosen as the optimal value and was used in the parametric study.

**Table 5.4:** Final cost function depending on the interval size used to approximate  $\alpha$ .

Interval size	1	10	100	1000
Configuration 1	$3.8438 \times 10^{-9}$	$3.8438 \times 10^{-9}$	$3.8438 \times 10^{-9}$	$3.8438 \times 10^{-9}$
Configuration 2	$3.1566 \times 10^{-9}$	$3.1566 \times 10^{-9}$	$3.1567 \times 10^{-9}$	$3.1567 \times 10^{-9}$
Configuration 3	$3.0504 \times 10^{-9}$	$3.0504 \times 10^{-9}$	$3.0504 \times 10^{-9}$	$3.0504 \times 10^{-9}$
Configuration 4	$3.0496 \times 10^{-9}$	$3.0583 \times 10^{-9}$	$3.0583 \times 10^{-9}$	$3.0496 \times 10^{-9}$

### 5.4.3 Initial Potentials along Steel/Concrete Interface

For cases with a single localised anode, the use of the observed potentials on the concrete surface (IP 4) was determined to be the optimal initial potential distribution to be used on the steel/concrete interface. Therefore, this case as well as two more cases that were tested (and which performed well) in Chapter 4 will be investigated in this study. The two additional cases are the constant zero potential (IP 1) and the idealised function with  $\kappa = 0.1$  (IP 5).

By examining the times of convergence in Table 5.5, it is clear that IP 4 is still the best choice for the initial potential distribution on the Steel/Concrete interface.

The shape of the solution (Figure 5.2), especially at the ends of the domain (Figures 5.3 and 5.4), also suggests that the observed data is the best choice.

**Table 5.5:** Times of convergence of the inverse model depending on the initial potentials on steel/concrete interface.

	$\rho = 150 \Omega\text{-m}$			$\rho = 1500 \Omega\text{-m}$		
	IP 1	IP 4	IP 5	IP 1	IP 4	IP 5
Time (s)	23.59	10.31	12.83	16.84	11.67	15.2
Iterations	136	60	73	98	67	87

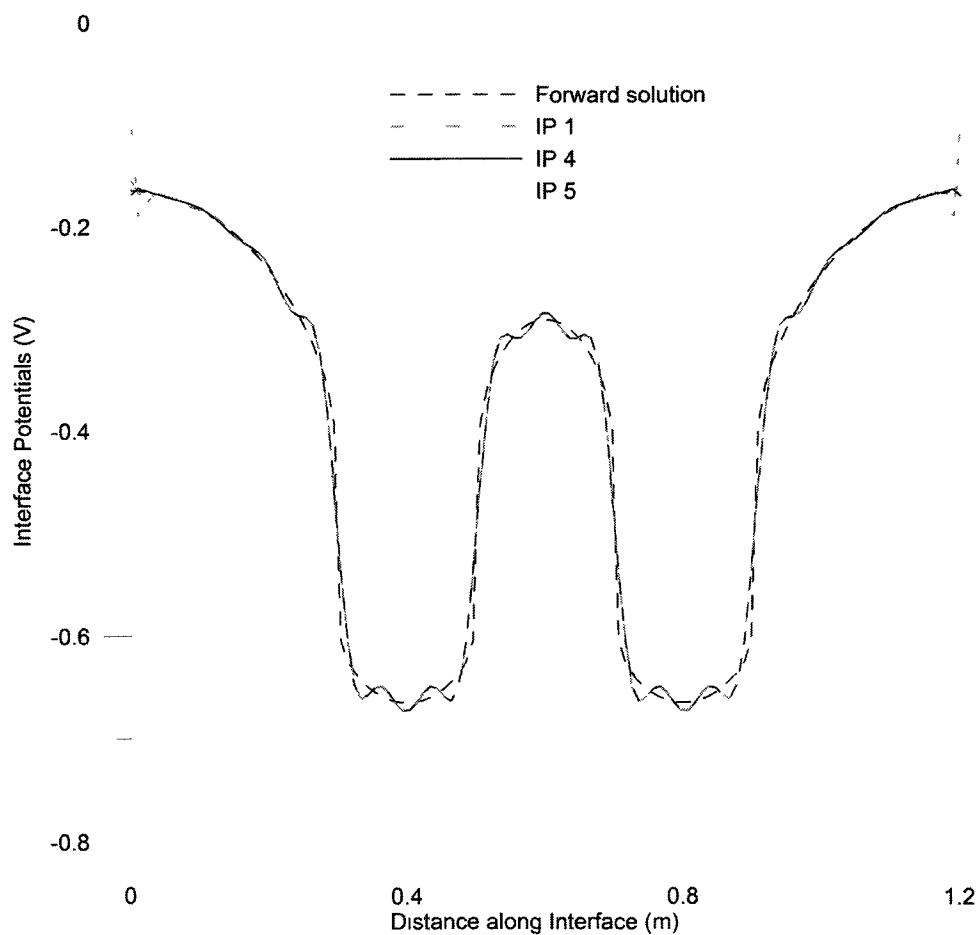


**Figure 5.2:** Inverse solution for the interface potential depending on the initial potential distribution.

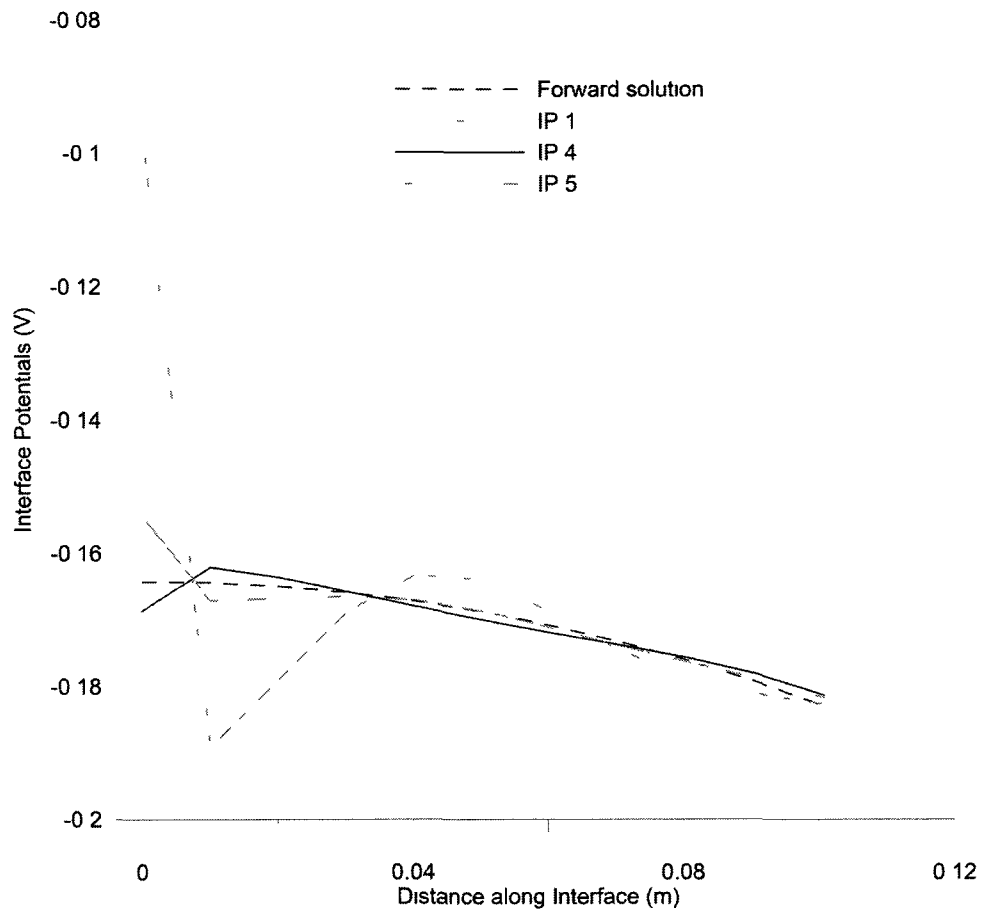


**Figure 5.3:** Close up of the left side of the inverse solution for the interface potential depending on the initial potential distribution.

#### 5.4.4 Regularisation Analysis

An attempt was made to eliminate the oscillations in the final solution by the use of regularisation, however, none of the test cases converged. This is easily explained by the fact that the idealised function was only an approximation of the true solution. As the algorithm attempts to reach convergence, it approaches the true solution, diminishing the contribution of the data misfit measure. The regularisation term then controls the shape of the equation, however, the algorithm cannot balance the conflicting needs to conform to both the true solution and to the ideal solution. The obvious answer is to reduce the value of  $\omega$ ; however, reducing  $\omega$  reduces the

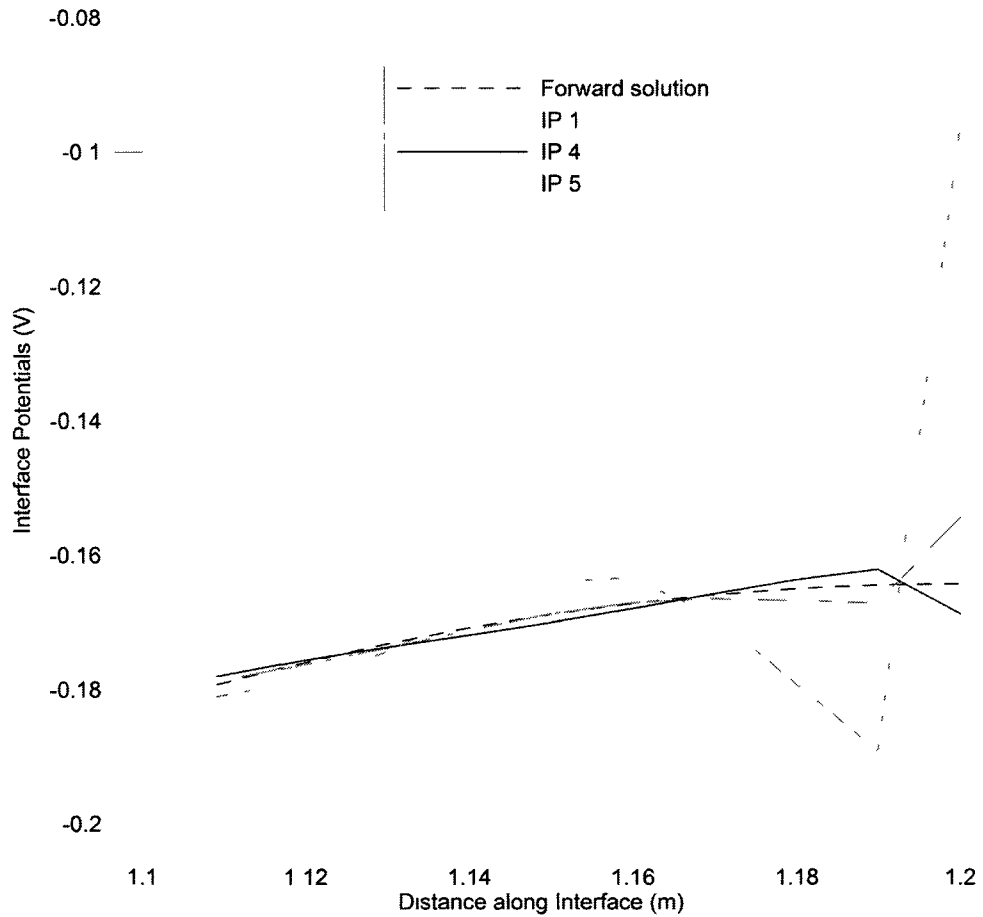


**Figure 5.4:** Close up of the right side of the inverse solution for the interface potential depending on the initial potential distribution.

contribution of the regularisation term. If  $\omega$  were to be reduced to a point where the solution could reach convergence, the contribution of the regularisation term would be negligible.

The smooth curve introduces extreme changes into the estimated solution at each iteration. It was hoped that the algorithm would be forced to converge to a solution that was smoother by forcing smoothness on the solution in such a manner. However, it is clear that the algorithm naturally develops oscillations and cannot reach convergence when such a large change is introduced. A new method must therefore be found to regularise this algorithm.

## 5.5 Results and Discussion: Parametric Study

All numerical test cases were carried out with a convergence criteria of  $1 \times 10^{-8}$ . The concrete cover thickness was either 80 mm or 160 mm, resistivity was set at either 150  $\Omega$ -m, or 1500  $\Omega$ -m. Since the results of the parametric study represent the effect of different parameters for a single numerical experiment, they are presented as a whole at the end of the chapter.

### 5.5.1 Effect of Resistivity and Cover Thickness

The resistivity was varied over 150  $\Omega$ -m and 1500  $\Omega$ -m and the cover thickness was varied over 80 mm and 160 mm. Three of the test cases did not converge to a result below the specified tolerance. The test cases that did not converge had a cover thickness of 160 mm as opposed to 80 mm (Table 5.6). In the cases where convergence was achieved, there is a clear and consistent increase in the time of convergence as cover thickness increases.

This result is expected since as the cover thickness increases the difference between the potential on the interface and the potential on the surface of the concrete also increases. Since the algorithm is trying to find the potential distribution on the interface that causes the potential distribution on the surface, the decrease in correlation creates a more difficult problem. However, when Configuration 1 was tested, the solution converged in the case where the resistivity was 150  $\Omega$ -m and not in the case where it raised to 1500  $\Omega$ -m. Since increasing the resistivity increases the difference between the surface and the interface potential distributions, this effect cannot explain this case. The forward solution is also affected by the resistivity, causing the true solution to be more extreme, with steeper slopes and a larger difference between the minimum and maximum values (Figures 5.5 and 5.6). The algorithm seems the

have less difficulty with reaching convergence when given this more extreme shape.

### 5.5.2 Effect of the A/C Ratio

The A/C ratio was primarily investigated by examining Configuration 1 and Configuration 2 since these two configurations are nearly the same except for a change in the A/C ratio. The symmetrical configuration with the A/C ratio of 0.5 (Configuration 2) had the the most difficulty achieving convergence. In both cases where the cover was increased to 160 mm the algorithm did not converge. By comparison, the same configuration with an A/C ratio of 0.25 (Configuration 1) consistently had better times of convergence and converged in three cases out of four, as shown in Table 5.6. Since all the other configurations had the same A/C ratio, and performed much better than Configuration 2, it can be concluded that increasing the A/C ratio does not cause problems for the algorithm.

An alternate explanation for the poor performance of Configuration 2 is the absolute size of the anodes and the spacing between them. As noted above, the first and second configurations performed the poorest. Configuration 1 is simply Configuration 2 with half the A/C ratio. As determined in the previous chapter, the algorithm had more trouble as the anode size increased. Since the third and fourth configurations have the same A/C ratio but different absolute sizes and spacings for the anodes, it can be assumed that the issue is in fact the size and spacing of the anodes.

### 5.5.3 Effect of Increasing the Number of Anodes

The configuration where the number of anodes was increased (Configuration 3) converged for all cases (see Figures 5.9 and 5.10). The algorithm did struggle in the cases with larger cover thicknesses but it performed much better than Configuration

2 which has only two anodes and the same A/C ratio (see Figures 5.7 and 5.8).

Since increasing the number of anodes decreased the size of each individual anode, and since the algorithm had less difficulty reaching convergence in the case with multiple smaller anodes, it can be concluded that the size of the anode has a much greater effect than the number of anodes.

#### **5.5.4 Effect of Asymmetry**

The asymmetrical configuration (Configuration 4) had the best times of convergence and converged to reasonable results (see Figures 5.11 and 5.12). This configuration had one large anode that is larger than any other configuration and one small anode. This suggest that the algorithm converges best with asymmetrical configurations and that the effects that were attributed to anode size and spacing may instead be a result of a regular configuration. It is most likely that the cause is a combination of several factors.

### **5.6 Removal of Observation Points**

The model with multiple anodes performed in a similar fashion when the number of observed nodes was reduced to the model with a single localised anode. The case where every second node was observed (60 nodes) produced a solution that was nearly identical to the control solution where all the nodes were observed. As fewer nodes were observed, the model generally produced more oscillations. When only 24 nodes were observed, the oscillations were so large as to nearly obscure the shape of the distribution.

The ends of the domain caused the most difficulty for the algorithm and so the

**Table 5.6:** Times of convergence of the inverse model for all four anode configurations.

	$\rho = 150 \Omega\text{-m}$		$\rho = 1500 \Omega\text{-m}$	
	80 mm	160 mm	80 mm	160 mm
Configuration 1				
Computation Time (s)	10.62	1852.74	11.72	35.62
Iterations	60	5002	67	96
Configuration 2				
Computation Time (s)	32.84	1851.95	16.00	1858.97
Iterations	187	5002	91	5002
Configuration 3				
Computation Time (s)	10.01	420.59	20.26	134.4
Iterations	57	1119	116	364
Configuration 4				
Computation Time (s)	10.97	45.06	19.38	60.52
Iterations	63	121	109	162

first and last five nodes were excluded from the plots of the potential distribution to better present the results.

Configuration 1 (Figures 5.13, 5.14, 5.15 and 5.16) showed a consistent amplitude of oscillations over the entire domain. The shape of the final solution is still visible and the potentials at the anodic and cathodic locations can be approximated by taking an average.

Configuration 2 (Figures 5.17, 5.18, 5.19 and 5.20) showed a diminishing of the amplitude of the oscillations in the anodic regions. In some cases, notably the case with 40 observed nodes (Figure 5.18), a diminishing of the amplitude over the middle

cathodic region also occurs. Presumably, this effect is caused by the fact that the anodes are large enough to diminish the uncertainty caused by the removal of observed nodes. Since the model only compares the calculated values at the nodes where there exists an observed when determining the cost function, when there are less observed nodes, it introduces uncertainty into the model, which is reflected by the amplitude of the oscillations.

Configuration 3 (Figures 5.21, 5.22, 5.23 and 5.24) showed a fairly constant amplitude of oscillation over the entire domain. This appears to be because of the regular spacing between anodes, and the relatively small size of the anodes.

Configuration 4 (Figure 5.25, 5.26, 5.27 and 5.28) shows a reduced amplitude of oscillation over the large anode and the large cathode, confirming the earlier conclusion that the size of the anodic or cathodic region was directly related to the ease of the convergence. In some cases, notably figure 5.26 the small anode also showed a reduced amplitude of oscillation. This effect seems to be caused by the fact that the spacing and sizing of the anodes is not regular. In the symmetrical cases, the algorithm has more difficulty achieving convergence suggesting that asymmetry plays an important role in the ease of convergence.

## 5.7 Summary of the Parametric Study

The inverse solution algorithm performs best when the spacing between anodes is not regular and when the sizes of the anodes are different. The solution that had the most difficulty reaching convergence was obtained with Configuration 2, the configuration with cathodes of all similar length and anodes of the same size. Reduction of the A/C ratio, helped one case to converge (Configuration 1) that previously did not

(Configuration 2). Addition of anodes helped all the cases reach convergence (Configuration 3), possibly because of a reduction of the size of the individual anodes, and the introduction of asymmetry had the best overall effect on the performance of the algorithm (Configuration 4). This is promising for applications in the field where regular spacing of anodes and cathodes is not likely to be observed.

Even in the cases where the algorithm did not reach convergence, the algorithm gave results that could be used to reasonably approximate the location of the anodes. Figures 5.5, 5.7 and 5.8 include solutions that did not reach convergence as shown in Table 5.6 by cases for which the number of iterations exceeded 5000, the maximum specified limit for the number of iterations. The accuracy may not be as high as the specified criterion, but for practical use, the algorithm already performs well enough.

The performance of the algorithm with the removal of observed nodes was similar in the case of multiple anodes to the case of a single localised anode. The case with 60 observed nodes was consistently almost identical to the the control solution where all nodes were observed. The model seemed to have the least difficulty reaching convergence in cases with large anodes, such as Configuration 2 and Configuration 4. In general, the fewer the number of nodes that were observed, the poorer the performance of the model.

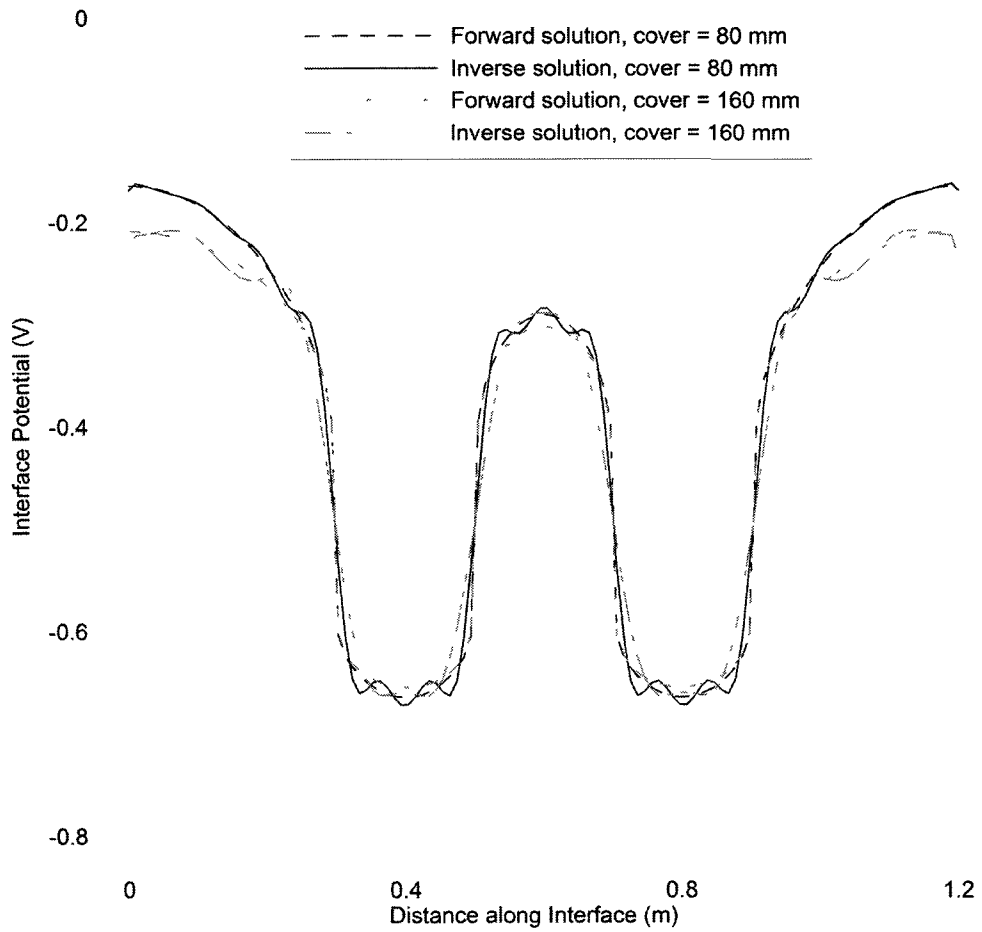


**Figure 5.5:** Comparison of the forward and inverse solutions with Configuration 1 and a resistivity of  $150 \Omega\text{-m}$ .

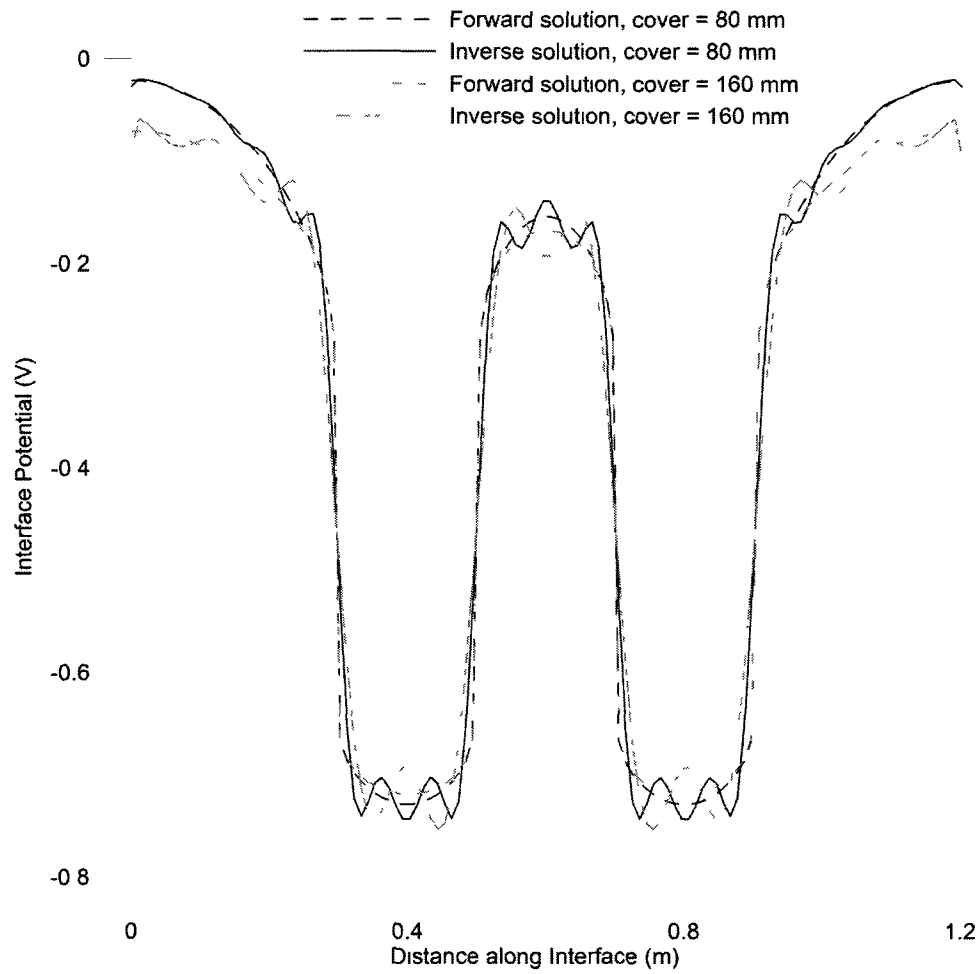


**Figure 5.6:** Comparison of the forward and inverse solutions with Configuration 1 and a resistivity of  $1500 \Omega\text{-m}$ .

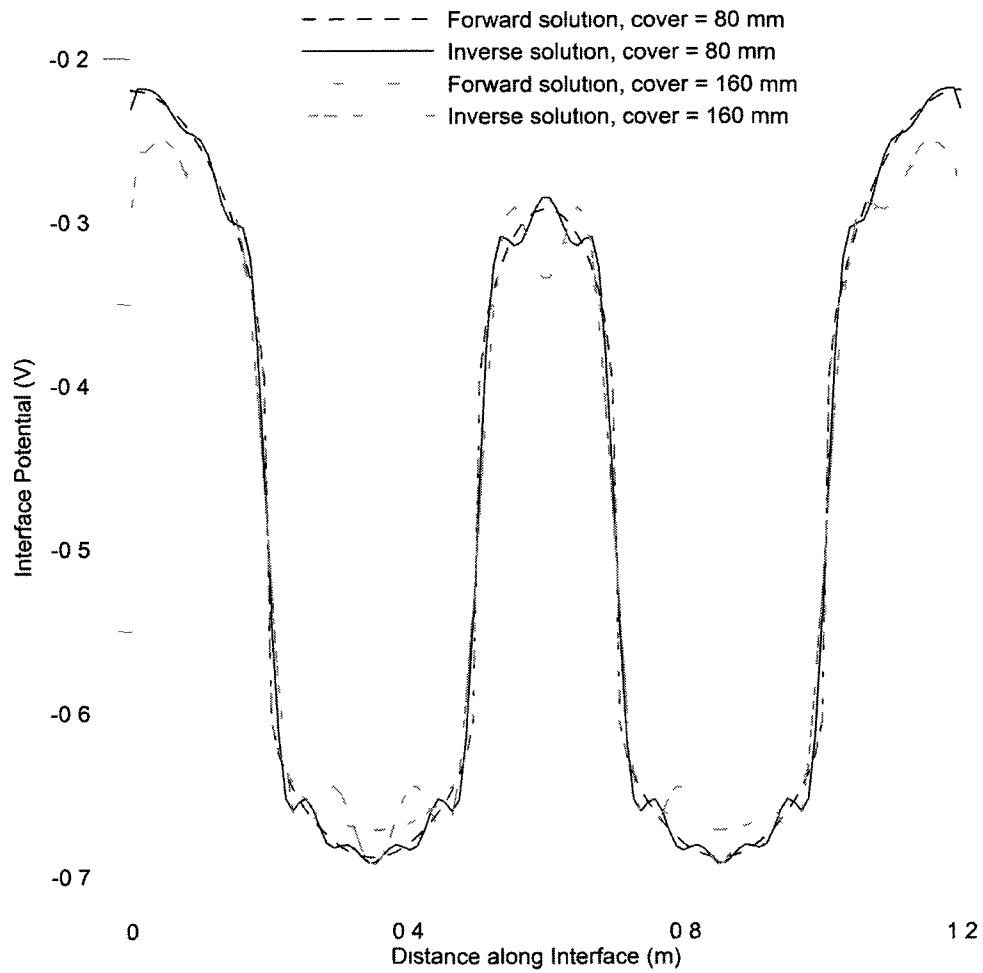


**Figure 5.7:** Comparison of the forward and inverse solutions with Configuration 2 and a resistivity of  $150 \Omega\text{-m}$ .

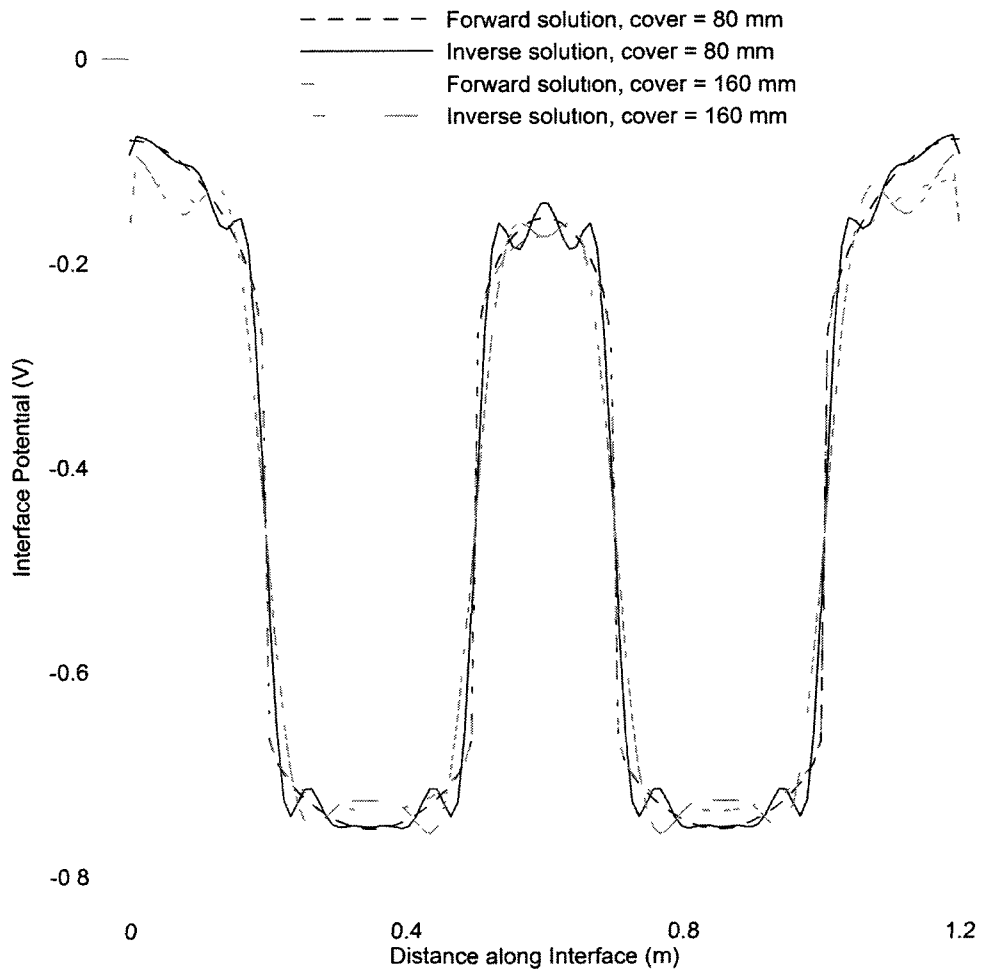


**Figure 5.8:** Comparison of the forward and inverse solutions with Configuration 2 and a resistivity of  $1500 \Omega\text{-m}$ .

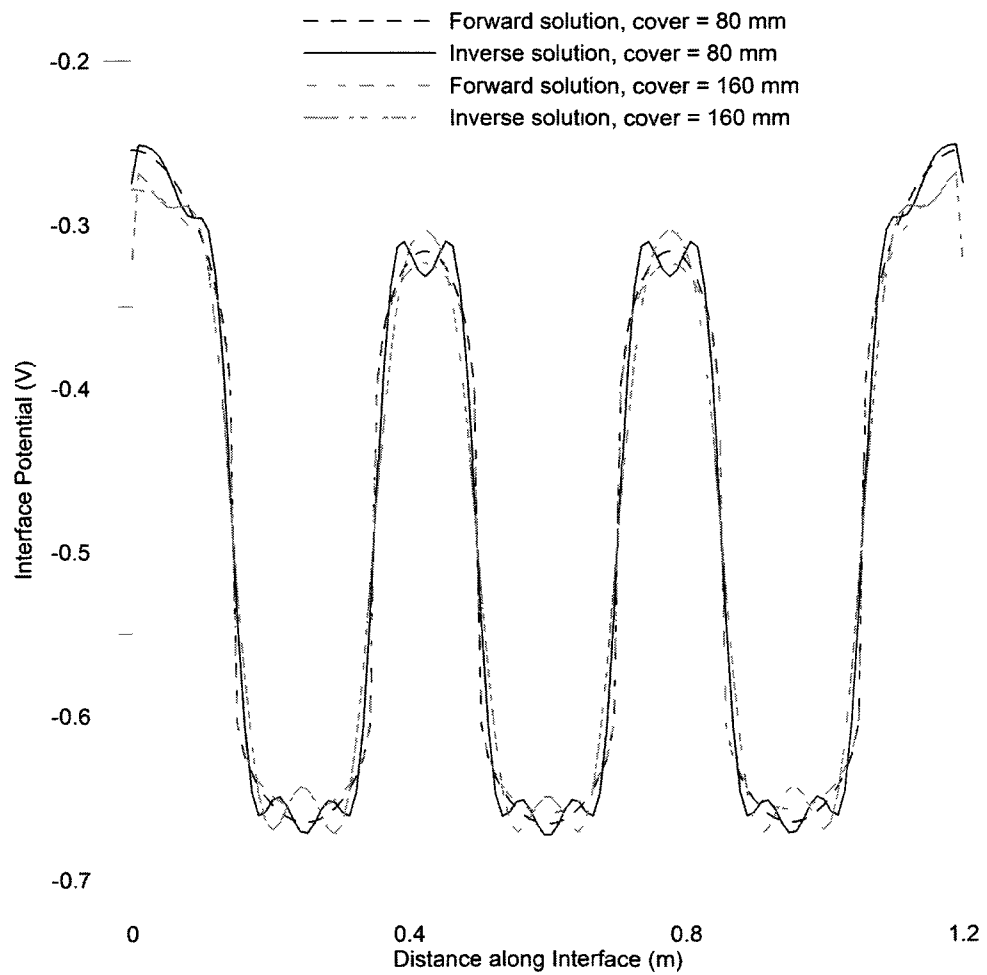


**Figure 5.9:** Comparison of the forward and inverse solutions with Configuration 3 and a resistivity of  $150 \Omega\text{-m}$ .

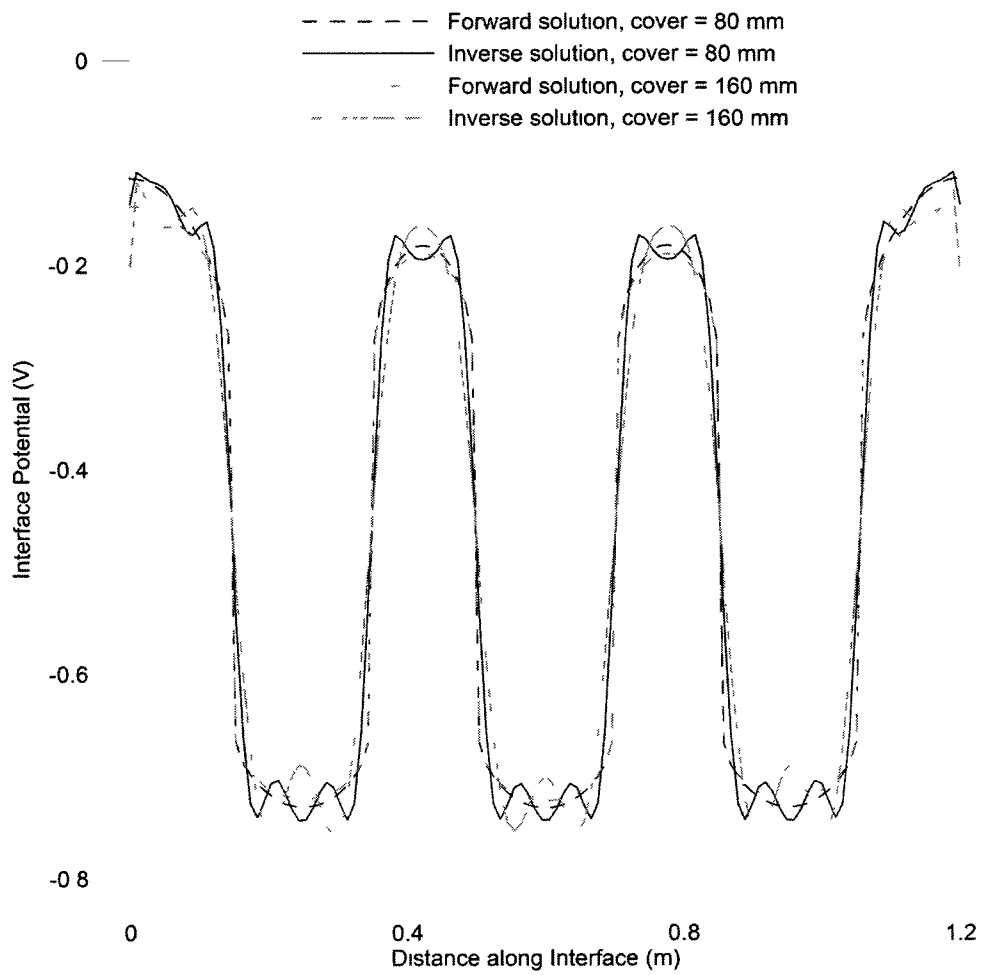


**Figure 5.10:** Comparison of the forward and inverse solutions with Configuration 3 and a resistivity of  $1500 \Omega\text{-m}$ .

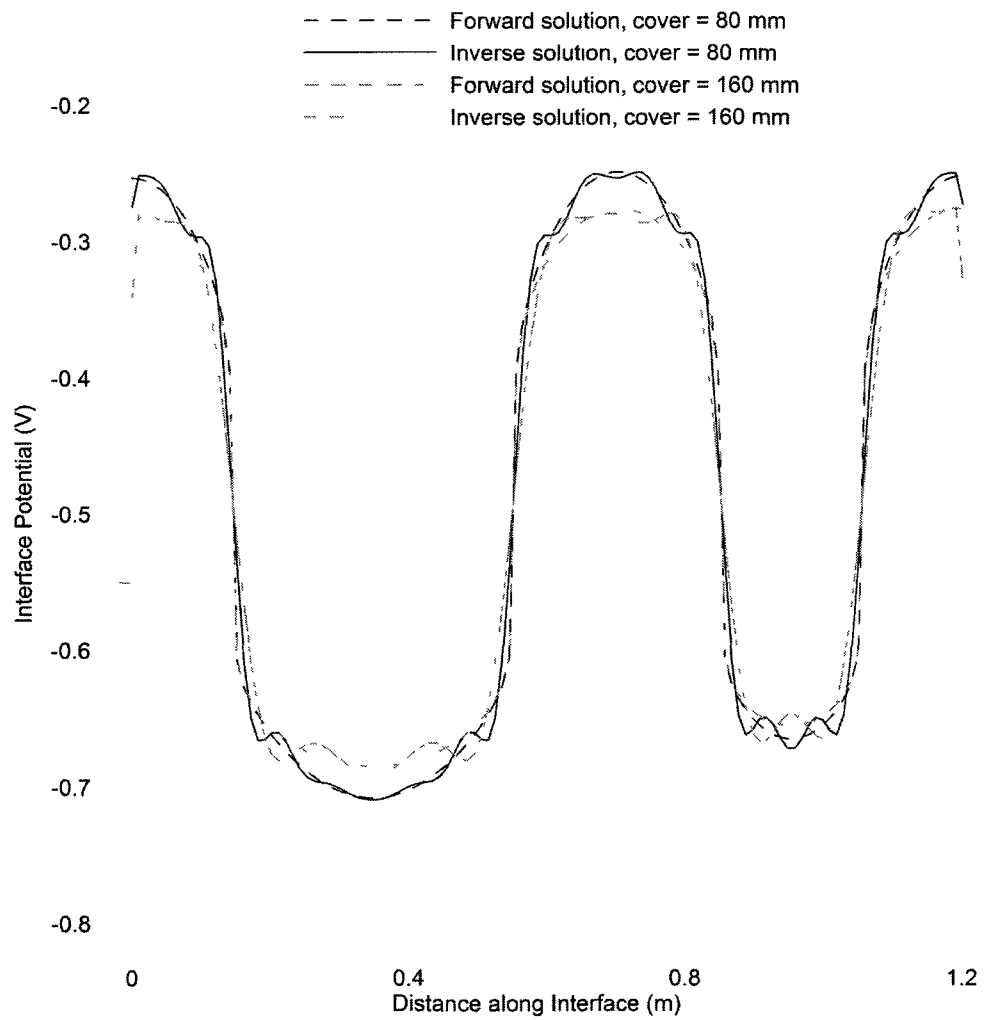


**Figure 5.11:** Comparison of the forward and inverse solutions with Configuration 4 and a resistivity of  $150 \Omega\text{-m}$ .

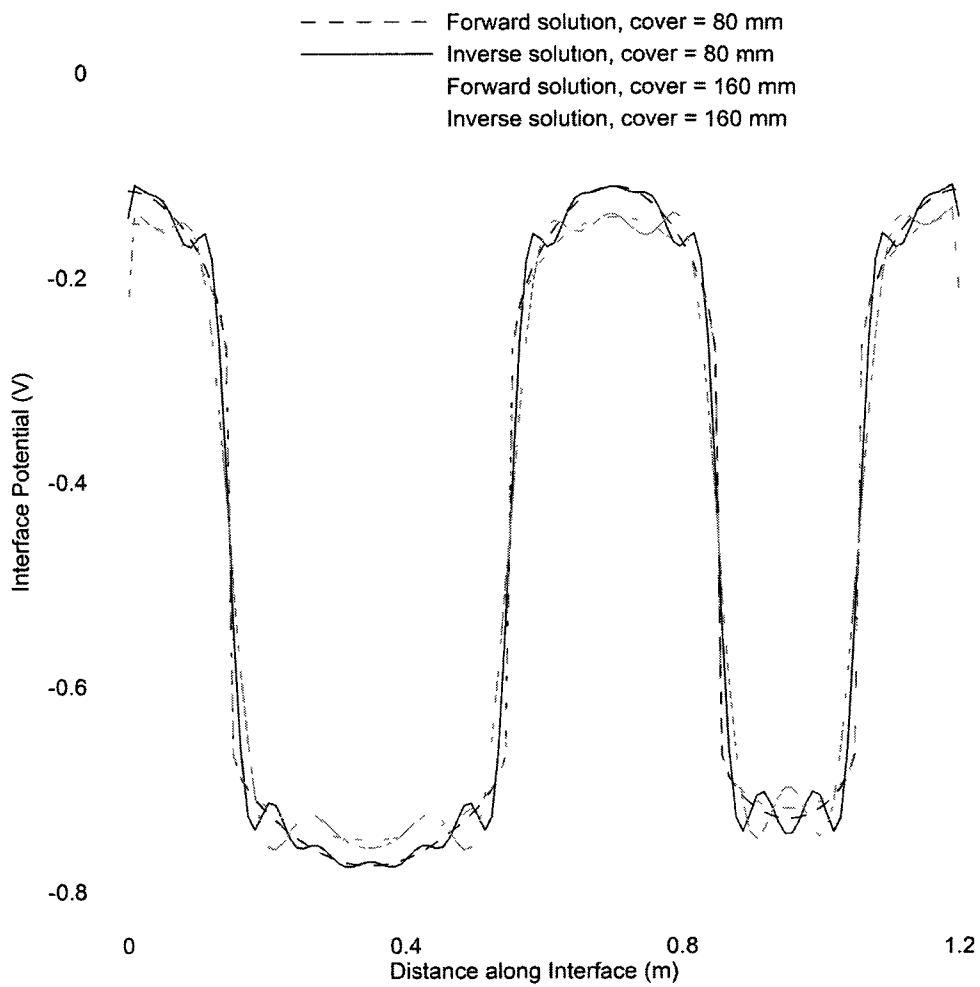


**Figure 5.12:** Comparison of the forward and inverse solutions with Configuration 4 and a resistivity of  $1500 \Omega\text{-m}$ .

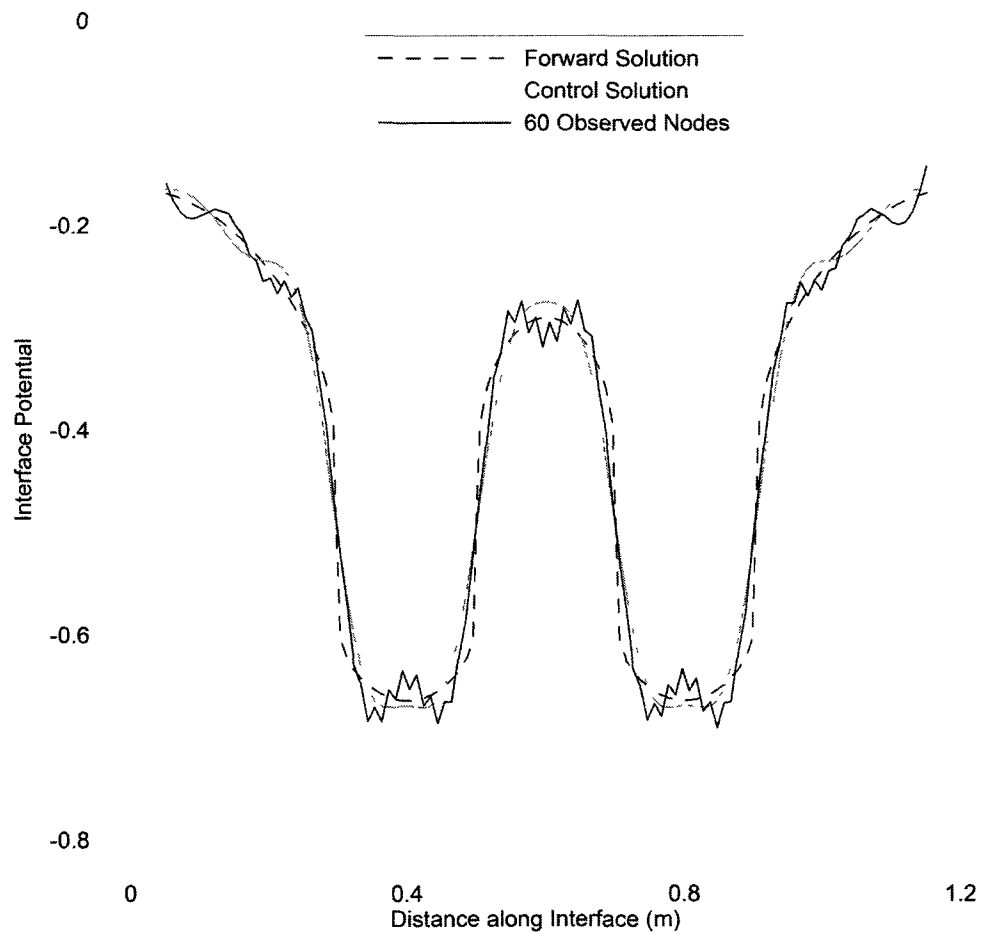


**Figure 5.13:** Comparison of the inverse solution of Configuration 1 with 60 observed nodes, the forward solution and the control solution with all nodes observed.

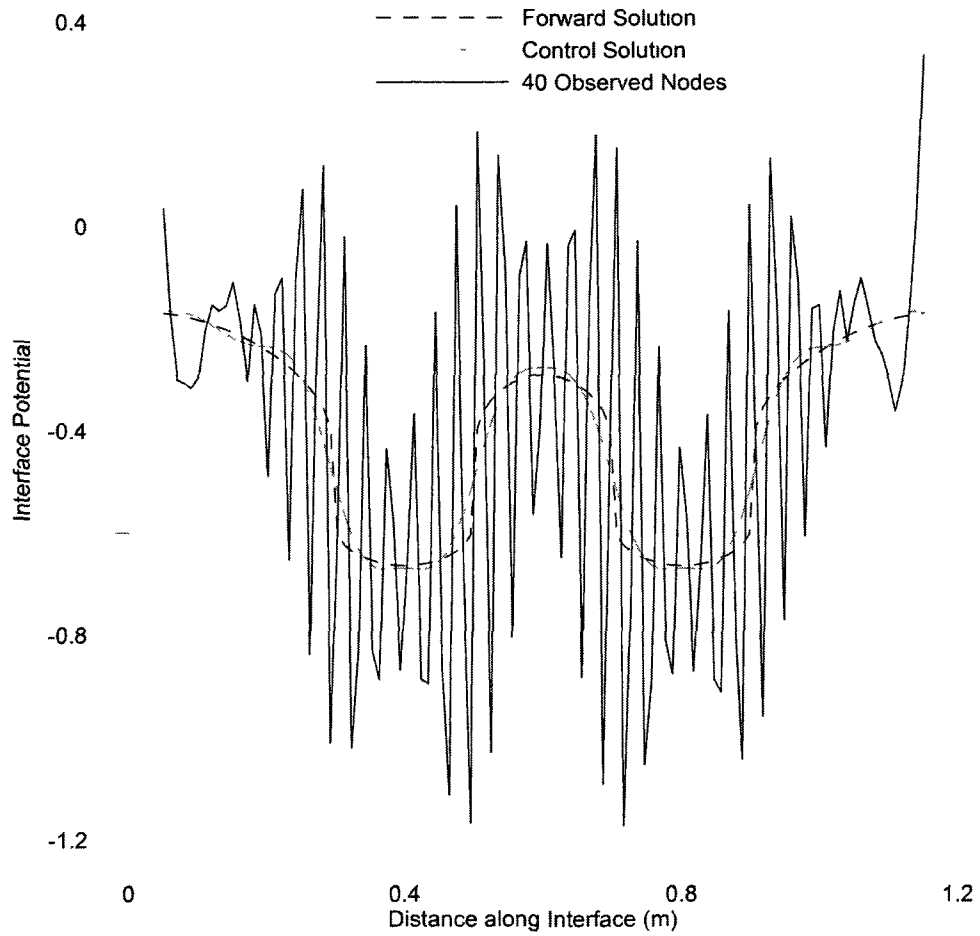


**Figure 5.14:** Comparison of the inverse solution of Configuration 1 with 40 observed nodes. the forward solution and the control solution with all nodes observed.

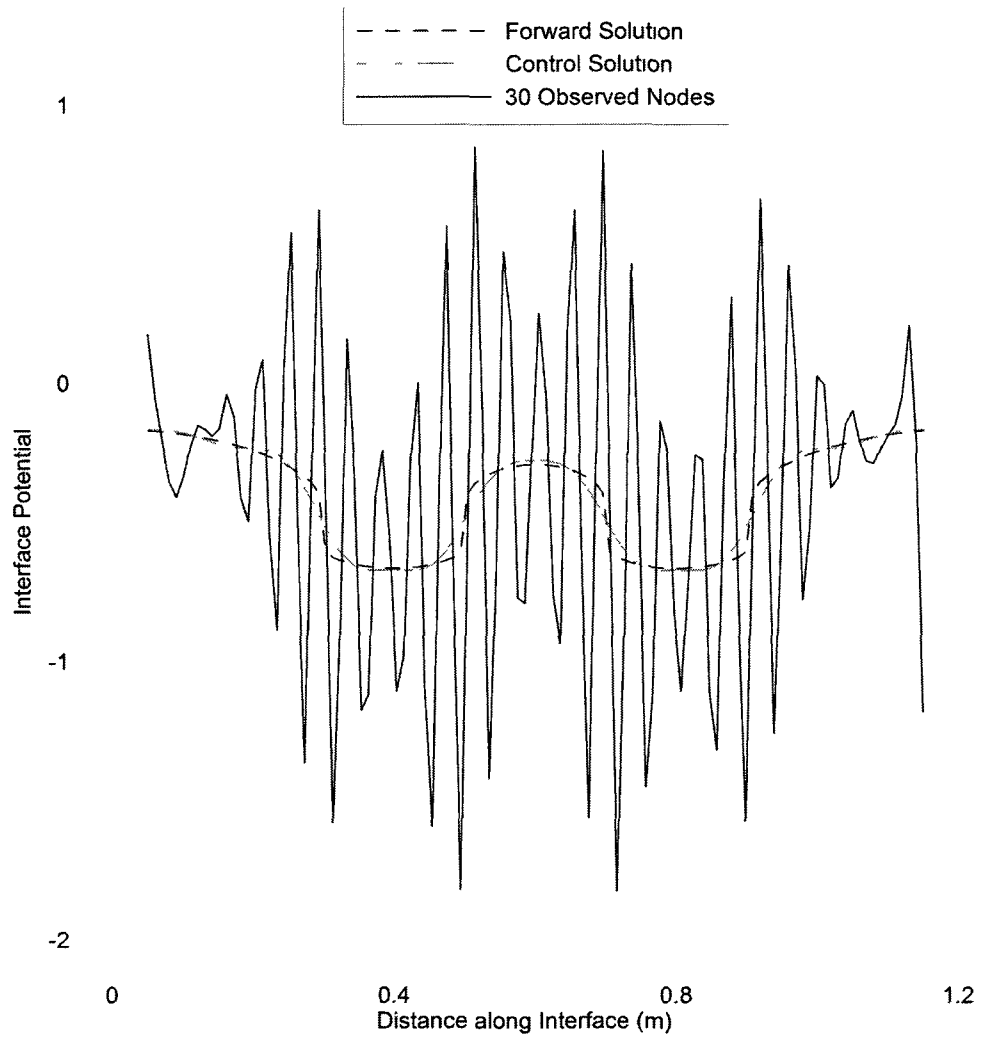


**Figure 5.15:** Comparison of the inverse solution of Configuration 1 with 30 observed nodes, the forward solution and the control solution with all nodes observed.

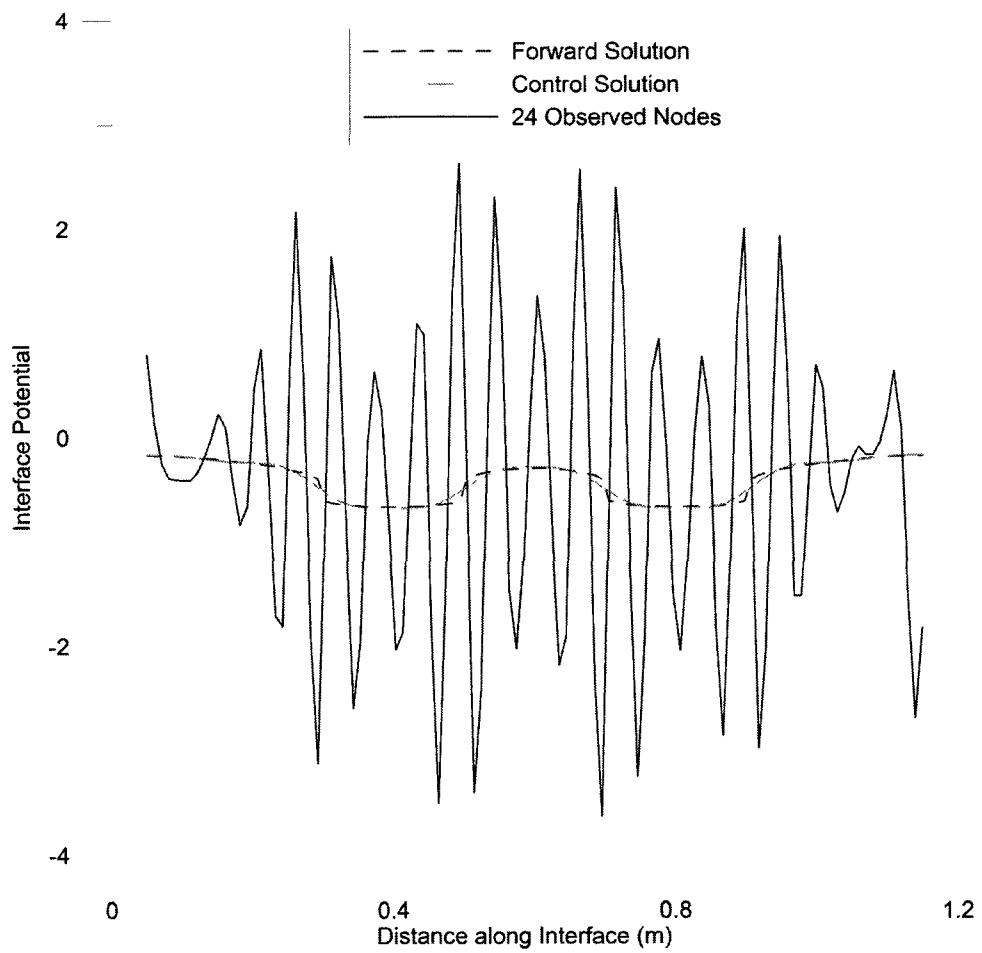


**Figure 5.16:** Comparison of the inverse solution of Configuration 1 with 24 observed nodes, the forward solution and the control solution with all nodes observed.

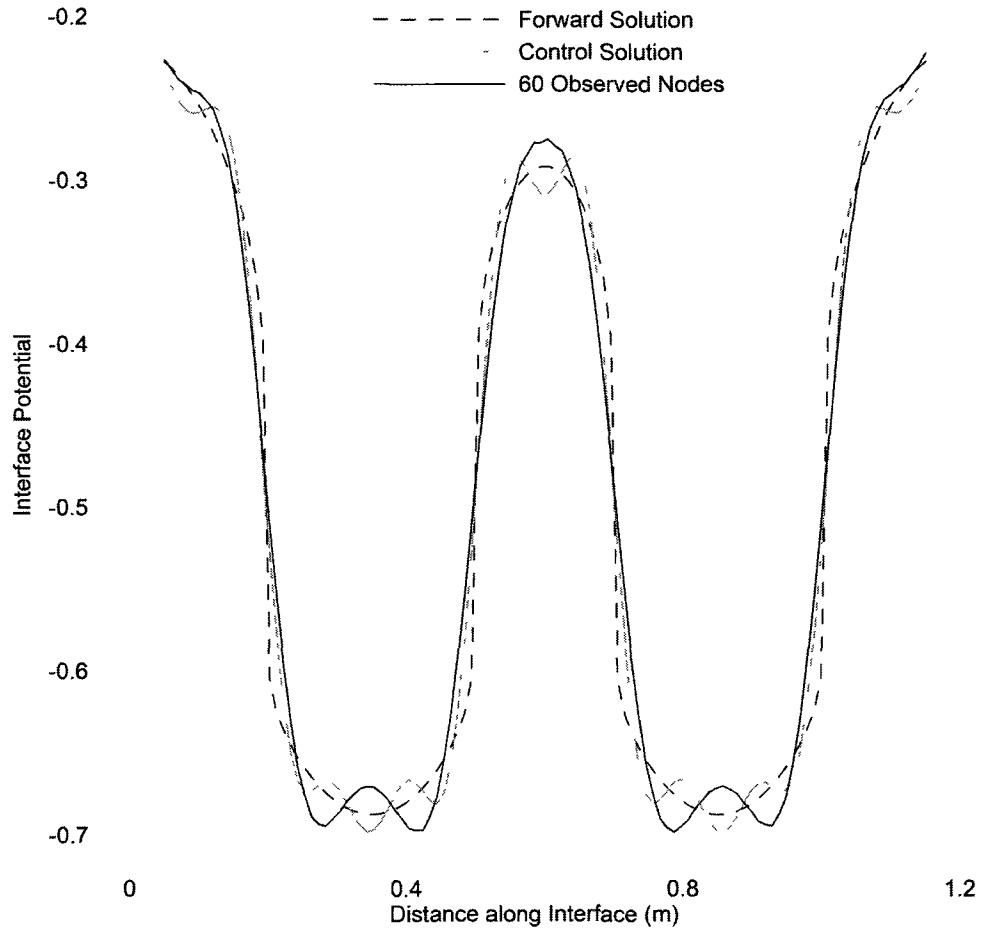


**Figure 5.17:** Comparison of the inverse solution of Configuration 2 with 60 observed nodes, the forward solution and the control solution with all nodes observed.

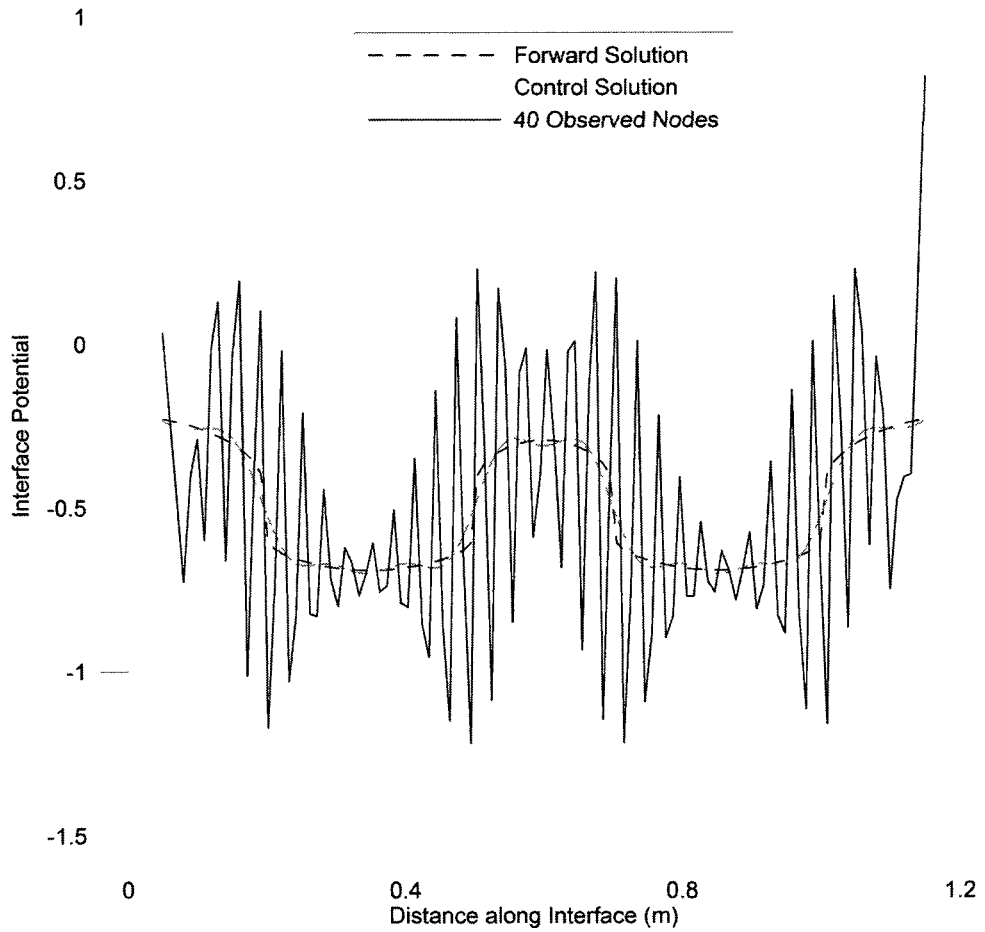


**Figure 5.18:** Comparison of the inverse solution of Configuration 2 with 40 observed nodes, the forward solution and the control solution with all nodes observed.

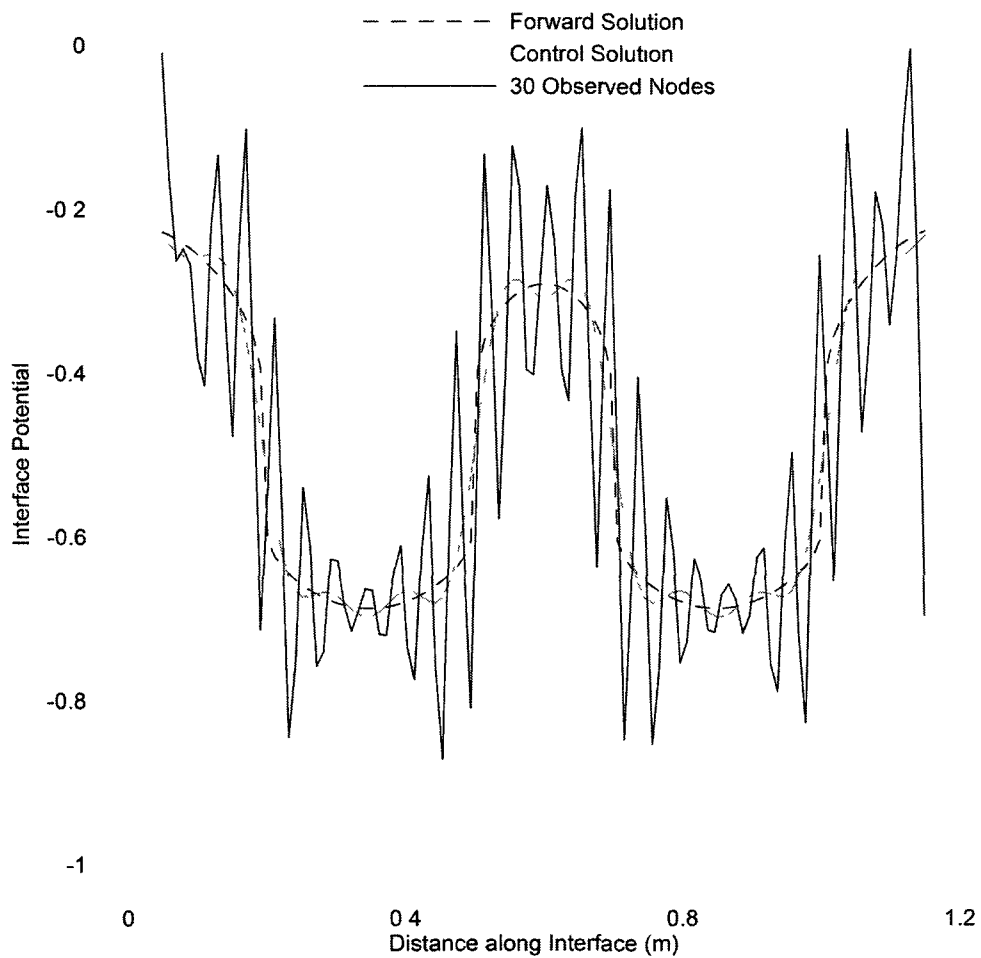


**Figure 5.19:** Comparison of the inverse solution of Configuration 2 with 30 observed nodes, the forward solution and the control solution with all nodes observed.

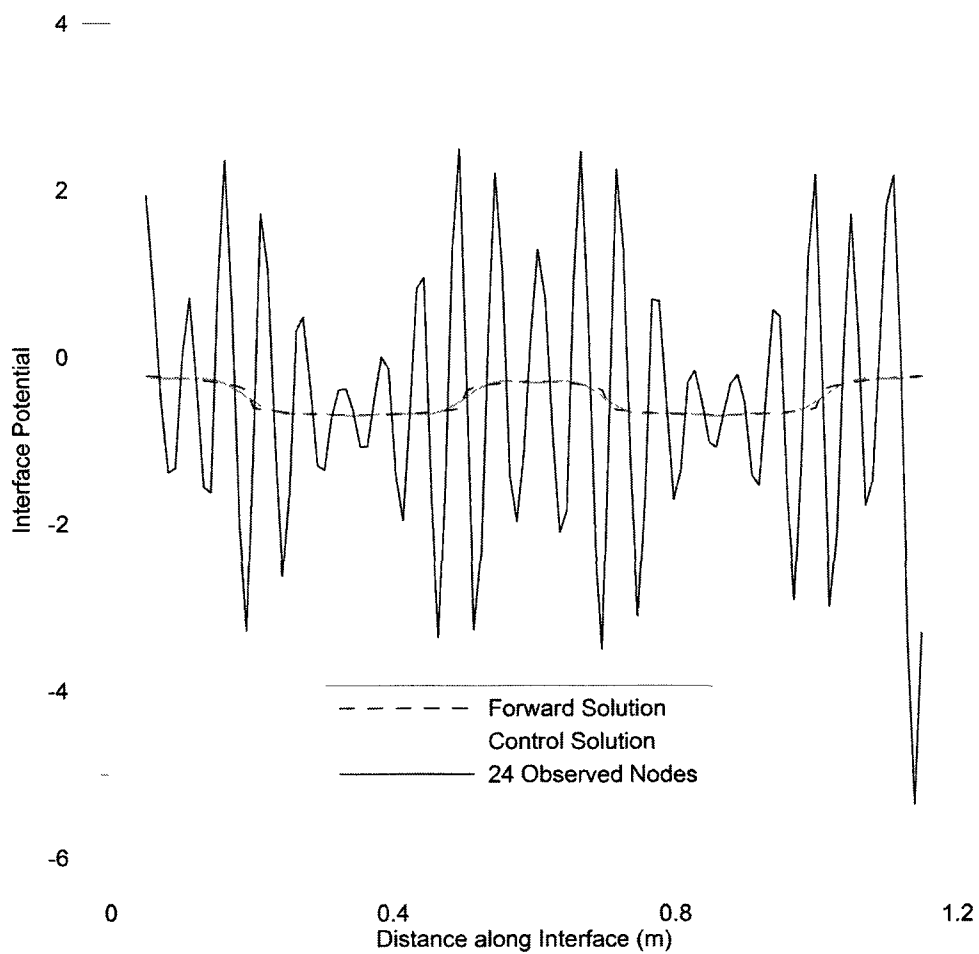


**Figure 5.20:** Comparison of the inverse solution of Configuration 2 with 24 observed nodes, the forward solution and the control solution with all nodes observed.

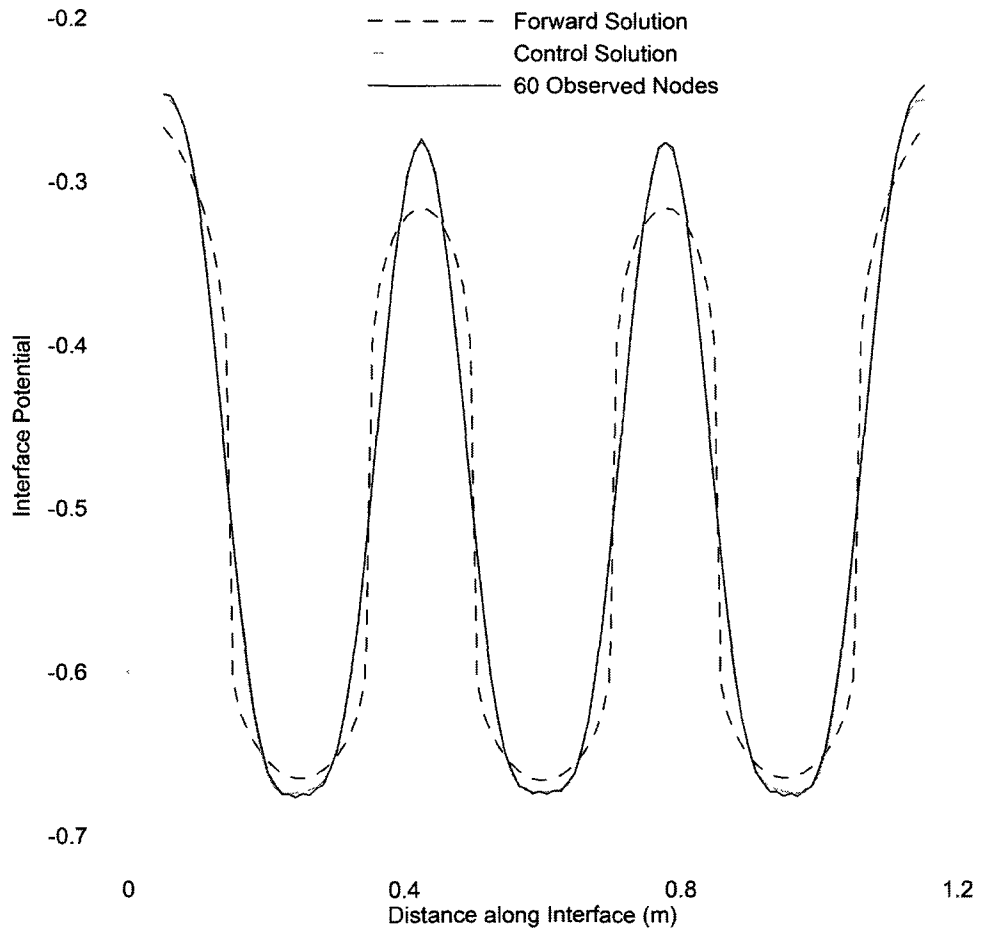


**Figure 5.21:** Comparison of the inverse solution of Configuration 3 with 60 observed nodes, the forward solution and the control solution with all nodes observed.

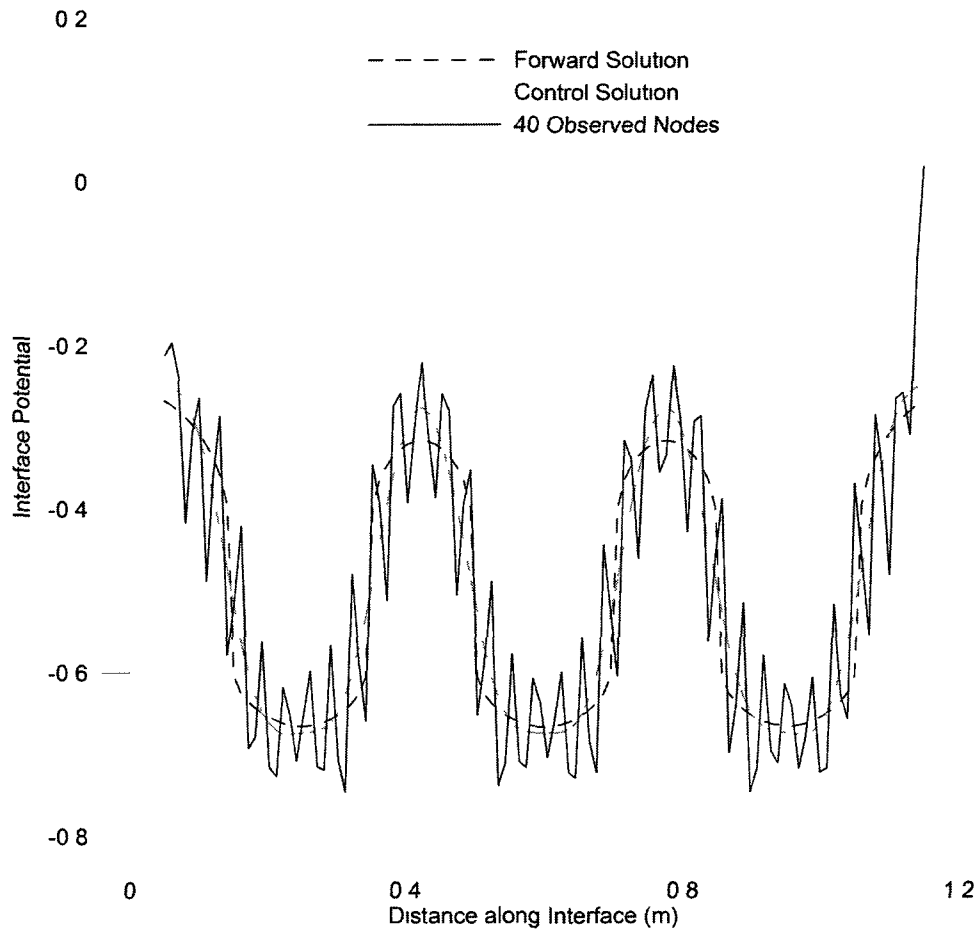


**Figure 5.22:** Comparison of the inverse solution of Configuration 3 with 40 observed nodes, the forward solution and the control solution with all nodes observed.

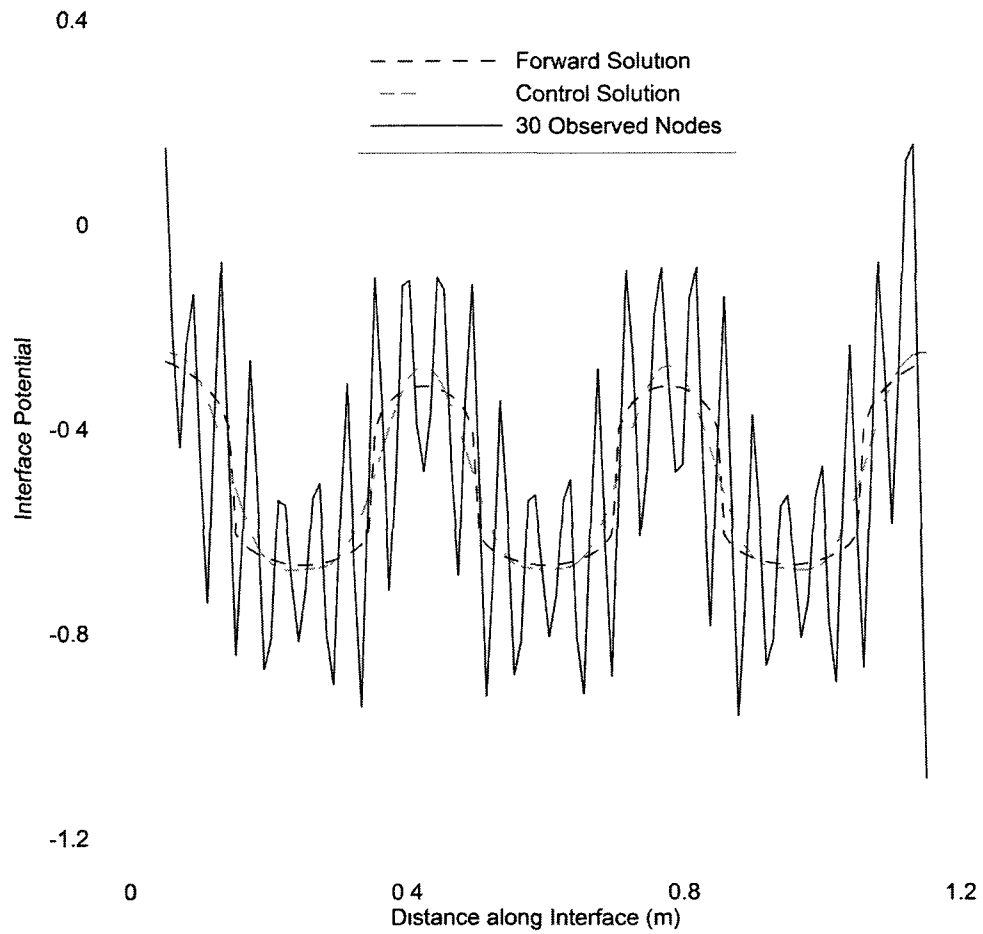


**Figure 5.23:** Comparison of the inverse solution of Configuration 3 with 30 observed nodes, the forward solution and the control solution with all nodes observed.

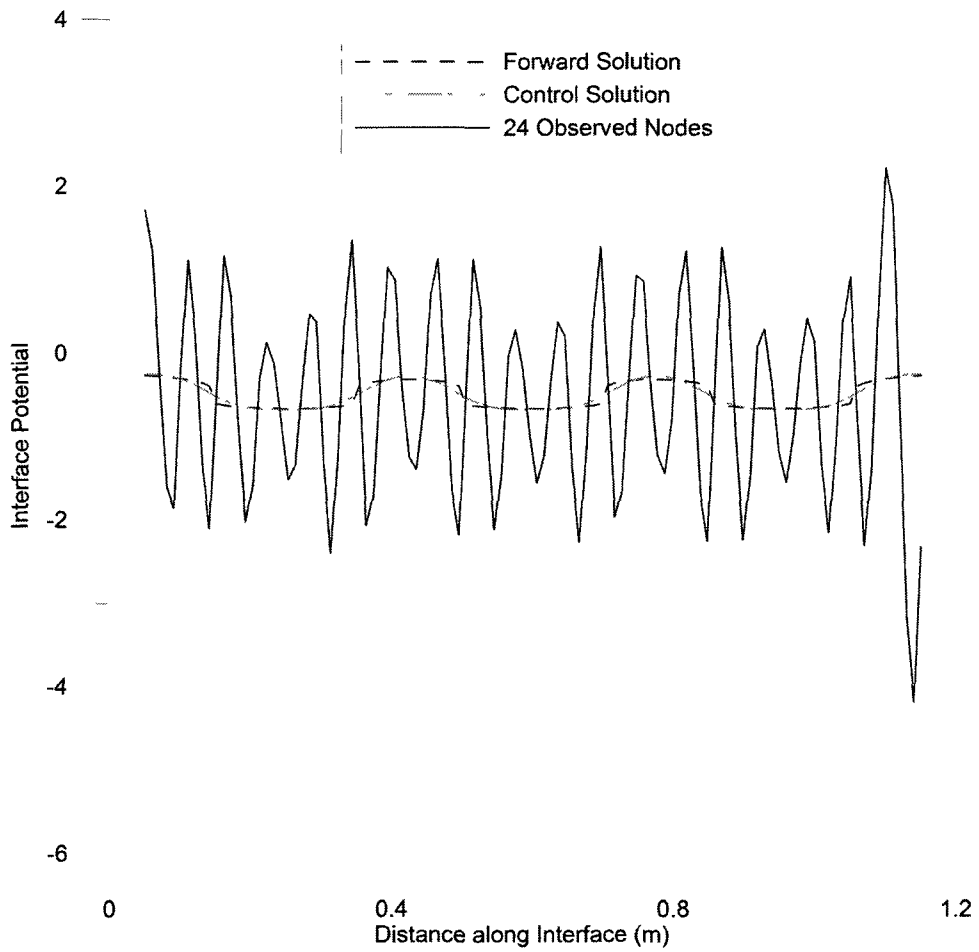


**Figure 5.24:** Comparison of the inverse solution of Configuration 3 with 24 observed nodes, the forward solution and the control solution with all nodes observed.

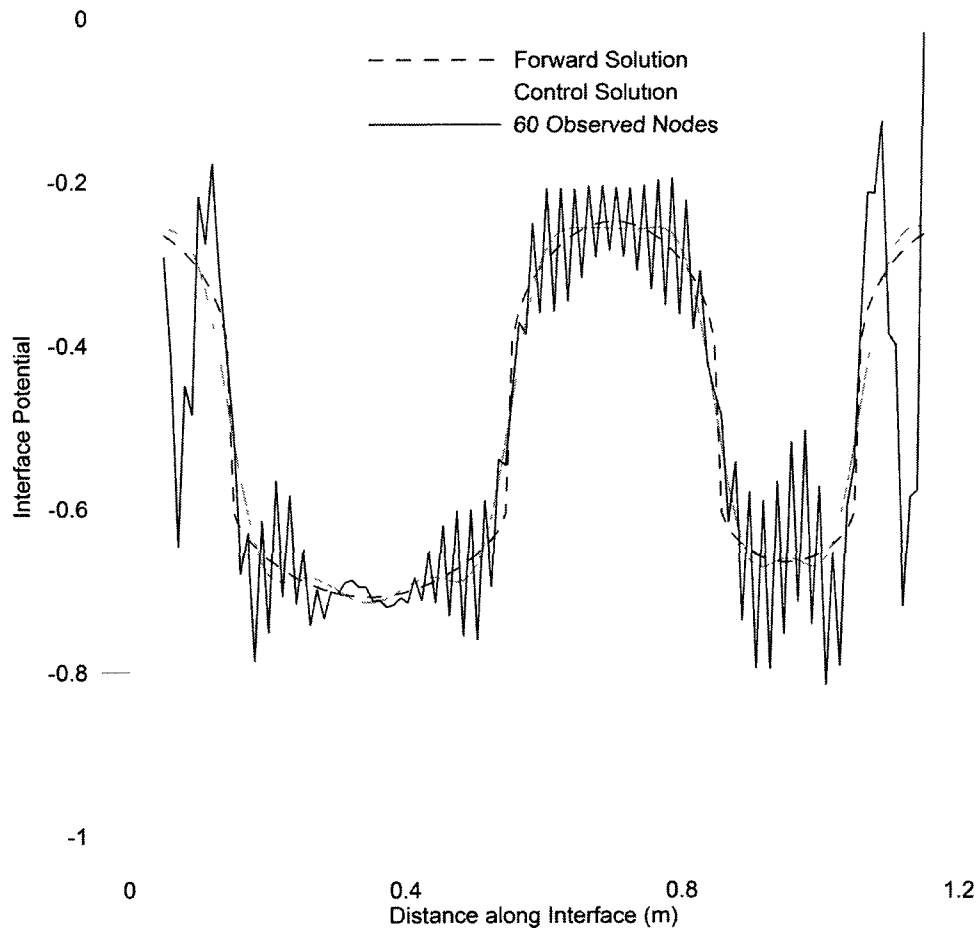


**Figure 5.25:** Comparison of the inverse solution of Configuration 4 with 60 observed nodes, the forward solution and the control solution with all nodes observed.

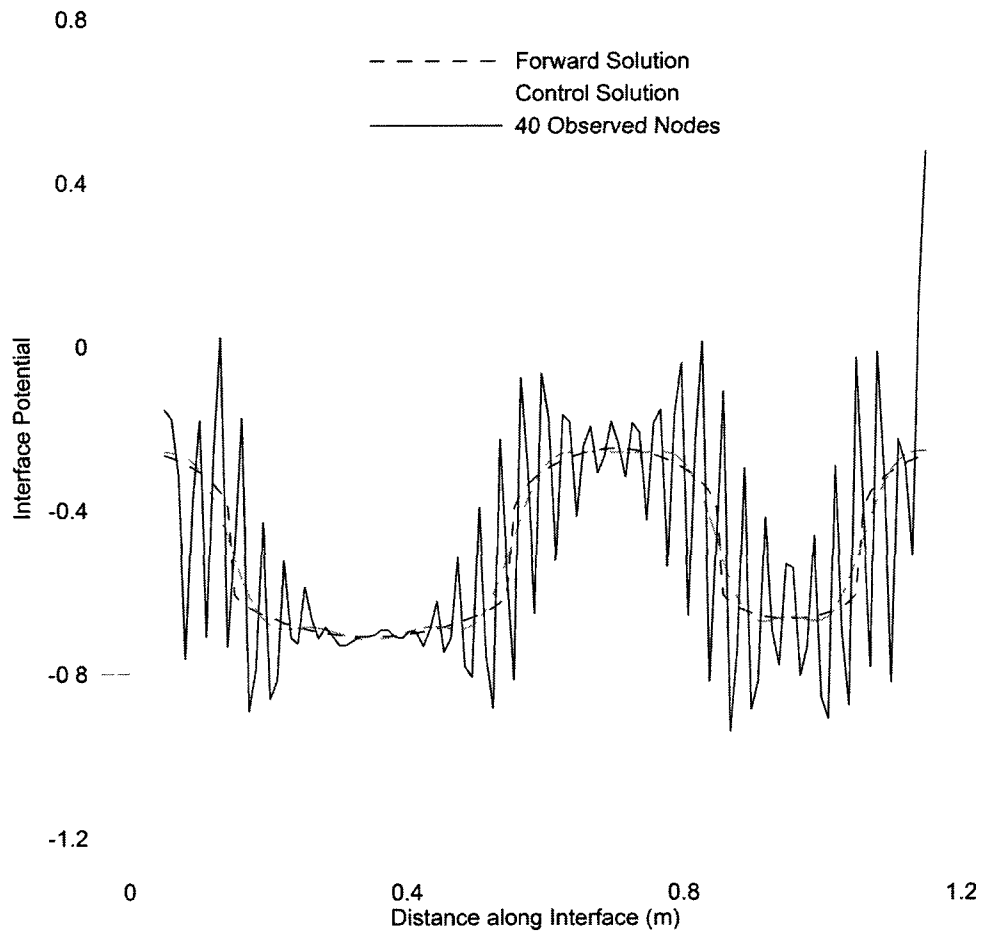


**Figure 5.26:** Comparison of the inverse solution of Configuration 4 with 40 observed nodes, the forward solution and the control solution with all nodes observed.

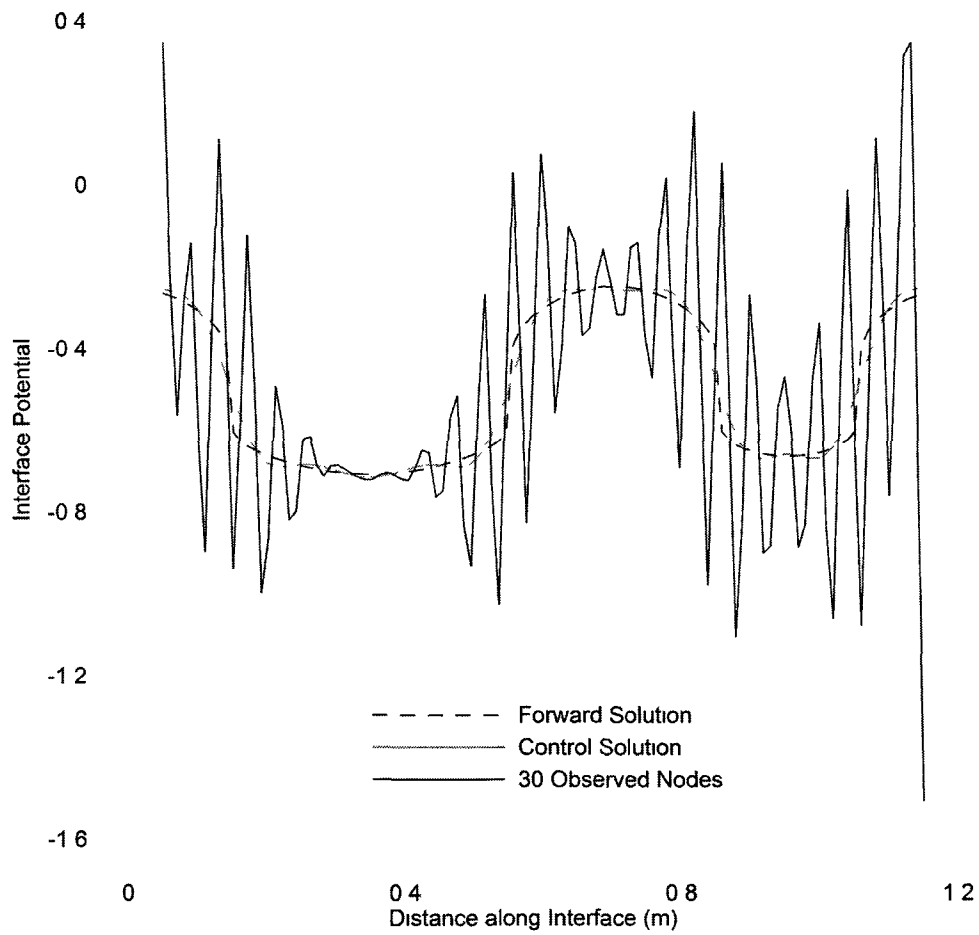


**Figure 5.27:** Comparison of the inverse solution of Configuration 4 with 30 observed nodes, the forward solution and the control solution with all nodes observed.

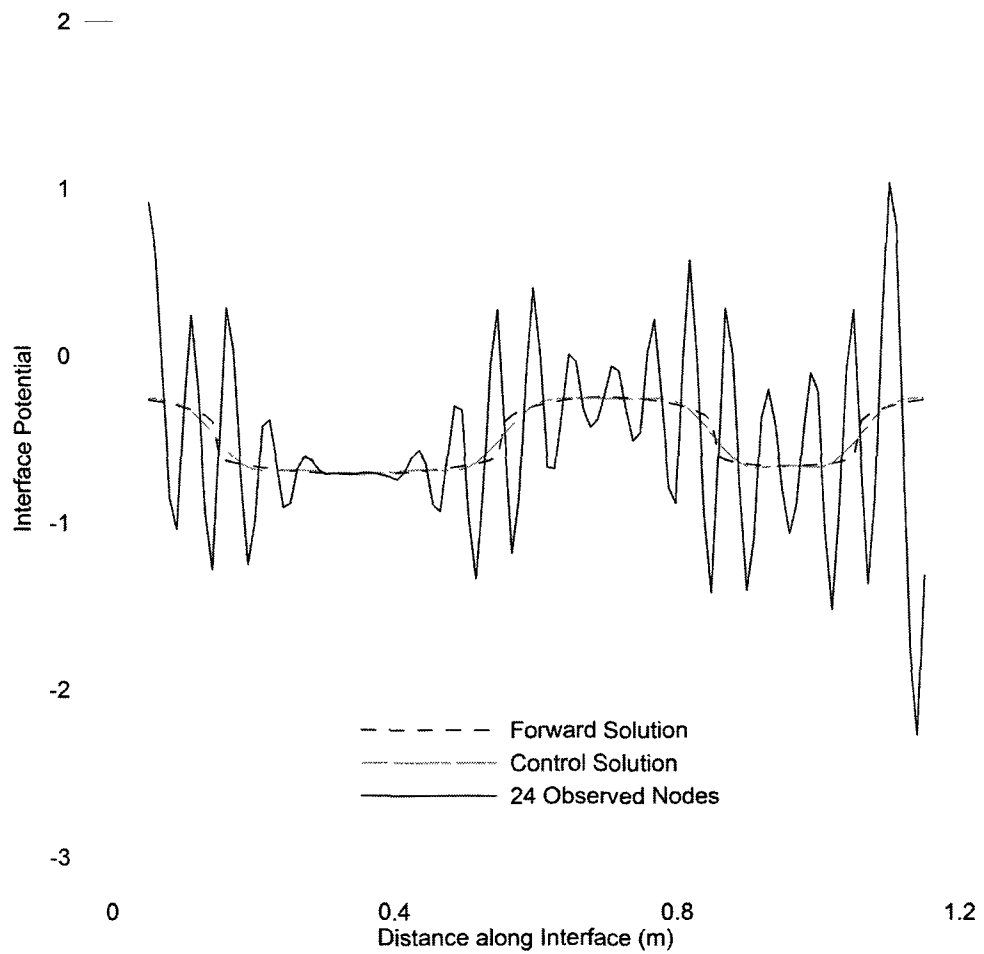


**Figure 5.28:** Comparison of the inverse solution of Configuration 4 with 24 observed nodes, the forward solution and the control solution with all nodes observed.

## Chapter 6

# Conclusions and Future Work

### 6.1 General

It is difficult to determine the state of corrosion on embedded steel reinforcement in concrete using the standardised measurement technique of half-cell potential readings on the surface of the concrete and the current ASTM standard [6]. A new non-destructive method was developed that can assimilate these half-cell potential readings to give a more reasonable estimation of the location and state of active corrosion.

An inverse model was constructed in C++ using an open source finite element package called Dolfin. The inverse problem was solved by repeated forward solutions and the error was evaluated using a least squares cost function. This cost function was minimised using the conjugate gradient method. The produced model assimilates standard half-cell potential measurements and calculates the potential distribution of the surface of the reinforcement.

The performance of the model was investigated with different physical parameters such as resistivity of the concrete and cover thickness, and with different configurations and sizes of anodes and cathodes.

## 6.2 Conclusions

- The developed inverse model successfully assimilated half-cell potential measurements to provide the additional information needed by corrosion engineers to accurately and non-destructively assess the state of corrosion on embedded reinforcement in concrete. The inverse results agreed with the results generated through the validated forward model.
- This inverse model is effective in predicting potential distribution on the surface of the steel reinforcement. It solves the inverse problem with relatively few, and computationally cheap, iterations.
- The model is robust and has little difficulty reaching convergence when the different corrosion and model parameters are varied. The resistivity of the concrete, the cover thickness, the A/C ratio and the locations of the anodes and cathodes can all be varied successfully. The model can detect small localised anodes and multiple anodes in varying numbers and sizes.
- The model naturally produces oscillations in the final solution, however, these oscillations do not obscure the shape of the solution which can still be used to predict the state of corrosion without any regularisation or post processing.
- Although for a few configurations of anodes and cathodes the model has some issues reaching convergence to a solution with an error that is below the criteria used in these studies, the solutions that are reached in these cases still give useful information. The values of the cost function to which these cases converge are very close to the convergence criteria and so the accuracy of the solutions is not compromised very much in these cases.
- When the data on the surface is limited, by the observation of fewer surface

nodes, the model performs fairly well. For limited removal of observed nodes, the final solution is hardly affected. For more extensive removal of observed nodes, information can still be inferred about the state of corrosion although the shape of the solution is eventually obscured by oscillations.

## 6.3 Future Work

- The model needs to be further generalised for three dimensional applications. This would include multiple embedded reinforcements and possibly reinforcement grids.
- Methods of regularisation, post-processing or other methods of reducing oscillations need to be investigated. Although the model performed well for all tests that were run, smoothing of the oscillations would improve the results in extreme cases, such a very limited number of surface nodes, or an extremely small localised anode.
- More research needs to be carried out on the removal of the number of observed nodes. No effort has yet been made to improve the behaviour of the system when operating under this condition. Methods such as the Bezier interpolation algorithm that was applied to the initial potential may potentially be used within the algorithm itself, or for post-processing, to improve the shape of the final solution and draw more information from the predicted potential distributions.
- The model can be further improved by including stochastic processes to model impurities in the steel, resistivity in the concrete, and other physical parameters. Different shapes of domain can also be used to simulate damage and

unsymmetrically shaped areas on beams or slabs.

## List of References

- [1] M. Pour-Ghaz, O. B. Isgor, and P. Ghods, "Quantitative interpretation of half-cell potential measurements in concrete structures," *ASCE Materials Journal*, vol. 21(9), pp. 467–475, 2009.
- [2] P. R. Roberge(ed), *Corrosion basics: an introduction (2nd ed.)*. Houston, Texas: NACE International, 2007.
- [3] L. Bertolini, B. Elsener, P. Pedferri, and R. Polder, *Corrosion of Steel in Concrete*. Weinheim, Germany: WILEY-VCH Verlag GmbH & Co. KGaA, 2004.
- [4] O. B. Isgor and A. G. Razaqpur, "Modelling steel corrosion in concrete structures," *Mater. Struct.*, vol. 39(287), pp. 291–302, 2006.
- [5] K. Tuutti, "Corrosion of steel in concrete," in *6th European Congress on Metallic Corrosion. Soc. Chemical Industry, London*, pp. 655–661, 1977.
- [6] *ASTM Standard C876 ASTM International*. 2009.
- [7] H. Bohni, *Corrosion in Reinforced Concrete Structures*. New York: CRC Press. 2005.
- [8] B. Elsener, "Macrocell corrosion of steel in concrete - implications for corrosion monitoring," *Cem. Concr. Compos.*, vol. 24(1), pp. 65–72, 2002.
- [9] A. A. Sagues and S. C. Kranc, "On the determination of polarization diagrams of reinforcing steel in concrete," *Corrosion*, vol. 48(8), pp. 624–633, 1992.
- [10] A. Poursaee and C. Hansson, "Galvanostatic pulse technique with the current confinement guard ring: The laboratory and finite element analysis," *Corrosion Science*, vol. 50(10), p. 27392746, 2008.

- [11] W. Oelsner, F. Berthold, and U. Guth, "The ir drop well-known but often underestimated in electrochemical polarization measurements and corrosion testing," *Materials and Corrosion*, vol. 57(6), pp. 455–466, 2006.
- [12] M. Pour-Ghaz, "A novel approach for practical modelling of steel corrosion in concrete," Master's thesis, Carleton University, Ottawa, Canada, 2007.
- [13] D. Fasino and G. Inglese, "An inverse robin problem for laplaces equation: theoretical results and numerical methods," *Inverse Problems*, vol. 15, pp. 41–48, 1999.
- [14] D. Lesnic, J. R. Berger, and P. A. Martin, "A boundary element regularisation method for the boundary determination in potential corrosion damage," *Inverse Problems in Engineering*, vol. 10(2), pp. 163–182, 2002.
- [15] R. C. Aster, B. Borchers, and C. H. Thurber, *Parameter Estimation and Inverse Problems*. Elsevier, 2005.
- [16] A. Katchalov, Y. Kurylev, and M. Lassas, *Inverse Boundary Spectral Problems*. Boca Raton, Florida: Chapman and Hall/CRC, 2001.
- [17] D. G. Cacuci, *Sensitivity and Uncertainty Analysis Theory*. Boca Raton, Florida: Chapman and Hall/CRC, 2003.
- [18] A. Tarantola, *Inverse Problem Theory and Methods for Model Parameter Estimation*. Philadelphia PA: The Society for Industrial and Applied Mathemaics, S.I.A.M., 2005.
- [19] G. Inglese, "An iinverse problem in corrosion detection," *inverse Problems*, vol. 13, pp. 977–994, 1997.
- [20] D. Fasino and G. Inglese. "Discrete methods in the study of an inverse problem for laplace's equation," *IMA Journal of Numerical Analysis*, vol. 19, pp. 105–118, 1999.
- [21] F. Kojima, D. Yorifuji, and H. T. Banks, "Shape recovery of corrosion damage for electromagnetic inverse problems arising in nondestructive testing," *SICE*, vol. 57, pp. 1918–1923, 2002.
- [22] R. J. Mayer, K. V. Akella, A. Ibragimov, and M. G. R. Bardsley, "Corrosion and paint breach detection using an ndi-based approach," 2007.

- [23] M. Ridha, K. Amaya, and S. Aoki, "Multistep genetic algorithm for detecting corrosion of reinforcing steels in concrete," *Corrosion*, vol. 57(9), pp. 794–801, 2001.
- [24] M. Ridha, K. Amaya, and S. Aoki, "Boundary element simulation for identification of steel corrosion in concrete using magnetic field measurement," *Corrosion*, vol. 61(8), pp. 784–791, 2005.
- [25] V. Leclalerkiet, J.-W. Kyung, M. Ohtsu, and M. Yokota, "Analysis of half-cell potential measurement for corrosion of reinforced concrete," *Construction and Building Materials*, vol. 18(3), pp. 155–162, 2004.
- [26] S. C. Kranc and A. A. Sagues, "A numerical method for the recovery of local potentials and currents due to corrosion of steel in concrete," *Journal of ATSM International*, vol. 3(2), 2006.
- [27] A. Nachaoui, "An improved implementation of an iterative method in boundary identification problems," *Numerical Algorithms*, vol. 33, pp. 381–398, 2003.
- [28] M. Schweiger, S. R. Arridge, and D. T. Delpy, "Application of the finite-element method for the forward and inverse models in optical tomography," *Journal of Mathematical Imaging and Vision*, vol. 3, pp. 263–283, 1993.
- [29] Y. Xin, C. Mourad, and C. Jin, "An iterative bem for the inverse problem of detecting corrosion in a pipe," *Numerical Mathematics*, vol. 14(3), pp. 252–266, 2005.
- [30] S. W. Provencher, "A fourier method for the analysis of exponential decay curves," *Biophysical Journal*, vol. 16, pp. 27–41, 1976.
- [31] D. Kosloff and R. Kosloff, "A fourier method solution for the time dependent schrödinger equation as a tool in molecular dynamics," *Journal of Computational Physics*, vol. 52, pp. 35–53, 1983.
- [32] W. L. Price, "A controlled random search procedure for global optimisation," *The Computer Journal*, vol. 20(4), pp. 367–370, 1977.
- [33] F. J. Solis and R. J.-B. Wets, "Minimization by random search techniques," *Mathematics of Operations Research*, vol. 6(1), pp. 19–30, 1981.

- [34] H. Kunstmann, J. Krause, and S. Mayr, "Inverse distributed hydrological modelling of alpine catchments," *Hydrology and Earth System Sciences*, vol. 3, pp. 395–412, 2006.
- [35] L. S. Lasdon, S. K. Mitter, and A. D. Warren, "The conjugate gradient method for optimal control problems," *IEEE Transactions on Automatic Control*, vol. 12(2), pp. 132–138, 1967.
- [36] Z.-J. Shi and J. Guo, "A new algorithm of nonlinear conjugate gradient method with strong convergence," *Computational and Applied Mathematics*, vol. 27(1), pp. 93–106, 2008.
- [37] H.-J. Jang, "Preconditioned conjugate gradient method for large generalised eigenproblems," *Trends in Mathematics*, vol. 4(2), pp. 103–109, 2001.
- [38] Y. Yuan, "On the truncated conjugate gradient method," *Math. Program.*, vol. 87, pp. 561–573, 2000.
- [39] D. A. H. Jacobs, "A generalization of the conjugate-gradient method to solve complex systems." *IMA Journal of Numerical Analysis*, vol. 6, pp. 447–452, 1986.
- [40] J. R. Shewchuk, "An introduction to the conjugate gradient method without the agonizing pain edition 1 1/4," 1994.
- [41] P. F. Fischer and S. Gottlieb, "Solving  $ax = b$  using a modified conjugate gradient method based on roots of  $a$ ," *Journal of Scientific Computing*, vol. 15(4), pp. 441–456, 2000.
- [42] R.-C. Li, "Hard cases for conjugate gradient method," *International Journal of Information and Systems Sciences*, vol. 4(1), pp. 15–29, 2008.
- [43] J. Koko, "A conjugate gradient method with quasi-newton approximation," *Applcationes Mathematicae*, vol. 27(2), pp. 153–165, 2000.
- [44] S. Rajashekar and G. Vijayalaxmi, *Neural Networks, Fuzzy Logic and Genetic Algorithms: Synthesis and Applications*. Prentice-Hall of India Pvt.Ltd, 2004.
- [45] C. M. Fonseca and P. J. Fleming, "Genetic algorithms for multiobjective optimization: Formulation, discussion and generalization," *Genetic Algorithms: Proceedings of the Fifth International Conference*, pp. 416–423, 1993.

- [46] J. Horn, N. Nafpliotis, and D. E. Goldberg, "A niched pareto genetic algorithm for multiobjective optimization," in *In Proceedings of the First IEEE Conference on Evolutionary Computation, IEEE World Congress on Computational Intelligence*, pp. 82–87, 1994.
- [47] S. A. Kazarlis, A. G. Bakirtzis, and V. Petridis, "Genetic algorithms for multiobjective optimization: Formulation, discussion and generalization," *IEEE Transactions on Power Systems*, vol. 11(1), pp. 416–423, 1996.
- [48] J.-H. Chou and J. Ghaboussi, "Genetic algorithm in structural damage detection," *Computers and Structures*, vol. 79, pp. 1335–1353, 2001.
- [49] X. Davoine and M. Bocquet, "Inverse modelling-based reconstruction of the chernobyl source term available for long-range transport," *Atmospheric Chemistry and Physics*, vol. 7, pp. 1549–1564, 2007.
- [50] K. Soetaert and T. Petzoldt, "Inverse modelling, sensitivity and monte carlo analysis in r using package fme," *Journal of Statistical Software*, vol. 33(3), 2010.
- [51] P. C. Hansen, *Rank-Deficient and Discrete Ill-Posed Problems: numerical aspects of linear inversion*. Philadelphia PA: The Society for Industrial and Applied Mathematics, S.I.A.M., 1998.
- [52] B. R. Frieden, "Restoring with maximum likelihood and maximum entropy," *Journal of the Optical Society of America*, vol. 62(4), pp. 511–518, 1972.
- [53] B. Lewis and L. Reichel, "Arnoldi-tikhonov regularization methods," *Journal of the Optical Society of America*, vol. 226(1), pp. 92–102, 2009.
- [54] S. Crepey, "Tikhonov regularisation," *Encyclopedia of Quantitative Finance*, 2010.
- [55] L. I. Rudin, S. Osher, and E. Fatemi, "Nonlinear total variation based noise removal algorithms," *Physica D*, vol. 60, pp. 259–268, 1992.
- [56] S. Ceccherini, C. Belotti, B. Carli, P. Raspollini, and M. Ridolfi, "Technical note: Regularization performances with the error consistency method in the case of retrieved atmospheric profiles," *Atmospheric Chemistry and Physics*, vol. 7, p. 14351440, 2007.
- [57] T. Hastie and R. Tibshirani, "Efficient quadratic regularization for expression arrays," *Biostatistics*, vol. 5(3), pp. 329–340, 2004.

- [58] K. Ganchev, J. Graa, J. Gillenwater, and B. Taskar, "Posterior regularization for structured latent variable models," *Journal of Machine Learning Research*, vol. 11, pp. 2001–2049, 2010.
- [59] A. Quattoni, X. Carreras, M. Collins, and T. Darrell, "An efficient projection for l1, regularization," in *ICML '09 Proceedings of the 26th Annual International Conference on Machine Learning*, 2009.
- [60] Q. Yan, X. Yan, X. Yang, and L. Zhang, "Research of optimization inverse analysis technique on corrosion identification of buried pipeline wall," in *ICPTT 2009: Advances and Experiences with Pipelines and Trenchless Technology for Water, Sewer, Gas, and Oil Applications*, pp. 1624–1630, 2009.
- [61] C. Qiu and M. E. Orazem, "A weighted nonlinear regression-based inverse model for interpretation of pipeline survey data," *Electrochimica Acta*, vol. 49, pp. 3965–3975, 2004.
- [62] L. C. Wrobel and P. Miltiadou, "Genetic algorithms for inverse cathodic protection problems," *Engineering Analysis with Boundary Elements*, vol. 28, pp. 267–277, 2004.
- [63] S. Kirkpatrick, "Optimization by simulated annealing: Quantitative studies," *Journal of Statistical Physics*, vol. 34, pp. 975–986, 1984.
- [64] R. C. Black, A. Mathai, F. C. Wellstood, E. Dantsker, A. H. Miklich, D. T. Nemeth, J. J. Kingston, and J. Clarke, "Magnetic microscopy using a liquid nitrogen cooled  $\text{YBa}_2\text{Cu}_3\text{O}_7$  superconducting quantum interference device," *Applied Physics Letters*, vol. 17, 1993.
- [65] A. Logg and G. Wells, "Dolfin: Automated finite element computing," *ACM Transactions on Mathematical Software*, vol. 37(2), 2010.
- [66] G. Yuan, "A conjugate gradient method for unconstrained optimization problems," *International Journal of Mathematics and Mathematical Sciences*, vol. 2009, pp. 1–14, 2009.
- [67] R. Fletcher and M. J. D. Powell, "A rapidly convergent descent method for minimization," *The Computer Journal*, pp. 163–168, 1963.
- [68] R. M. Errico, "What is an adjoint model?," *Bulletin of the American Meteorological Society*, vol. 1997, pp. 2577–2591, 78(11).

- [69] M. S. Alnæs, “The unified form language.” Presentation at the FEniCS ’09 Workshop, Simula Research Laboratory, Oslo, 2009-06-11, 2009. <http://simula.no/research/sc/publications/Simula.SC.608>.
- [70] “COMSOL Multiphysics ®,” 2006. ©1997-2008 COMSOL AB.
- [71] O. B. Isgor, *A Durability Model for Chloride and Carbonation Induced Steel Corrosion in Reinforced Concrete Members*. PhD thesis, Carleton University, Ottawa, Ontario, Canada, 2001.
- [72] G. Ji, “On the numerical solution of laplace’s equation with nonlinear boundary conditions for the corrosion of steel in concrete,” Master’s thesis, Carleton University, Ottawa, Canada, 2006.
- [73] T. Sederberg and R. Farouki, “Approximation by interval bezier curves,” *Computer Graphics and Applications, IEEE*, vol. 12(5), pp. 87–95, 1992.